Stephan SCHEIDL

Validation and extension of a primary jet breakup model for CFD simulation of mixture formation and combustion

Diploma Thesis

Graz University of Technology

Institute of Fluid Mechanics and Heat Transfer

Supervisors:

Univ.-Prof. Dr.-Ing. habil. Günter Brenn

DI. Dr.techn. Wilfried Edelbauer

DI. Dr.techn. Klaus Pachler

Graz, February 2014

EIDESSTATTLICHE ERKLÄRUNG

Ich erkläre an Eides statt, dass ich die vorliegende Arbeit selbstständig verfasst, andere als die angegebenen Quellen/Hilfsmittel nicht benutzt, und die den benutzten Quellen wörtlich und inhaltlich entnommenen Stellen als solche kenntlich gemacht habe.

Graz, am ……………………………   …………………………………………………..
                                                                                    (Unterschrift)

STATUTORY DECLARATION

I declare that I have authored this thesis independently, that I have not used other than the declared sources / resources, and that I have explicitly marked all material which has been quoted either literally or by content from the used sources.

……………………………   …………………………………………………..
           date   (signature)

ABSTRACT

The aim of this thesis was to validate and improve the primary breakup model used for the Lagrangian spray calculation in the CFD code AVL FIRE. Several improvements of the primary breakup model are presented and validated with measurements. To further improve the primary breakup models a detailed information about the region near the nozzle orifice is necessary. This region is visually hard to capture due to the dense spray. Therefore Large Eddy Simulations (LES) of the disintegration of a liquid jet under different flow and ambient conditions were performed. The transient inflow boundary condition was created by an LES of a fully developed turbulent pipe flow. These simulations were used to validate the Coherent Structure Model (turbulence model) from Kobayashi (2005) on different mesh sizes with Direct Numerical Simulation (DNS) data.

Key words: primary breakup, LES, liquid jet, atomization, pipe flow

KURZFASSUNG

Das Ziel dieser Arbeit war die Validierung und Verbesserung des Primärzerfallsmodells für die Lagrange Spray Berechnung in der CFD Software FIRE von AVL. Mehrere Verbesserungen am Primärzerfallsmodell wurden vorgenommen und mit Messungen validiert. Um diese Zerfallsmodelle weiter zu verbessern sind detaillierte Informationen über den Strahlzerfall in der Nähe der Düsenöffnung notwendig. Dieser Bereich ist optisch sehr schwer zu erfassen, da er durch dichten Sprühnebel verdeckt ist. Daher wurden Large Eddy Simulationen (LES) vom Zerfall eines Flüssigkeitsstrahls unter verschiedenen Strömungs- und Umgebungsbedingungen durchgeführt. Die dafür notwendigen transienten Randbedingungen wurden mithilfe weiterer LES von voll entwickelten turbulenten Rohrströmungen erstellt. Diese Simulationen wurden genutzt um das Coherent Structure Model (Turbulenzmodell) von Kobayashi (2005) auf unterschiedlichen Gittern mit Ergebnissen einer Direct Numerical Simulation (DNS) mit ähnlicher Reynoldszahl zu vergleichen.

Schlüsselwörter: Primärzerfall, LES, Strahlzerfall, Spray, Rohrströmung

TABLE OF CONTENTS

NOMENCLATURE

Latin symbols

a	Thermal diffusivity	[m²/s]
A	Area	[m²]
C	Constant	[-]
c	Speed of sound	[m/s]
c_p	Specific heat capacity at constant pressure	[J/kgK]
D	Diameter	[m]
E	Energy	[J]
M	Mass	[kg]
p	Pressure	[Pa]
$\vec{q}$	Heat flux	[W/m²]
r	Radius	[m]
R	Universal gas constant	[J/molK]
t	Time	[s]
T	Temperature	[K]
u	Velocity component, usually in x-direction	[m/s]
u^+	Non-dimensional velocity	[-]
v	Velocity component, usually in y-direction	[m/s]
V	Volume	[m³]
w	Velocity component, usually in z-direction	[m/s]
x	Coordinate	[m/s]
y	Coordinate	[m/s]
y^+	Non-dimensional distance from the wall	[-]
z	Coordinate	[m/s]

Greek symbols

α	Void fraction	[-]
κ	Isentropic exponent	[-]
λ	Thermal conductivity	[W/mK]
μ	Dynamic viscosity	[Ns/m²]
ν	Kinematic viscosity	[m²/s]
ρ	Density	[kg/m³]

| σ | Surface tension | [N/m] |
| τ | Shear stress | [N/m²] |

Abbreviations

CFD	Computational fluid dynamics
DDM	Discrete droplet model
DNS	Direct numerical simulation
Ec	Eckert number
IC	Internal combustion
LES	Large eddy simulation
Ma	Mach number
Oh	Ohnesorge number
Pr	Prandtl number
Re	Reynolds number
SGS	Sub grid scale
SMD	Sauter mean diameter
TKE	Turbulent kinetic energy
VOF	Volume of fluid
We	Weber number

1   Introduction

For the development of IC engines many test bed runs are needed to optimize the still growing number of parameters that influence efficiency and emissions. Simulating the combustion becomes more and more important to help understand combustion processes and pollutant formation. Especially for Diesel engines, the spray formation is of high interest, since combustion and injection take place simultaneously. Multiple pilot and post injections are used to reduce noise level and emissions. High-pressure fuel injection is used for better spray atomization and smaller droplet diameters and therefore faster evaporation.

The surface of a liquid jet that emerges from a nozzle is deformed by disturbances coming from turbulence, cavitation or oscillations of the fuel system. If the turbulence is high enough or if the disturbances are amplified by aerodynamic forces drops detach from the jet surface. This process is called primary breakup. When these drops further disintegrate into smaller drops, so-called secondary breakup is happening. The length of the coherent liquid structure of the spray is called the liquid core length. Figure 1 illustrates the disintegration of a liquid jet.
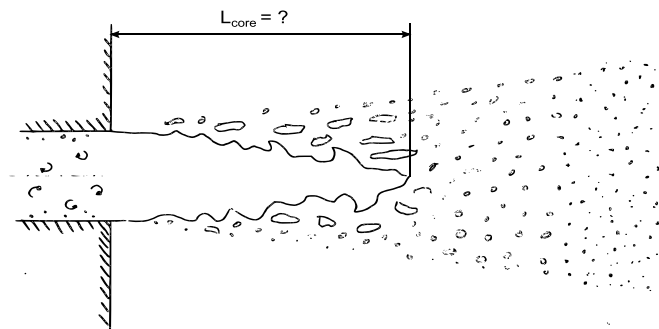
Figure 1: Liquid jet disintegration

The liquid core is very hard to observe due to the dense spray that covers the core region. Due to this fact, and because the nozzle flow conditions strongly influence the spray formation, one task of this thesis was to perform Large Eddy Simulations of the disintegration of a liquid jet emerging from a nozzle, described in chapter 4. The exactly defined inflow conditions that are possible in simulations make it easier to study the different mechanisms of breakup. In this thesis, a fully developed turbulent pipe flow was

used as an inflow boundary condition. The flow field was generated by an LES of a turbulent pipe flow as described in chapter 3.

During the development of a new Diesel engine, simulations of the spray formation and combustion can reduce test bed runs. The computational costs of DNS and LES, however, are much too high to simulate multiple engine cycles. That's why models are necessary to reduce the computation time. Today mostly Lagrangian spray models are used, where the liquid that emerges from the nozzle is modeled by blobs. These blobs are initialized with the flow properties at the nozzle orifice. Special primary breakup models are used for the initial breakup of these blobs. Further breakup is modeled by secondary breakup models. Sometimes the nozzle flow is simulated separately, and the flow properties at the nozzle orifice are stored to a so-called nozzle file. This nozzle file is then used in a Lagrangian spray simulation. Figure 2 illustrates this process.
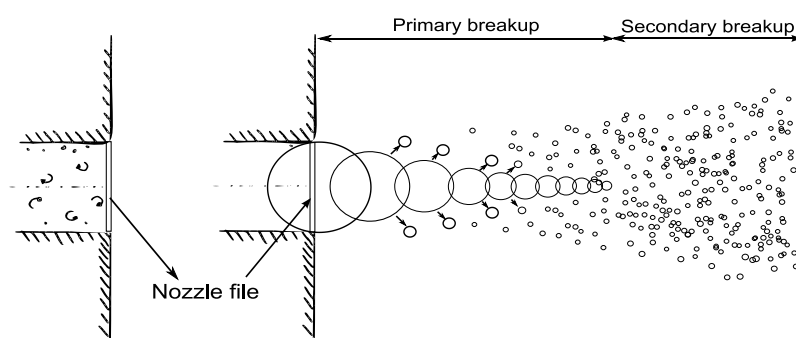
Figure 2: Simulation of spray formation

These models are well accepted and commonly used in engine development nowadays. In contrast, the separate nozzle flow simulation is not so often used. The 3D CFD software FIRE from AVL offers this feature, and one task of this thesis was to improve the primary breakup model in FIRE to allow the use of a nozzle file that not only contains the main, but also pilot and post injections. Of special interest is the transient phase when the injector needle is opening or closing. Chapter 5 deals with this task.

2 Theory

2.1 The fundamental equations

The fundamental equations are based on the following 3 axioms:

1. Mass cannot be created or destroyed.
2. The change of momentum of a body with time is the sum of the forces acting on it.
3. The change of internal and kinetic energies of a body with time is the sum of the power of the forces acting on it and the transferred thermal power.

Starting from a Lagrangian (mass based) consideration, we observe some mass points as they are moving with the flow of a continuum. The considered mass points occupy a control volume $\bar{V} = \bar{V}(t)$ that changes its shape in time. Applying the 3 axioms to the control volume, the following equations can be derived:

Mass
$$\frac{dM}{dt} = \frac{d}{dt}\int_{\bar{V}(t)} \rho\, dV = 0 \tag{2.1}$$

Momentum
$$\frac{dI}{dt} = \frac{d}{dt}\int_{\bar{V}(t)} \rho\vec{v}\, dV = \sum \vec{f} \tag{2.2}$$

Energy
$$\frac{dE}{dt} = \frac{d}{dt}\int_{\bar{V}(t)} \rho\left(e + \frac{1}{2}\vec{v}^2\right) dV = \vec{v}\sum \vec{f} + \sum(\dot{Q} + S_e) \tag{2.3}$$

In these equations, $\vec{f}$ is a force, $\dot{Q}$ is the rate of heat flow (conduction or convection) and S_e is a heat source. The heat source could be a chemical reaction (combustion) inside the control volume.

Using the Reynolds transport theorem, these equations can be transferred from Lagrangian to Eulerian coordinates.

$$\frac{d}{dt}\int_{\bar{V}(t)} \phi\, dV = \frac{\partial}{\partial t}\int_V \phi\, dV + \oint_S \phi(\vec{v}\cdot\vec{n})\, dA \tag{2.4}$$

The total change in time of the integral of a scalar or vectorial quantity ϕ over the time dependent volume $\bar{V}(t)$ is the sum of the local change and the convective change (flow across the surface of V).

With the divergence theorem (Gauß's theorem), the surface integral can be transformed into a volume integral.

$$\oint_S \vec{n} \cdot \vec{F} dA = \int_V \vec{\nabla} \cdot \vec{F} dV, \tag{2.5}$$

where $\vec{F}$ is a vector field. Since V does not depend on time, the Reynolds transport theorem can be written as

$$\frac{d}{dt} \int_{\bar{V}(t)} \phi dV = \int_V \left[\frac{\partial \phi}{\partial t} + \vec{\nabla} \cdot (\phi \vec{v}) \right] dV \tag{2.6}$$

The forces that act on the volume are

Surface forces
$$\vec{F_s} = \oint_S (\underline{\sigma} \cdot \vec{n}) dA = \int_V \vec{\nabla} \cdot \underline{\sigma} dV \tag{2.7}$$

Mass forces
$$\vec{F_B} = \int_V \rho \vec{f^B} dV \tag{2.8}$$

The rate of heat flow can be written as

$$\dot{Q} = -\oint_S (\vec{q} \cdot \vec{n}) dA = -\int_V (\nabla \cdot \vec{q}) dV \tag{2.9}$$

Let $\vec{q}$ denote the heat flux vector and $\vec{n}$ the outward normal to the surface, then $-(\vec{q} \cdot \vec{n})$ is the heat flux into the volume. The heat source is defined as

$$S_e = \int_V \dot{q}_Q dV \tag{2.10}$$

where $\dot{q}_Q$ is the volumetric rate of heat production.

The resulting conservation equations read

Mass
$$\frac{dM}{dt} = \frac{d}{dt}\int_{\bar{V}(t)} \rho dV = \int_V \left[\frac{\partial \rho}{\partial t} + \vec{\nabla}\cdot(\rho\vec{v})\right]dV = 0$$

Momentum
$$\frac{dI}{dt} = \frac{d}{dt}\int_{\bar{V}(t)} \rho\vec{v}dV = \int_V \left[\frac{\partial \rho\vec{v}}{\partial t} + \vec{\nabla}\cdot(\rho\vec{v}\vec{v})\right]dV = F_s + F_B$$

Energy
$$\frac{dE}{dt} = \frac{d}{dt}\int_{\bar{V}(t)} \rho\left(e + \frac{1}{2}\vec{v}^2\right)dV$$

$$= \int_V \left[\frac{\partial \rho\left(e + \frac{1}{2}\vec{v}^2\right)}{\partial t} + \vec{\nabla}\cdot\rho\vec{v}\left(e + \frac{1}{2}\vec{v}^2\right)\right]dV$$

$$= \vec{v}\sum\vec{f} + \sum(\dot{Q} + S_e)$$

This leads to the integral forms of the basic equations

Mass
$$\int_V \left[\frac{\partial \rho}{\partial t} + \vec{\nabla}\cdot(\rho\vec{v})\right]dV = 0 \qquad (2.11)$$

Momentum
$$\int_V \left[\frac{\partial \rho\vec{v}}{\partial t} + \vec{\nabla}\cdot(\rho\vec{v}\vec{v})\right]dV = \int_V \left[\vec{\nabla}\cdot\underline{\sigma} + \rho\vec{f^B}\right]dV \qquad (2.12)$$

Energy
$$\int_V \left[\frac{\partial}{\partial t}\left(\rho\left(e + \frac{1}{2}\vec{v}^2\right)\right) + \vec{\nabla}\cdot\rho\vec{v}\left(e + \frac{1}{2}\vec{v}^2\right)\right]dV$$

$$= \int_V \left[\vec{v}\left(\vec{\nabla}\cdot\underline{\sigma} + \rho\vec{f^B}\right) - (\nabla\cdot\vec{q}) + \dot{q}_Q\right]dV \qquad (2.13)$$

The stress tensor for Cartesian coordinates looks like

$$\underline{\sigma} = \begin{bmatrix} \sigma_{xx} & \tau_{yx} & \tau_{zx} \\ \tau_{xy} & \sigma_{yy} & \tau_{zy} \\ \tau_{xz} & \tau_{zy} & \sigma_{zz} \end{bmatrix}$$

By separating the pressure from the normal stresses, only the deformation induced values remain in the tensor $\underline{\tau}$

$$\sigma_{xx} = -p + \tau_{xx}; \quad \sigma_{yy} = -p + \tau_{yy}; \quad \sigma_{zz} = -p + \tau_{zz}$$

So the stress tensor can be written as

$$\underline{\sigma} = \begin{bmatrix} \sigma_{xx} & \tau_{yx} & \tau_{zx} \\ \tau_{xy} & \sigma_{yy} & \tau_{zy} \\ \tau_{xz} & \tau_{zy} & \sigma_{zz} \end{bmatrix} = -pI + \begin{bmatrix} \tau_{xx} & \tau_{yx} & \tau_{zx} \\ \tau_{xy} & \tau_{yy} & \tau_{zy} \\ \tau_{xz} & \tau_{zy} & \tau_{zz} \end{bmatrix} = -pI + \underline{\tau}, \tag{2.14}$$

where the values τ_{ij} are the deformation induced stresses and I is the unit tensor.

With the stress tensor given by equation (2.14), the differential form of the conservation equations look like

Mass
$$\frac{\partial \rho}{\partial t} + \vec{\nabla} \cdot (\rho \vec{v}) = 0 \tag{2.15}$$

Momentum
$$\frac{\partial \rho \vec{v}}{\partial t} + \vec{\nabla} \cdot (\rho \vec{v} \vec{v}) = -\vec{\nabla} p + \vec{\nabla} \cdot \underline{\tau} + \rho \vec{f^B} \tag{2.16}$$

Energy
$$\frac{\partial}{\partial t} \left[\rho \left(e + \frac{1}{2} \vec{v}^2 \right) \right] + \vec{\nabla} \cdot \rho \vec{v} \left(e + \frac{1}{2} \vec{v}^2 \right)$$
$$= \vec{v} \left(\vec{\nabla} \cdot \underline{\sigma} + \rho \vec{f^B} \right) - (\nabla \cdot \vec{q}) + \dot{q}_Q \tag{2.17}$$

For Newtonian fluids, the stress-strain relationship is known as

$$\tau_{xx} = \mu \left[2 \frac{\partial u}{\partial x} - \frac{2}{3} (\vec{\nabla} \cdot \vec{v}) \right]$$

$$\tau_{yy} = \mu \left[2 \frac{\partial v}{\partial y} - \frac{2}{3} (\vec{\nabla} \cdot \vec{v}) \right]$$

$$\tau_{zz} = \mu \left[2 \frac{\partial w}{\partial z} - \frac{2}{3} (\vec{\nabla} \cdot \vec{v}) \right]$$

$$\tau_{xy} = \tau_{yx} = \mu \left[\frac{\partial u}{\partial y} + \frac{\partial v}{\partial x} \right]$$

$$\tau_{yz} = \tau_{zy} = \mu \left[\frac{\partial v}{\partial z} + \frac{\partial w}{\partial y} \right]$$

$$\tau_{zx} = \tau_{xz} = \mu \left[\frac{\partial w}{\partial x} + \frac{\partial u}{\partial z} \right]$$

Following Steiner (2010), for a Newtonian fluid, the stress tensor σ_{ij} can be written as

$$\sigma_{ij} = -p\delta_{ij} - \underbrace{\frac{2}{3}\mu(\vec{\nabla}\cdot\vec{v})\delta_{ij}}_{dilatation} + \underbrace{2\mu S_{ij}}_{\substack{linear\ deformation\ i=j \\ angle\ change\ i\neq j}} \quad , \tag{2.18}$$

where S_{ij} denotes the rate of strain tensor

$$S_{ij} = \frac{1}{2}\left(\frac{\partial u_i}{\partial x_j} + \frac{\partial u_j}{\partial x_i}\right) \tag{2.19}$$

2.1.1   Incompressible flow

For incompressible flow $\rho = \rho(T)$, the continuity equation reduces to

$$\vec{\nabla}\cdot\vec{v} = 0 \ , \tag{2.20}$$

which means that volume dilatation is zero.

The resulting momentum equation for a Newtonian, incompressible fluid read

$$\frac{\partial\vec{v}}{\partial t} + (\vec{v}\cdot\vec{\nabla})\vec{v} = -\frac{1}{\rho}\vec{\nabla}p + \nu\Delta\vec{v} + \vec{f}^B \tag{2.21}$$

For incompressible Newtonian fluids with negligible rate of viscous heating, all types of flows without heat transfer can be described by these equations. An exact solution is only possible for special laminar cases in simple geometries. Even the numerical solution is sometimes difficult or even impossible.

The energy equation in compact form reads

$$\rho\frac{d}{dt}\left(e + \frac{1}{2}|\vec{v}|^2\right) = \rho(\vec{v}\cdot\vec{f}^B) - (\vec{\nabla}\cdot p\vec{v}) + (\vec{\nabla}\cdot[\underline{\tau}\cdot\vec{v}]) - (\nabla\cdot\vec{q}) + \dot{q}_Q \tag{2.22}$$

The balance equation for mechanical energy, kinetic and potential, can be obtained by multiplying the momentum equation with the velocity vector. This leads to the equation of mechanical energy

$$\rho\frac{d}{dt}\left(\frac{1}{2}|\vec{v}|^2\right) = -(\vec{v}\cdot\vec{\nabla}p) + (\vec{v}\cdot[\vec{\nabla}\cdot\underline{\tau}]) + \rho(\vec{v}\cdot\vec{f}^B) \tag{2.23}$$

$$\rho \frac{d}{dt}\left(\frac{1}{2}|\vec{v}|^2\right) = p(\vec{\nabla}\cdot\vec{v}) - (\vec{\nabla}\cdot p\vec{v}) + (\vec{\nabla}\cdot[\underline{\tau}\cdot\vec{v}]) - (\tau:\vec{\nabla}\vec{v})$$
$$+ \rho(\vec{v}\cdot\vec{f}^B) \tag{2.24}$$

The term $(\tau:\vec{\nabla}\vec{v})$ is called the dissipation function and is often denoted as Φ_μ.

When subtracting the mechanical energy given by equation (2.24) from the total energy given by equation (2.22), the thermal energy remains

$$\rho\frac{de}{dt} = -p(\vec{\nabla}\cdot\vec{v}) + (\tau:\vec{\nabla}\vec{v}) - (\nabla\cdot\vec{q}) + \dot{q}_Q \tag{2.25}$$

By comparing equations (2.24) and (2.25) it can be seen that they only share the terms $p(\vec{\nabla}\cdot\vec{v})$ and $(\tau:\vec{\nabla}\vec{v})$ with different signs in each equation. Those terms represent the exchange of mechanical and thermal energy. Since the term $p(\vec{\nabla}\cdot\vec{v})$ can be positive or negative for expanding or compressing flow, it describes a reversible exchange of energy. The term $(\tau:\vec{\nabla}\vec{v})$ is always positive for Newtonian fluids and therefore represents the irreversible dissipation of mechanical into thermal energy.

The dissipation function for Newtonian fluids in cartesian coordinates is given by

$$\Phi_\mu = (\tau:\vec{\nabla}\vec{v}) = \mu\left\{2\left[\left(\frac{\partial u}{\partial x}\right)^2 + \left(\frac{\partial v}{\partial y}\right)^2 + \left(\frac{\partial w}{\partial z}\right)^2\right] + \left(\frac{\partial v}{\partial x} + \frac{\partial u}{\partial y}\right)^2\right.$$
$$\left. + \left(\frac{\partial w}{\partial y} + \frac{\partial v}{\partial z}\right)^2 + \left(\frac{\partial u}{\partial z} + \frac{\partial w}{\partial x}\right)^2 - \frac{2}{3}\left(\frac{\partial u}{\partial x} + \frac{\partial v}{\partial y} + \frac{\partial w}{\partial z}\right)^2\right\} \tag{2.26}$$

For incompressible flow $(\vec{\nabla}\cdot\vec{v} = 0)$ with small effects of viscous dissipation $(\tau:\vec{\nabla}\vec{v})$, the equations of mechanical and thermal energies are decoupled. In this case, the change of mechanical energy does not influence the thermal energy and vice versa.

There are many other formulations of the equation of thermal energy. For enthalpy and temperature it looks like

$$\rho\frac{dh}{dt} = \frac{dp}{dt} + (\tau:\vec{\nabla}\vec{v}) - (\nabla\cdot\vec{q}) + \dot{q}_Q \tag{2.27}$$

$$\rho c_p \frac{dT}{dt} = \frac{dp}{dt} + \left(\tau : \vec{\nabla}\vec{v}\right) - (\nabla \cdot \vec{q}) + \dot{q}_Q \tag{2.28}$$

2.2 Nondimensional parameters

For model tests it is important to know how to transfer measured results from the model to reality and vice versa. By non-dimensionalising the equations of motion it is possible to make them only relate on non-dimensional characteristic numbers. If these numbers are identical, then the non-dimensional flow fields are also equal. The main task of fluid dynamics is therefore to find the dependency between the solution of the equations of motion and these non-dimensional characterstic numbers.

The non-dimensionalisation of the momentum equation is done by the use of a characteristic velocity U and a characteristic length L. The * indicates a dimensionless quantity.

$$\vec{v}^* = \frac{1}{U}\vec{v}; \quad \vec{\nabla}^* = \vec{\nabla}L; \quad \Delta^* = \Delta L^2; \quad t^* = t\frac{U}{L}; \quad p^* = \frac{p}{\rho U^2}$$

Using these relations with the momentum equation (2.21), and omitting the volume forces $\vec{f}^B$, results in

$$\underbrace{\frac{\partial \vec{v}^*}{\partial t^*} + \left(\vec{v}^* \cdot \vec{\nabla}^*\right)\vec{v}^*}_{forces\ of\ inertia} = \underbrace{-\vec{\nabla}^* p^*}_{\substack{pressure \\ forces}} + \frac{1}{Re}\underbrace{\Delta^* \vec{v}^*}_{\substack{viscous \\ forces}} \tag{2.29}$$

Re is the Reynolds number that describes the ratio of the forces of inertia to the viscosity forces. Flows that have the same Reynolds number

$$Re = \frac{UL}{\nu} \tag{2.30}$$

are dynamically similar. For small Reynolds number, the viscous forces dominate over the forces of inertia. For high Reynolds numbers, the viscous forces can be neglected.

To transform the thermal energy equation (2.28) to dimensionless form, the following dimensionless quantities are used. Let U again denote a characteristic velocity, L a characteristic length, T_W the wall temperature, and the subscript R a reference value.

$$\vec{v}^* = \frac{\vec{v}}{U}; \quad \vec{\nabla}^* = \vec{\nabla}L; \quad \Delta^* = \Delta L^2; \quad t^* = t\frac{U}{L}$$

$$p^* = \frac{p}{\rho U^2}; \quad \phi_\mu^* = \frac{\phi}{\phi_R}; \quad T^* = \frac{T - T_R}{T_W - T_R}$$

The dimensionless energy equation without heat source is given by

$$\rho c_p \frac{dT^*}{dt^*} = Ec\,\frac{dp^*}{dt^*} + \frac{Ec}{Re}\Phi_\mu^* + \frac{1}{RePr}\Delta^* T^* \ , \tag{2.31}$$

where Ec is the Eckert number that describes the ratio of kinetic energy to the enthalpy difference.

$$Ec = \frac{U^2}{c_p(T_W - T_R)} \tag{2.32}$$

Pr denotes the Prandtl number, which describes the ratio of the diffusivities for momentum and enthalpy. It also describes the ratio of the velocity boundary layer thickness to the thermal boundary layer thickness and is about 1 for many gases at atmospheric state.

$$Pr = \frac{\nu}{a} = \frac{\nu \rho c_p}{\lambda} = \frac{\mu c_p}{\lambda} \tag{2.33}$$

For ideal gases the Eckert number can also be written as

$$Ec = \frac{U^2}{c_p(T_W - T_R)}\frac{c^2}{c^2} = Ma^2(\kappa - 1)\frac{T_R}{T_W - T_R} \ , \tag{2.34}$$

where $c = \sqrt{\kappa R T_R}$ is the speed of sound for an ideal gas, $Ma = U/c$ the Mach number and κ the isentropic exponent.

For flow with constant density ρ, the speed of sound c goes to infinity and therefore the Eckert number $Ec \ll 1$. This means that, for constant density ρ, the power of pressure forces and the power of the viscous forces can be neglected.

2.3 Laminar pipe flow

In experiments on fluid systems it is observed that, at values below the critical Reynolds number Re$_{crit}$, the flow is laminar. In laminar flow, the fluid flows in parallel layers without disruption between the layers. There is no motion perpendicular to the flow direction. For the laminar 2-dimensional fully developed flow, an exact solution of the Navier-Stokes equations is possible.

The stationary, axially symmetric flow of an incompressible Newtonian fluid through a pipe of infinite length can be described by the following equations, as shown by Brenn & Meile (2008).

Continuity equation

$$\frac{1}{r}\frac{\partial}{\partial r}(rv_r) + \frac{\partial u}{\partial z} = 0 \tag{2.35}$$

Momentum equation in radial direction

$$v_r\frac{\partial v_r}{\partial r} + u\frac{\partial v_r}{\partial z} = -\frac{1}{\rho}\frac{\partial p}{\partial r} + v\left[\frac{\partial}{\partial r}\left(\frac{1}{r}\frac{\partial}{\partial r}(rv_r)\right) + \frac{\partial^2 v_r}{\partial z^2}\right] + f_r^B \tag{2.36}$$

Momentum equation in axial direction

$$v_r\frac{\partial u}{\partial r} + u\frac{\partial u}{\partial z} = -\frac{1}{\rho}\frac{\partial p}{\partial z} + v\left[\frac{1}{r}\frac{\partial}{\partial r}\left(r\frac{\partial u}{\partial r}\right) + \frac{\partial^2 u}{\partial z^2}\right] + f_z^B \tag{2.37}$$

If the body force is neglected and the flow is fully developed, the continuity equation reduces to

$$r \cdot v_r = constant$$

Since the velocity v_r on the pipe wall $r = R$ must be zero v_r must be zero in the whole flow field. This leads to the simplified momentum equations

Momentum equation in radial direction

$$0 = -\frac{1}{\rho}\frac{\partial p}{\partial r} \quad,$$

hence the pressure p is no function of r.

Momentum equation in axial direction

$$0 = -\frac{1}{\rho}\frac{dp}{dz} + \nu\left[\frac{1}{r}\frac{d}{dr}\left(r\frac{du}{dr}\right)\right]$$

Since the term with ν does not depend on z, neither can $\frac{dp}{dz}$, and therefore it must be constant. After integration of the momentum equation in the axial direction, the velocity profile reads

$$\frac{1}{\mu}\frac{dp}{dz}r = \frac{d}{dr}\left(r\frac{du}{dr}\right)$$

$$\frac{1}{\mu}\frac{dp}{dz}\frac{r^2}{2} + C_1 = r\frac{du}{dr}$$

$$\frac{du}{dr} = \frac{1}{\mu}\frac{dp}{dz}\frac{r}{2} + \frac{C_1}{r}$$

$$u(r) = \frac{1}{4\mu}\frac{dp}{dz}r^2 + C_1\ln(r) + C_2$$

Since $u(r)$ needs to be finite for $r = 0$, $C_1 = 0$. At the wall $u(r = R) = 0$, which leads to parabolic velocity field

$$u(r) = -\frac{1}{4\mu}\frac{dp}{dz}R^2\left(1 - \frac{r^2}{R^2}\right) \tag{2.38}$$

The mean velocity can be calculated as

$$\bar{u} = \frac{\dot{V}}{A} = \frac{1}{R^2 \pi} \int_0^R u(r) 2r\pi dr = -\frac{1}{8\mu} \frac{dp}{dz} R^2 \qquad (2.39)$$

The maximum velocity follows as

$$u_{max} = u(r = 0) = -\frac{1}{4\mu} \frac{dp}{dz} R^2 = 2\bar{u} \qquad (2.40)$$

Using equation (2.40), the velocity field from equation (2.38) can be written as

$$u(r) = 2\bar{u} \left(1 - \frac{r^2}{R^2} \right) \qquad (2.41)$$

One can see that a pressure drop $\frac{dp}{dz}$ is necessary to drive the flow. This pressure drop has a negative value and is constant in the radial and axial directions. So $\frac{dp}{dz}$ is the pressure loss Δp on a pipe length L.

$$\frac{dp}{dz} = \frac{\Delta p}{L} = \frac{p_2 - p_1}{L}$$

This pressure loss is related to the shear stress τ_{rz} at the pipe wall

$$\tau_w = \tau_{rz}|_{r=R} = \mu \frac{du}{dr}\bigg|_{r=R} = \mu \frac{1}{2\mu} \frac{dp}{dz} R = \frac{R}{2} \frac{dp}{dz} \qquad (2.42)$$

The Darcy-Weisbach equation relates the pressure loss due to friction to the average velocity of the fluid flow.

$$-\Delta p = \lambda \frac{L}{D} \frac{\rho}{2} \bar{u}^2 \qquad (2.43)$$

where λ is the dimensionless friction factor. Hence the relation

$$-\frac{\Delta p}{L} = -\frac{dp}{dz} = \lambda \frac{1}{D} \frac{\rho}{2} \bar{u}^2$$

is obtained. From equation (2.39) we get

$$-\frac{dp}{dz} = -\frac{\Delta p}{L} = \frac{8\mu}{R^2}\bar{u} = \frac{32\mu}{D^2}\bar{u} = \underbrace{\frac{64\mu}{\rho D\bar{u}}}_{\lambda}\frac{1}{D}\frac{\rho}{2}\bar{u}^2$$

Comparing the last two equations we obtain the Hagen-Poisseuille friction law for laminar pipe flow.

$$\lambda = \frac{64\mu}{\rho D\bar{u}} = \frac{64}{Re} \tag{2.44}$$

This means that there is a linear correlation between the wall shear stress τ_w and the mean velocity $\bar{u}$ for laminar pipe flow

$$\tau_w = \frac{R}{2}\frac{dp}{dz} = \frac{4\mu}{R}\bar{u} \tag{2.45}$$

2.4 Turbulent flow

For Reynolds numbers higher than Re_{crit}, the flow is unstable and may eventually turn into turbulent. Turbulent flow has a three-dimensional, time dependent, random velocity $\vec{v}(\vec{x}, t)$ and pressure $p(\vec{x}, t)$ field. The fluctuating flow properties can be calculated at every location $\vec{x}$ and every time t with the Navier-Stokes equations. This method is called direct numerical simulation (DNS) and has to resolve all length and time scales. The computational costs of this method increase as Re^3. The DNS is therefore restricted to lower Reynolds numbers. For the technically relevant higher Reynolds numbers, average values of the flow properties are used to reduce the computation time. Generally, two main types of averaging are used

- *Statistical averaging*

  Instantaneous flow properties are split into the time-average and fluctuating components. This method is called Reynolds Averaged Numerical Simulation (RANS) and is described in chapter 2.4.1.

- *Local averaging (filtering)*

  Spatial filtering is used to separate the large scales from the small ones. The large eddies are resolved, and the influence of the small eddies is modelled. Simulating a flow field like this is called Large Eddy Simulation (LES), which will be described in chapter 2.5.

2.4.1 The Reynolds averaged transport equations (RANS)

The mathematical description of turbulence can be simplified by decomposing the instantaneous property ϕ (velocity, pressure, …) into a mean $\overline{\phi}$ and the fluctuations ϕ' around the mean $\overline{\phi}$

$$\phi = \overline{\phi} + \phi',$$

where $\overline{\phi'} = 0$

The ensemble average $\langle\phi\rangle$ of N samples is calculated by

$$\langle\phi\rangle(\vec{x}, t) = \frac{1}{N}\sum_{1}^{N}\phi(\vec{x}, t)$$

For statistically stationary flow the ensemble average $\langle\phi\rangle$ is equal to the time average $\overline{\phi}$

$$\overline{\phi}(\vec{x}) = \lim_{N\to\infty}\frac{1}{N}\sum_{1}^{N}\phi(\vec{x}, t) = \lim_{T\to\infty}\frac{1}{T}\int_{t_0}^{t_0+T}\phi(\vec{x}, t)dt.$$

The following rules apply when using these averages on fluctuating fluid properties $\phi = \overline{\phi} + \phi'$ and $\psi = \overline{\psi} + \psi'$, their combinations and derivatives.

$$\overline{\overline{\phi}} = \overline{\phi}; \quad \overline{\phi \pm \psi} = \overline{\phi} \pm \overline{\psi}; \quad \overline{\overline{\phi} \cdot \psi} = \overline{\phi} \cdot \overline{\psi}$$

$$\overline{\frac{\partial \overline{\phi}}{\partial s}} = \frac{\partial \overline{\phi}}{\partial s}; \quad \overline{\phi'} = \overline{\psi'} = 0$$

where s denotes x, y, z or t. Applying the decomposition of an instantaneous property into a mean and a fluctuation on the continuity (2.20) and momentum equations (2.21) without body force of an incompressible Newtonian fluid results in

$$\frac{\partial \bar{u}}{\partial x} + \frac{\partial \bar{v}}{\partial y} + \frac{\partial \bar{w}}{\partial z} = 0 \tag{2.46}$$

$$\frac{\partial u'}{\partial x} + \frac{\partial v'}{\partial y} + \frac{\partial w'}{\partial z} = 0 \tag{2.47}$$

$$\rho \left(\bar{u} \frac{\partial \bar{u}}{\partial x} + \bar{v} \frac{\partial \bar{u}}{\partial y} + \bar{w} \frac{\partial \bar{u}}{\partial z} \right) = -\frac{\partial \bar{p}}{\partial x} + \mu \Delta \bar{u} - \rho \left(\frac{\partial \overline{u'u'}}{\partial x} + \frac{\partial \overline{u'v'}}{\partial y} + \frac{\partial \overline{u'w'}}{\partial z} \right) \tag{2.48}$$

$$\rho \left(\bar{u} \frac{\partial \bar{v}}{\partial x} + \bar{v} \frac{\partial \bar{v}}{\partial y} + \bar{w} \frac{\partial \bar{v}}{\partial z} \right) = -\frac{\partial \bar{p}}{\partial y} + \mu \Delta \bar{v} - \rho \left(\frac{\partial \overline{u'v'}}{\partial x} + \frac{\partial \overline{v'v'}}{\partial y} + \frac{\partial \overline{v'w'}}{\partial z} \right) \tag{2.49}$$

$$\rho \left(\bar{u} \frac{\partial \bar{w}}{\partial x} + \bar{v} \frac{\partial \bar{w}}{\partial y} + \bar{w} \frac{\partial \bar{w}}{\partial z} \right) = -\frac{\partial \bar{p}}{\partial z} + \mu \Delta \bar{w} - \rho \left(\frac{\partial \overline{u'w'}}{\partial x} + \frac{\partial \overline{v'w'}}{\partial y} + \frac{\partial \overline{w'w'}}{\partial z} \right) \tag{2.50}$$

The terms $-\rho \left(\frac{\partial \overline{u'u'}}{\partial x} + \frac{\partial \overline{u'v'}}{\partial y} + \frac{\partial \overline{u'w'}}{\partial z} \right)$, $-\rho \left(\frac{\partial \overline{u'v'}}{\partial x} + \frac{\partial \overline{v'v'}}{\partial y} + \frac{\partial \overline{v'w'}}{\partial z} \right)$ and $-\rho \left(\frac{\partial \overline{u'w'}}{\partial x} + \frac{\partial \overline{v'w'}}{\partial y} + \frac{\partial \overline{w'w'}}{\partial z} \right)$ originate from the forces of inertia, but since they have the form of a stress tensor they are called apparent stresses of the turbulent flow or Reynolds stresses. These stresses are supplementary to the viscous stresses of a flow and are caused by the turbulent fluctuations. In general, the apparent turbulent stresses predominate over the viscous stresses.

$$\underline{\tau}_t = \underline{\sigma}' = \begin{pmatrix} \sigma'_{xx} & \tau'_{xy} & \tau'_{xz} \\ \tau'_{xy} & \sigma'_{yy} & \tau'_{yz} \\ \tau'_{xz} & \tau'_{yz} & \sigma'_{zz} \end{pmatrix} = - \begin{pmatrix} \rho \overline{u'u'} & \rho \overline{u'v'} & \rho \overline{u'w'} \\ \rho \overline{u'v'} & \rho \overline{v'v'} & \rho \overline{v'w'} \\ \rho \overline{u'w'} & \rho \overline{v'w'} & \rho \overline{w'w'} \end{pmatrix} \tag{2.51}$$

Since six new unknowns, namely the Reynolds stresses, appear, further equations are needed to calculate turbulent flow. This so-called closure problem can be solved by turbulence models that describe the relation between Reynolds stresses and the quantities of the mean motion.

The kinetic energy of the turbulent fluctuations is very important for turbulence modelling.

$$k = \frac{1}{2}\overline{q^2} = \frac{1}{2}\left(\overline{u'^2 + v'^2 + w'^2}\right) \tag{2.52}$$

$$q^2 = u'^2 + v'^2 + w'^2 \tag{2.53}$$

The balance of the quantity k can be derived from the Navier-Stokes equations, as shown by Gersten & Herwig (1992) on page 769. For steady flows and constant physical properties it reads

$$\underbrace{\rho\left(\vec{\overline{v}} \cdot \vec{\nabla}\mathrm{k}\right)}_{convection} = \underbrace{-\vec{\nabla} \cdot \left[\overline{\vec{v'}\left(p' + \frac{\rho}{2}q^2\right)}\right]}_{turbulent\ diffusion} + \underbrace{PRO}_{\substack{turbulence \\ production}} + \underbrace{DIF}_{\substack{viscous \\ diffusion}} - \underbrace{\rho\tilde{\varepsilon}}_{dissipation} \tag{2.54}$$

$$\begin{aligned} PRO = -\rho\Bigg(& \overline{u'u'}\frac{\partial\overline{u}}{\partial x} + \overline{u'v'}\frac{\partial\overline{v}}{\partial x} + \overline{u'w'}\frac{\partial\overline{w}}{\partial x} \\ & + \overline{u'v'}\frac{\partial\overline{u}}{\partial y} + \overline{v'v'}\frac{\partial\overline{v}}{\partial y} + \overline{v'w'}\frac{\partial\overline{w}}{\partial y} \\ & + \overline{u'w'}\frac{\partial\overline{u}}{\partial z} + \overline{v'w'}\frac{\partial\overline{v}}{\partial z} + \overline{w'w'}\frac{\partial\overline{w}}{\partial z}\Bigg) \end{aligned} \tag{2.55}$$

$$\begin{aligned} DIF = +\mu\Bigg[& \frac{\partial^2}{\partial x^2}\left(k + \overline{u'^2}\right) + \frac{\partial^2}{\partial y^2}\left(k + \overline{v'^2}\right) + \frac{\partial^2}{\partial z^2}\left(k + \overline{w'^2}\right) \\ & + 2\left(\frac{\partial^2\overline{u'v'}}{\partial x\partial y} + \frac{\partial^2\overline{v'w'}}{\partial y\partial z} + \frac{\partial^2\overline{w'u'}}{\partial z\partial x}\right)\Bigg] \end{aligned} \tag{2.56}$$

$$\begin{aligned} \rho\tilde{\varepsilon} = +\mu\Bigg[& 2\overline{\left(\frac{\partial u'}{\partial x}\right)^2} + 2\overline{\left(\frac{\partial v'}{\partial y}\right)^2} + 2\overline{\left(\frac{\partial w'}{\partial z}\right)^2} \\ & + \overline{\left(\frac{\partial u'}{\partial y} + \frac{\partial v'}{\partial x}\right)^2} + \overline{\left(\frac{\partial u'}{\partial z} + \frac{\partial w'}{\partial x}\right)^2} + \overline{\left(\frac{\partial v'}{\partial z} + \frac{\partial w'}{\partial y}\right)^2}\Bigg] \end{aligned} \tag{2.57}$$

The viscous diffusion and the dissipation are often combined as

$$DIF - \rho\tilde{\varepsilon} = \mu\Delta k - \rho\varepsilon \tag{2.58}$$

The term $\rho\varepsilon$ is some sort of pseudo-dissipation and reads

$$\rho\varepsilon = +\mu\left[\overline{\left(\frac{\partial u'}{\partial x}\right)^2} + \overline{\left(\frac{\partial v'}{\partial x}\right)^2} + \overline{\left(\frac{\partial w'}{\partial x}\right)^2}\right.$$
$$+ \overline{\left(\frac{\partial u'}{\partial y}\right)^2} + \overline{\left(\frac{\partial v'}{\partial y}\right)^2} + \overline{\left(\frac{\partial w'}{\partial y}\right)^2}$$
$$\left.+ \overline{\left(\frac{\partial u'}{\partial z}\right)^2} + \overline{\left(\frac{\partial v'}{\partial z}\right)^2} + \overline{\left(\frac{\partial w'}{\partial z}\right)^2}\right] \qquad (2.59)$$

Since the dissipation occurs in the smallest eddies where isotropic turbulence can be assumed, as shown by Kolmogorov (1941), the dissipation term simplifies to

$$\rho\tilde{\varepsilon} = 15\mu\,\overline{\left(\frac{\partial u'}{\partial x}\right)^2} \qquad (2.60)$$

2.4.1.1 Turbulent boundary layer

Similar to laminar flow, turbulent flows at high Reynolds numbers may have boundary layer character. The flow consists of two main regions, an inviscid outer flow and a thin turbulent boundary layer close to the wall. In analogy to laminar boundary layers, the fundamental equations can also be simplified for the turbulent case ($Re \to \infty$, $\bar{v} \ll U$, $\partial/\partial x \ll \partial/\partial y$). Equation (2.49) results in

$$0 = -\frac{\partial\bar{p}}{\partial y} - \rho\frac{\partial\overline{v'v'}}{\partial y} \qquad (2.61)$$

Integrating over the boundary layer thickness, and assuming a turbulence free outer flow ($\overline{v'v'} = 0$ for $y = 0$ and $y \to \infty$) leads to

$$\bar{p} + \rho\overline{v'v'} = \bar{p}_w = p_e \qquad (2.62)$$

This means that the pressure on the wall $\bar{p}_w$ and the pressure of the outer flow p_e are the same, as for the laminar case. The pressure inside the turbulent boundary layer $\bar{p}$ is not

constant, but the expression $\bar{p} + \rho\overline{v'v'}$ is. For constant physical fluid properties this leads to the following equations for the turbulent boundary layer

$$\frac{\partial \bar{u}}{\partial x} + \frac{\partial \bar{v}}{\partial y} = 0 \tag{2.63}$$

$$\rho\left(\bar{u}\frac{\partial \bar{u}}{\partial x} + \bar{v}\frac{\partial \bar{u}}{\partial y}\right) = -\frac{\partial p_e}{\partial x} + \frac{\partial}{\partial y}(\bar{\tau}_v + \tau_t) \tag{2.64}$$

with

$$\bar{\tau}_v = \mu\frac{\partial \bar{u}}{\partial y} \qquad \tau_t = -\rho\overline{u'v'} \tag{2.65}$$

A detailed derivation of the laminar and turbulent boundary layer equations can be found in Brenn & Meile (2008). For the simplified energy and k-equations please refer to Schlichting & Gersten (2006) on pages 514-515.

2.4.2 Turbulence modelling

A turbulence model provides additional equations that describe the correlation between the turbulent shear stress and the quantities of the mean motion. If the relation is given by algebraic equations, the model is called a zero-equation model. In general, partial differential equations are used that may contain even new unknowns, so that further model equations may be required. Depending on how many differential equations are used, these models are called one-equation model, two-equation model, etc.

At high Reynolds number, the turbulent boundary layer essentially consists of two layers, the viscous wall layer and the fully turbulent outer flow, in which viscosity effects may be neglected. Since the viscous wall layer becomes very thin at high Reynolds numbers it suffices, to compute the turbulent outer flow and the wall shear stress τ_W. A turbulence model is therefore only needed for the turbulent outer flow. The influence of viscosity is only introduced through the boundary condition, the universal law of the wall, that will be described in chapter 2.4.2.2.

At low Reynolds number, the whole flow field must be taken into account using a no-slip boundary condition at the wall.

2.4.2.1 Algebraic turbulence models

J. Boussinesq (1872) introduced a model for the turbulent shear stress τ_t in analogy to the Newtonian friction law.

$$\tau_t = \mu_t \frac{\partial \bar{u}}{\partial y} = \rho v_t \frac{\partial \bar{u}}{\partial y}, \tag{2.66}$$

where $\mu_t(x, y)$ and $v_t(x, y)$ are not material constants but depend on the location in the flow field. They are called eddy viscosity and kinematic eddy viscosity, respectively. The eddy viscosity is unknown but easier to model than the turbulent shear stress.

L. Prandtl (1925) also constructed a model that describes the relation between τ_t and $\frac{\partial \bar{u}}{\partial y}$. He assumed that the fluctuations originate from the displacement of fluid elements perpendicular to the flow. The mean displacement is called the mixing length l.

$$\tau_t = \rho l^2 \left| \frac{\partial \bar{u}}{\partial y} \right| \frac{\partial \bar{u}}{\partial y} \tag{2.67}$$

The mixing length $l(x, y)$ is still unknown, but easier to model. By comparing equations (2.66) and (2.67), the following relation can be obtained.

$$v_t = l^2 \left| \frac{\partial \bar{u}}{\partial y} \right| \tag{2.68}$$

A detailed description of those two models is given by Brenn & Meile (2008) or Schlichting & Gersten (2006).

2.4.2.2 The universal law of the wall

A fully developed Couette flow is a simple shear flow with constant shear stress in the whole flow field. The laminar case was described in detail e.g. by Brenn & Meile (2008)

and Schlichting & Gersten (2006). The turbulent Couette flow near the wall is of universal importance and therefore shall be investigated now.
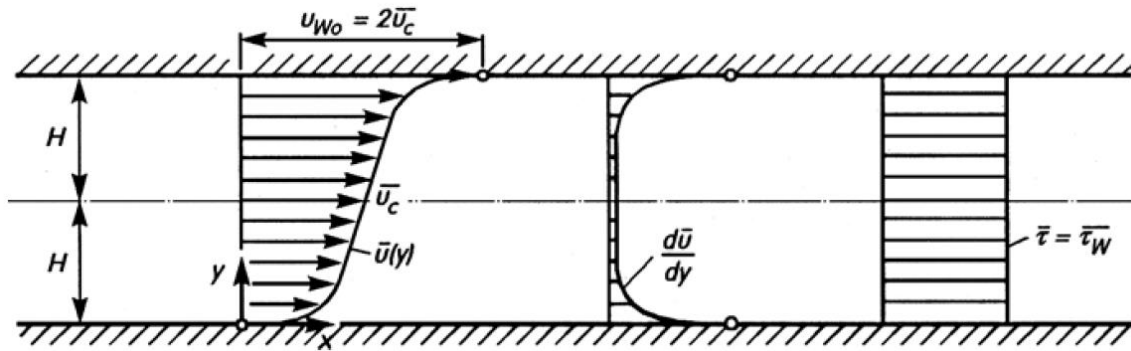
Figure 3: Turbulent Couette flow from Schlichting & Gersten (2006)

Since the flow is fully developed ($\partial \bar{u}/\partial x = 0$) it follows from equation (2.63) that $\bar{v} = 0$. This means that all inertial terms in equation (2.64) vanish. Since we look at a shear flow without external pressure gradient we get

$$\bar{\tau} = \bar{\tau}_v + \tau_t = \bar{\tau}_w = const \tag{2.69}$$

Using Prandtl's mixing length results in

$$\bar{\tau}_w = \bar{\tau}_v + \tau_t = \mu \frac{\partial \bar{u}}{\partial y} - \rho l^2 \left|\frac{\partial \bar{u}}{\partial y}\right| \frac{\partial \bar{u}}{\partial y} \tag{2.70}$$

By introducing the so-called friction velocity u_τ

$$u_\tau = \sqrt{\frac{\bar{\tau}_w}{\rho}} \tag{2.71}$$

and the following dimensionless quantities

$$u^+ = \frac{\bar{u}}{u_\tau}, \qquad y^+ = \frac{y u_\tau}{\nu}, \qquad l^+ = \frac{l u_\tau}{\nu} \tag{2.72}$$

we get

$$1 = \frac{\partial u^+}{\partial y^+} + l^{+2} \left|\frac{\partial u^+}{\partial y^+}\right| \frac{\partial u^+}{\partial y^+} \tag{2.73}$$

When we assume that the velocity rises with the distance to the wall ($\partial u^+/\partial y^+ > 0$), we can solve the quadric equation and get

$$\frac{\partial u^+}{\partial y^+} = \frac{2}{1 + \sqrt{1 + 4l^{+2}}} \tag{2.74}$$

Prandtl used

$$l = \kappa y\,, \quad l^+ = \kappa y^+ \tag{2.75}$$

to model the mixing length which was later improved by Van Driest (1956) who used the findings of Stokes (1851) to damp the mixing length near the wall.

$$l = \kappa y \left(1 - e^{-\frac{y}{A}}\right), \quad l^+ = \kappa y^+ \left(1 - e^{-\frac{y^+}{A^+}}\right) \tag{2.76}$$

The constant κ is called the Karman constant and has a value of $\kappa = 0.4$ which is based on many experiments. Following Van Driest (1956), the constant A^+ has a value of $A^+ = 26$. Integrating equation (2.74) yields

$$u^+(y^+) = \int_0^{y^+} \frac{2dy^+}{1 + \sqrt{1 + 4\kappa^2 y^{+2}\left(1 - e^{-\frac{y^+}{A^+}}\right)^2}} \tag{2.77}$$

Close to the wall, where $4\kappa^2 y^{+2} \ll 1$, we get

$$u^+ = y^+ \tag{2.78}$$

Far from the wall, where $4\kappa^2 y^{+2} \gg 1$, the velocity reads

$$u^+ = \frac{1}{\kappa}\ln(y^+) + B \tag{2.79}$$

Almost all turbulent flows with high Reynolds numbers and $\bar{\tau}_w \neq 0$ show such a velocity distribution. Therefore, equation (2.79) is called the universal law of the wall. The value for the constant B varies in different literature from $B = 5$ to $B = 5.5$
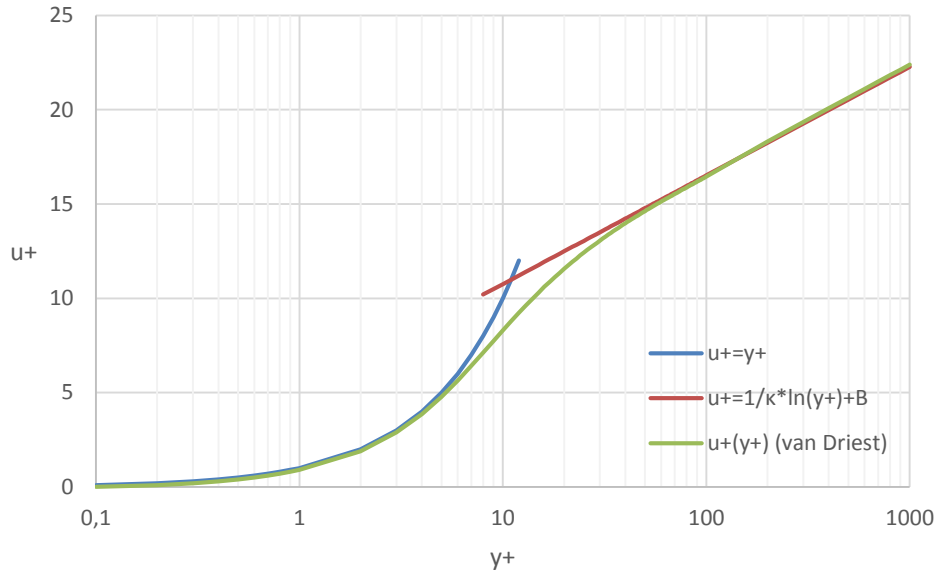
Figure 4: Viscous sublayer, logarithmic region and integrated equation (2.77)

2.4.2.3   Non-algebraic turbulence models

The various existing non-algebraic turbulence models are classified by the number of transport equations that are solved in addition to the RANS equations. All of them use the equation for the kinetic energy of the turbulent fluctuations (2.54), based on the work of Prandtl (1945). The turbulent diffusion is often modelled using

$$\overline{v'\left(p' + \frac{\rho}{2}q^2\right)} = -\frac{\rho \nu_t}{Pr}\frac{\partial k}{\partial y} \tag{2.80}$$

For the fully turbulent outer flow, where viscosity effects can be neglected, the k-equation reads

$$\underbrace{\bar{u}\frac{\partial k}{\partial x} + \bar{v}\frac{\partial k}{\partial y}}_{convection} = \underbrace{\frac{\partial}{\partial y}\left(\frac{\rho \nu_t}{Pr_k}\frac{\partial k}{\partial y}\right)}_{turb.\ diffusion} + \underbrace{\frac{\tau_t}{\rho}\frac{\partial \bar{u}}{\partial y}}_{turb.\ production} - \underbrace{\varepsilon}_{\substack{turbulence \\ dissipation}} \tag{2.81}$$

The model constant is often set to $Pr_k = 1$.

With the use of equation (2.66) ν_t can be replaced by τ_t and therefore two more equations for k and ε are needed to close the system. If one partial differential and one algebraic equation are used, the model is called a two-equation model. If it is assumed

that the eddy-viscosity $\nu_t = f(k, \varepsilon)$ is a function of k and ε, a dimensional analysis results in

$$\nu_t = c_\mu \frac{k^2}{\varepsilon} \qquad (c_\mu \approx 0.09) \tag{2.82}$$

Prandtl (1945) introduced the following relation to obtain the eddy viscosity

$$\nu_t = c_P L \sqrt{k} \qquad (c_P \approx 0.55) \tag{2.83}$$

where L denotes a mixing length that depends on the flow. The combination of equation (2.82) and (2.83) yields in the so-called Prandtl-Kolmogorov formula

$$L = c_\varepsilon \frac{k^{\frac{3}{2}}}{\varepsilon} \qquad \left(c_\varepsilon = \frac{c_\mu}{c_P} \approx 0.168\right) \tag{2.84}$$

The k-ε model

One of the most popular and widely used turbulence models is the two-equation k-ε model. It was developed by Jones & Launder (1972) and uses the k equation (2.81) and the following balance equation for the dissipation ε

$$\bar{u} \frac{\partial \varepsilon}{\partial x} + \bar{v} \frac{\partial \varepsilon}{\partial y} = \frac{\partial}{\partial y} \left(\frac{\nu_t}{Pr_\varepsilon} \frac{\partial \varepsilon}{\partial y}\right) + c_{\varepsilon 1} \frac{\varepsilon}{k} \frac{\tau_t}{\rho} \frac{\partial \bar{u}}{\partial y} - c_{\varepsilon 2} \frac{\varepsilon^2}{k} \tag{2.85}$$

with the model constants

$$Pr_k = 1, \quad Pr_\varepsilon = 1.3, \quad c_{\varepsilon 1} = 1.44, \quad c_{\varepsilon 2} = 1.87 \tag{2.86}$$

The boundary conditions for high Reynolds numbers are based on wall functions and on equilibrium between turbulence production and dissipation to avoid the need of resolving the high gradients near the wall.

Special low Reynolds number models exist that also resolve the region near the wall. They can make use of the simple boundary condition that all velocities vanish on the wall, but have to do the costly integration to the wall.

For a detailed review of various turbulence models refer to Patel, Rodi, & Scheurer (1985).

Reynolds stress models

In contrast to the eddy viscosity approach, these models introduce a transport equation for each term of the Reynolds stress tensor. This results in 6 additional equations and although the predictive capabilities are better, the computational costs are often too high.

2.4.3   Turbulent pipe flow

Looking at the momentum equation in the streamwise direction of a fully developed turbulent pipe flow we get

$$0 = -\frac{dp}{dz} + \frac{1}{r}\frac{d}{dr}(r \cdot \bar{\tau}) \tag{2.87}$$

$$\bar{\tau} = \rho v \frac{d\bar{u}}{dr} - \rho\overline{u'v'} = \bar{\tau}_v + \tau_t \tag{2.88}$$

As for the laminar case shown in chapter 2.3, the term $\frac{dp}{dz} < 0$ is constant. Integration leads to

$$\bar{\tau}(r) = \frac{r}{2}\frac{d\bar{p}}{dz} \tag{2.89}$$

On the wall we get

$$\tau_w = \bar{\tau}(R) = \frac{R}{2}\frac{d\bar{p}}{dz} = \frac{R}{2}\frac{\Delta p}{L} \tag{2.90}$$

This means that the wall shear stress can easily be determined by measuring the pressure drop Δp over a defined pipe length L.

The velocity profile of the turbulent pipe flow cannot be calculated analytically, but Nikuradse found that the universal law of the wall is a good approximation up to the pipe axis. Using these findings, we get the following correlation between the mean flow velocity $\bar{U}$ and the maximum velocity u_{max}.

$$\frac{u_{max} - \overline{U}}{u_{max}} = \frac{u_\tau}{u_{max}} \frac{3}{2\kappa} = \frac{1}{u_{max}^+} \frac{3}{2\kappa} \tag{2.91}$$

$$u_{max}^+ = \frac{1}{\kappa} lnR^+ + B, \quad \kappa = 0.4, \quad B = 5.5 \tag{2.92}$$

For the details of the derivation of equation (2.91) refer to Brenn & Meile (2008).

The turbulent pipe flow has nearly the same velocity over a wide area of the cross section, as shown in Figure 5. Near the wall, the velocity profile shows high gradients that cause the higher wall shear stress than in the laminar case.
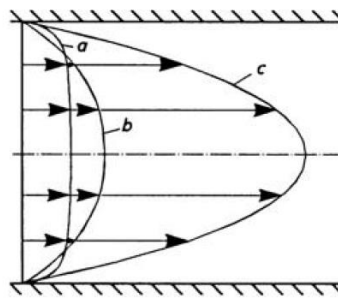
Figure 5: Velocity field in a pipe, (a) turbulent, (b) laminar with the same volume flow rate as a, (c) laminar with the same pressure gradient as a; from Schlichting & Gersten (2006)

The pressure loss for turbulent pipe flow was found to have a quadric correlation to the mean flow velocity, not a linear one as in the laminar case. Using equations (2.90) and (2.43) we get

$$\tau_w = \frac{R}{2} \frac{d\bar{p}}{dz} = \frac{R}{2} \lambda \frac{1}{D} \frac{\rho}{2} \overline{U}^2 = \frac{\lambda \rho}{8} \overline{U}^2 \tag{2.93}$$

The friction factor λ is not only a function of the Reynolds number, but also of the wall roughness. For smooth pipes, Blasius (1911) found an empirical formula for the friction factor for Reynolds numbers $Re \le 10^5$

$$\lambda = 0.3164 \cdot Re^{-\frac{1}{4}} \tag{2.94}$$

Prandtl derived an implicit correlation from the universal law of the wall for smooth pipes and high Reynolds numbers $Re > 10^5$

$$\frac{1}{\sqrt{\lambda}} = 2 \log\left(Re \cdot \sqrt{\lambda}\right) - 0.8 \tag{2.95}$$

New measurements by Gersten K. (2004) at high Reynolds numbers showed that the constants 2 and -0.8 should be 1.934 and -0.554 instead.

2.5 Large eddy simulation (LES)

A turbulent flow contains a wide range of length and time scales. Direct Numerical Simulation (DNS) has to resolve all those scales, which means vast computational costs. The smallest scales of a turbulent flow are defined as

$$\eta = \left(\frac{\nu^3}{\epsilon}\right)^{\frac{1}{4}}, \quad \tau = \left(\frac{\nu}{\epsilon}\right)^{\frac{1}{2}} \tag{2.96}$$

where η is the Kolmogorov length scale, τ is the Kolmogorov time scale, ϵ is the dissipation of turbulent kinetic energy and ν is the kinematic viscosity. This means that the smallest scales, where energy is dissipated, depend on both the dissipation rate and the viscosity. For a statistically steady turbulent flow, the dissipated energy at small scales must equal the energy supplied by the larger scales. If L denotes the length of the largest eddies, then the ratio between the largest and the smallest scales can be approximated as

$$\frac{L}{\eta} \approx Re^{\frac{3}{4}} \tag{2.97}$$

This means that, with increasing Reynolds number, the range between largest and smallest scales also increases. In 3 dimensions, the required number of grid points to resolve all scales is given by $N_{min} = Re^{(9/4)}$. This is the reason why DNS is still limited to lower Reynolds number flow problems.

A Large Eddy Simulation (LES) only resolves the large eddies of the flow and models the effect of the smaller eddies, the so-called Sub Grid Scales (SGS), as shown in Figure 6.
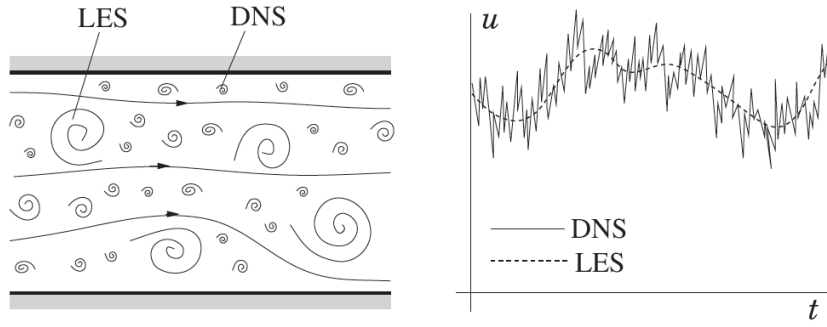
Figure 6: Schematic representation of turbulent fluid motion (left) and velocity over time for one point in the flow (right); from Ferziger & Perić (2008)

This is reasonable, since the large eddies transport the principal turbulent momentum and energy. Energy is transferred from larger to smaller eddies. Small eddies have a more universal character and are mainly responsible for the dissipation of the turbulent kinetic energy. The large eddies are resolved by a spatially filtered set of conservation equations, whereas the influence of the small eddies are modelled by so-called SGS models. Often used spatial filter methods are the box filter and the Gaussian filter. The general filtering operation for one dimension is defined by

$$\overline{F}(x,t) = \int G(r)F(x-r,t)\,dr, \qquad (2.98)$$

where the homogeneous filter function $G(r)$ satisfies the normalization condition

$$\int G(r)dr = 1. \qquad (2.99)$$

Let r denote the filter radius, then the filter width is defined as $\Delta = 2r$. In 3D CFD often implicit filtering is used. This means that the spatial discretization defines the filter operation and that the filter width is unknown. The filtering operation is used to decompose, e.g., the velocity component $u(\vec{x},t)$ into the sum of a filtered component $\bar{u}(\vec{x},t)$ and a residual component $u'(\vec{x},t)$. The result appears analogous to the Reynolds decomposition.

$$u(\vec{x},t) = \bar{u}(\vec{x},t) + u'(\vec{x},t) \qquad (2.100)$$

The important difference is that, in general,

$$\overline{u'}(\vec{x}, t) \neq 0 \tag{2.101}$$

The resulting filtered continuity equation for incompressible flow is equal to the Reynolds decomposition case.

$$\frac{\partial \bar{u}}{\partial x} + \frac{\partial \bar{v}}{\partial y} + \frac{\partial \bar{w}}{\partial z} = 0 \tag{2.102}$$

$$\frac{\partial u'}{\partial x} + \frac{\partial v'}{\partial y} + \frac{\partial w'}{\partial z} = 0 \tag{2.103}$$

The filtered Navier-Stokes equations in conservative form read

$$\frac{\partial \bar{u}_i}{\partial t} + \frac{\partial \overline{u_i u_j}}{\partial x_j} = -\frac{1}{\rho}\frac{\partial \bar{p}}{\partial x_i} + v\frac{\partial^2 \bar{u}_i}{\partial x_j^2} \tag{2.104}$$

The residual or SGS stress tensor is defined by

$$\tau_{ij}^R = \overline{u_i u_j} - \bar{u}_i \bar{u}_j \tag{2.105}$$

This leads to

$$\frac{\partial \bar{u}_i}{\partial t} + \frac{\partial \bar{u}_i \bar{u}_j}{\partial x_j} = -\frac{1}{\rho}\frac{\partial \bar{p}}{\partial x_i} + \frac{\partial}{\partial x_j}\left(v\frac{\partial \bar{u}_i}{\partial x_j} - \tau_{ij}^R\right) \tag{2.106}$$

Similar to the RANS equations, the system of filtered equations is not closed, because the SGS stress tensor is unknown and must therefore be modelled.

2.5.1 Smagorinsky model

The most commonly used SGS model was proposed by Smagorinsky (1963). It is an eddy viscosity model and uses the following equation to relate the SGS stress τ_{ij}^R to the filtered strain rate tensor $\bar{S}_{ij}$

$$\tau_{ij}^R - \frac{1}{3}\tau_{ii}^R \delta_{ij} = v_t\left(\frac{\partial \bar{u}_i}{\partial x_j} + \frac{\partial \bar{u}_j}{\partial x_i}\right) = 2v_t \bar{S}_{ij} \tag{2.107}$$

where

$$\bar{S}_{ij} = \frac{1}{2}\left(\frac{\partial \bar{u}_j}{\partial x_i} + \frac{\partial \bar{u}_i}{\partial x_j}\right) \tag{2.108}$$

In analogy to the mixing length, the eddy viscosity ν_t is modelled as

$$\nu_t = l_s^2|\bar{S}| = (C_s\Delta)^2|\bar{S}| \tag{2.109}$$

where

$$|\bar{S}| = \sqrt{2\bar{S}_{ij}\bar{S}_{ij}} \tag{2.110}$$

$\bar{S}$ is the filtered rate of strain, l_s is the Smagorinsky length scale, $\Delta = (\Delta_1\Delta_2\Delta_3)^{1/3}$ is the filter width, and C_s is the Smagorinsky coefficient. The value of C_s is not constant but depends on the flow regime. It is zero for laminar flow, and $C_s \approx 0.15$ in high Reynolds number free turbulent flow. Near walls it needs to be attenuated, since $l_s \approx y^{\wedge}(3/2)$ which is often achieved by a Van Driest damping function

$$l_s = C_s\Delta\left(1 - e^{\frac{y^+}{A^+}}\right), \tag{2.111}$$

where the constant A^+ often has a value of $A^+ = 25$.

So-called dynamic Smagorinsky models determine a local appropriate value for the Smagorinsky coefficient C_s. For a more detailed description refer to Pope (2000).

2.5.2 Coherent structure model (CSM)

This SGS model is based on the relation of coherent structures in grid-scale flow fields and SGS energy dissipation and was proposed by Kobayashi (2005). The advantages over the Smagorinsky model are that a Van Driest damping function near walls is not needed, the model parameter is determined locally, and that it is also applicable to laminar flows. The eddy viscosity ν_t is defined as

$$\nu_t = C_{CSM}\Delta^2|\bar{S}| \tag{2.112}$$

The model parameter C_{CSM} is determined locally and is always positive

$$C_{CSM} = C_1 |F_{CS}|^{\frac{3}{2}} F_\Omega \tag{2.113}$$

The coherent structure function F_{CS} is defined as the second invariant Q of the velocity gradient tensor in grid scale flow fields normalized by the magnitude of a velocity gradient tensor E and plays the role of wall damping. F_Ω denotes the energy-decay suppression function needed for rotating flows.

$$F_{CS} = \frac{Q}{E} \tag{2.114}$$

$$F_\Omega = 1 - F_{CS} \tag{2.115}$$

The constant C_1 has the value

$$C_1 = \frac{1}{22} \tag{2.116}$$

The coherent structure is extracted by the second invariant Q which is given by

$$Q = \frac{1}{2}\left(\overline{W}_{ij}\overline{W}_{ij} - \bar{S}_{ij}\bar{S}_{ij}\right) = -\frac{1}{2}\frac{\partial \bar{u}_j}{\partial x_i}\frac{\partial \bar{u}_\iota}{\partial x_j} \tag{2.117}$$

where $\overline{W}_{ij}$ is the grid scale vorticity tensor and $\bar{S}_{ij}$ the grid scale strain rate tensor from equation (2.108).

$$\overline{W}_{ij} = \frac{1}{2}\left(\frac{\partial \bar{u}_j}{\partial x_i} - \frac{\partial \bar{u}_\iota}{\partial x_j}\right) \tag{2.118}$$

The magnitude of the velocity gradient tensor E is given by

$$E = \frac{1}{2}\left(\overline{W}_{ij}\overline{W}_{ij} + \bar{S}_{ij}\bar{S}_{ij}\right) = \frac{1}{2}\left(\frac{\partial \bar{u}_j}{\partial x_i}\right)^2 \tag{2.119}$$

Since $\overline{W}_{ij}\overline{W}_{ij}$ and $\bar{S}_{ij}\bar{S}_{ij}$ are always positive, the value of F_{CS} has definite upper and lower limits of

$$-1 \leq F_{CS} \leq 1 \tag{2.120}$$

As a result, the model parameter C_{CSM} has a very narrow range, making the CSM model very stable even though the parameter is locally determined.

2.6 Multiphase flow

If the phase denotes the state of matter and can be solid, liquid or gas, a multiphase flow is the flow of a fluid with several phases. This can be two liquids, liquid and vapor from the same substance, liquid and a permanent gas or solids inside the flow domain. There are different methods available to simulate multiphase flows.

2.6.1 Euler-Eulerian

With the Euler-Eulerian method, all phases are described in the Eulerian frame of reference. If the discretization is fine enough, the interface between different phases can be tracked, but due to the computational effort this is often not reasonable or even feasible. Therefore, average values of the volume fraction, the velocity and the density for the phases in a cell are computed. The interface is not tracked, but the gradient of the phase volume fraction indicates its position for larger scaled surfaces. The mass conservation equation for each phase k is represented by

$$\frac{\partial \alpha_k \rho_k}{\partial t} + \nabla \cdot \alpha_k \rho_k \vec{v}_k = \sum_{l=1, l \neq k}^{n_{ph}} \Gamma_{kl} \tag{2.121}$$

α_k is the volume fraction of phase k, n_{ph} is the number of phases and Γ_{kl} represents the interfacial mass exchange between phases k and l. The compatibility condition

$$\sum_{k=1}^{n_{ph}} \alpha_k = 1 \tag{2.122}$$

must be satisfied. The momentum conservation equation equals

$$\frac{\partial \alpha_k \rho_k \vec{v}_k}{\partial t} + \nabla \cdot \alpha_k \rho_k \vec{v}_k \vec{v}_k = -\alpha_k \nabla p + \nabla \cdot \alpha_k \left(\underline{\tau}_k + \underline{\tau}_k^t \right) + \alpha_k \rho_k \vec{f}^B$$

$$+ \sum_{l=1, l \neq k}^{n_{ph}} M_{kl} + \sum_{l=1, l \neq k}^{n_{ph}} \vec{v}_{kl} \Gamma_{kl} \tag{2.123}$$

where $\vec{f}^B$ is the body force vector, M_{kl} represents the momentum interfacial interaction between phases k and l. The pressure p is assumed to be identical for all phases. The term $\vec{v}_{kl} \Gamma_{kl}$ represents the interfacial momentum transfer due to mass transfer. The phase k shear stress tensor $\underline{\tau}_k$ assuming a Newtonian fluid is given as

$$\tau_{k,ij} = \mu_k \left[\left(\frac{\partial U_{k,i}}{\partial x_j} + \frac{\partial U_{k,j}}{\partial x_i} \right) - \frac{2}{3} \delta_{ij} \frac{\partial U_{k,m}}{\partial x_m} \right] , \tag{2.124}$$

where μ_k is the molecular viscosity. The Reynolds stress thensor $\underline{\tau}_k^t$ reads

$$\tau_{k,ij}^t = -\rho_k \overline{u'_{k,i} u'_{k,j}} = \mu_k^t \left[\left(\frac{\partial U_{k,i}}{\partial x_j} + \frac{\partial U_{k,j}}{\partial x_i} \right) - \frac{2}{3} \delta_{ij} \frac{\partial U_{k,m}}{\partial x_m} \right] - \frac{2}{3} \delta_{ij} \rho_k k_k \tag{2.125}$$

2.6.2 Surface tracking with the Volume of Fluid (VOF) model

In VOF models, the different fluids are modeled as single continua with variable properties. Therefore, only a single set of momentum equations is solved using mixture properties of all fluids. The central idea behind the VOF model is to solve a scalar transport equation for the volume fraction equation. For incompressible flow this equation reads

$$\frac{\partial \alpha}{\partial t} + \nabla \cdot \alpha \vec{v} = 0 \tag{2.126}$$

where α is the volume fraction of the tracked phase and $\vec{v}$ the velocity of the flow. Assuming a flow with two phases, the possible values of the volume fraction α of phase 2 for each computational cell are

$$\alpha = \begin{cases} 0 & \textit{the cell is fully occupied by phase 1} \\ 0 < \alpha < 1 & \textit{the cell contains part of the phase interface} \\ 1 & \textit{the cell is fully occupied by phase 2} \end{cases} \tag{2.127}$$

The main difficulty of the VOF method lies in the discretization of the convective term of equation (2.127). Special schemes are necessary to prevent smearing of the interface caused by numerical diffusion and unphysical values of the volume fraction α caused by oscillations. Schemes that ensure that the advected volume fraction field is bounded and monotonic are often based on the Donator-Acceptor differencing scheme proposed by Ramshaw & Trapp (1976).

In many flows with fluid interfaces, the surface tension on the interface plays an important role. Based on the Continuum Surface Force (CSF) model Brackbill, Kothe, & Zemach (1992), the surface tension effects can be treated as a body force

$$f_\sigma = \int_V \sigma \kappa \nabla \alpha dV \tag{2.128}$$

where σ is the surface tension assumed to be constant, and κ is the curvature calculated by

$$\kappa = -(\nabla \cdot \vec{n}) = -\nabla \cdot \frac{\nabla \alpha}{|\nabla \alpha|} \quad , \tag{2.129}$$

where $\vec{n}$ is the unit normal vector on the interface.

2.6.3   Discrete Droplet Model (DDM)

The Discrete Droplet Model is an Euler-Lagrangian approach for simulating dilute dispersed liquid phases in multiphase flows. The dispersed liquid phase is described in the Lagrangian frame of reference, while the continuous phase is described in the Eulerian frame. Fluid particles or droplets that share similar properties like diameter, velocity or temperature are grouped to so-called parcels. The momentum equation for a parcel reads

$$m_d \frac{d\vec{u}_{id}}{dt} = \vec{F}_{idr} + \vec{F}_{ig} + \vec{F}_{ip} + \vec{F}_{ivm} + \vec{F}_{ib} \quad , \tag{2.130}$$

where m_d is the particle mass and $\vec{F}_{idr}$ is the drag force, given by

$$\vec{F}_{idr} = \frac{1}{2}\rho_g A_d C_D |\vec{u}_{rel}|\vec{u}_{rel} \quad .$$

(2.131)

ρ_g is the gas density, A_d the cross-sectional area of the droplet, C_D the drag coefficient, which is generally a function of the particle Reynolds number, and $\vec{u}_{rel}$ the relative velocity between the parcel and the gas. $\vec{F}_{ig}$ denotes a force including gravity and buoyancy

$$\vec{F}_{ig} = V_p(\rho_d - \rho_g)\vec{g} \quad ,$$

(2.132)

where V_p is the volume of the parcel, ρ_d the droplet density and $\vec{g}$ the gravity force vector. The pressure force $\vec{F}_{ip}$, the virtual mass force $\vec{F}_{ivm}$ taking into account acceleration of the medium surrounding the drops, and external forces $\vec{F}_{ib}$ (electrostatic, magnetic) are often neglected due to their minor magnitude in spray injection compared to the drag force. Dividing equation (2.130) by the particle mass m_d and inserting the relevant forces results in

$$\frac{d\vec{u}_{id}}{dt} = \frac{3}{4}C_D\frac{\rho_g}{\rho_d}\frac{1}{D_d}|\vec{u}_g - \vec{u}_d|(\vec{u}_g - \vec{u}_d) + \left(1 - \frac{\rho_g}{\rho_d}\right)\vec{g}$$

(2.133)

where D_d is the droplet diameter, $\vec{u}_g$ is the velocity of the continuous phase and $\vec{u}_d$ is the current parcel velocity. The new parcel velocity $\vec{u}_{id}$ can then be calculated by integration of equation (2.133). Another integration yields the particle position vector.

The effect of the dispersed phase on the continuous phase is modelled via source terms in the conservation equations of the continuous phase.

2.7   Spray formation

Depending on the properties of the liquid and the surrounding gas, and on the relative velocity, the breakup of a liquid jet is governed by different breakup mechanisms. These mechanisms are usually characterized by the distance between the nozzle and the point of first droplet formation, the so-called breakup length, and the size of the droplets produced by the breakup.

2.7.1 Breakup regimes

Ohnesorge (1931) showed that the disintegration process can be classified by three regimes using the liquid Weber number

$$We_l = \frac{u^2 D \rho_l}{\sigma} \tag{2.134}$$

and the Reynolds number

$$Re = \frac{u D \rho_l}{\mu_l} \tag{2.135}$$

Another characteristic number called the Ohnesorge number is a function of Re and We as per

$$Oh = \frac{\sqrt{We_l}}{Re} = \frac{\mu_l}{\sqrt{\sigma \rho_l D}} \tag{2.136}$$

where u is the jet velocity, D the nozzle diameter, ρ_l the liquid density, μ_l the dynamic viscosity of the liquid and σ the surface tension at the liquid-gas interface.
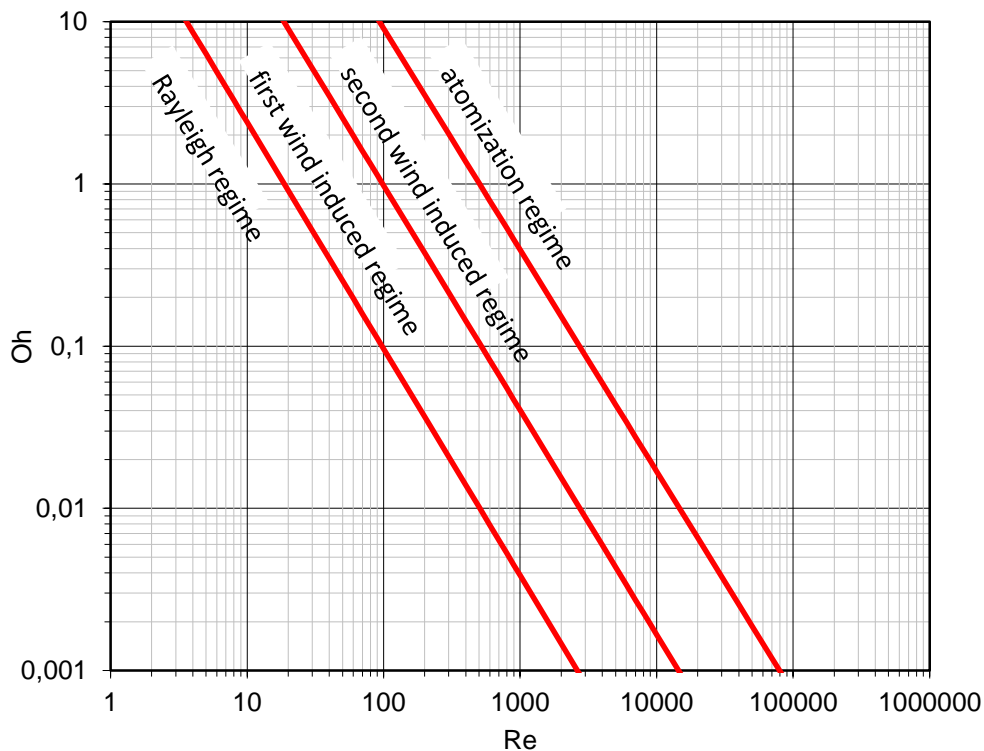
Figure 7: Ohnesorge nomogram in the version by Reitz & Bracco (1986)

Since the definition of the Ohnesorge number only contains liquid properties it was suggested by, e.g., Reitz (1978) to include the gas to liquid density ratio and extend the nomogram to three dimensions. This means that, for higher gas to liquid density ratio, the division lines between the different regimes are moved to lower Reynolds numbers.

According to Reitz & Bracco (1986) the following breakup regimes can be distinguished:

A) Dripping regime

In this regime, the liquid velocity in the nozzle is very small and drops are directly emitted from the nozzle when the surface tension cannot compensate the gravity anymore. The drops are very large.

B) Rayleigh regime

At higher jet velocity, an intact liquid column with a cylindrical surface can develop. Axially symmetric perturbations growing due to capillarity can lead to detachment of drops when the amplitude has become equal to the jet radius. The diameter of the detached drop is larger than the nozzle diameter. The distance to the nozzle where a drop is formed increases with the jet velocity at the nozzle orifice.

C) First wind-induced regime

As the velocity is further increased, the perturbations are amplified by aerodynamic forces. This leads to a decrease of the breakup length and smaller drops. The drop size is of the order of the nozzle diameter.

D) Second wind-induced regime

The unstable growth of short wavelength surface waves on the jet surface due to the relative motion of the jet and the ambient gas as well as turbulence that disrupt the jet surface lead to separation of drops from the jet core. The drop formation now no longer

occurs at the tip of the jet only, but drops are separated from the jet surface forming a cloud of small droplets that surround the jet core. The liquid core length increases with the initial velocity.

E) Atomization regime

This regime is characterized by a complete disruption of the jet from the nozzle exit on. The drop diameters are much smaller than the nozzle diameter. The liquid core is hidden inside the dense spray near the nozzle orifice, and its length is therefore hard to measure.

2.7.2   Stability curve

The correspondence of jet velocity and breakup length has been studied experimentally by many investigators. In the laminar flow regime, the breakup length increases linearly with the velocity. In the transition regime, the breakup length decreases, and it increases again in the turbulent flow region. If the jet velocity is increased further, the shape of the stability curve is uncertain. A review of results from different authors can be found in McCarthy & Molloy (1974) and Dumouchel (2008). Figure 8 shows a stability curve and illustrations of the breakup regimes, taken from Balewski (2009).
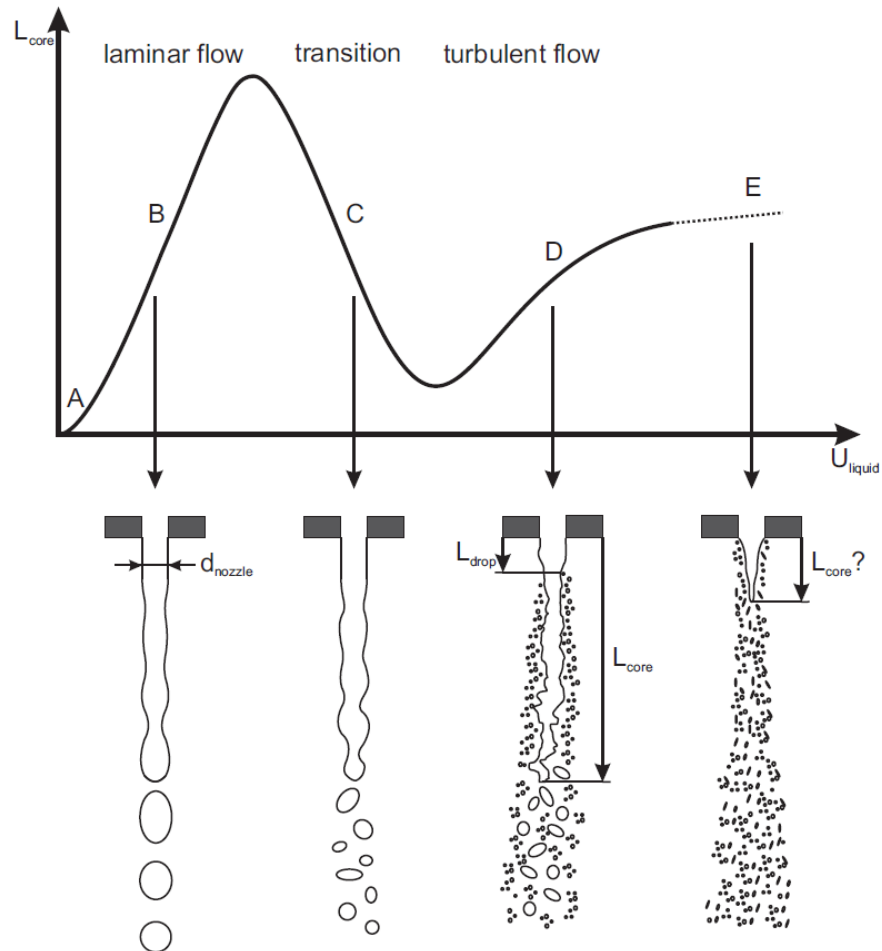
Figure 8: Stability curve and breakup regimes from Balewski (2009). The regions A, B, C, D and E correspond to the dripping, Rayleigh, first wind-induced, second wind-induced and atomization regime, respectively.

2.7.3   Mechanisms of primary breakup

The breakup of directly injected fuel jets usually lies within the atomization regime. Only during a short time at the beginning and at the end of injection, other regimes are relevant. Within the atomization regime, the breakup of the jet can be divided into two parts. First, the jet disintegrates into ligaments and larger droplets, named primary breakup. Then the subsequent secondary breakup driven by aerodynamic forces further reduces the droplet sizes. The dominant mechanism of the primary breakup is not as clear as for the secondary breakup. Reviewing various works, e.g. Baumgarten (2006), depicted four possible mechanisms of primary breakup, as shown in Figure 9.
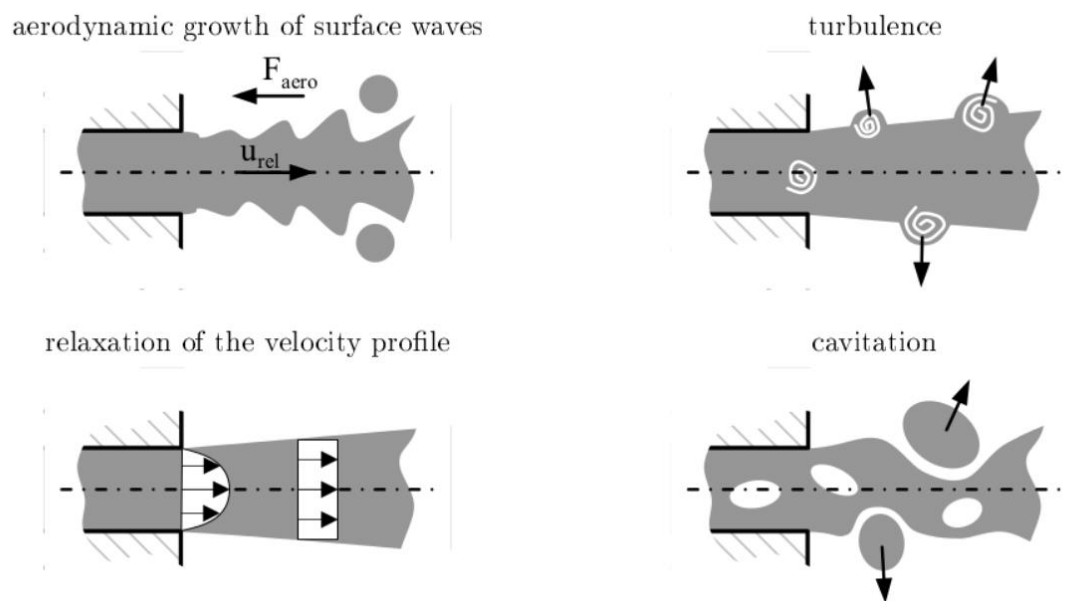
Figure 9: Possible primary breakup mechanisms Baumgarten (2006)

Due to the liquid turbulence created inside the nozzle and other excitations coming, e.g., from the fuel pump and the needle movement, the jet surface is deformed by a spectrum of small surface waves. Some of these surface waves are amplified by aerodynamic shear forces, become unstable and separate from the jet forming primary ligaments. The unstable surface waves grow at a finite rate with time and can therefore not explain the immediate breakup of a jet at the nozzle orifice.

It is also believed that turbulence has a great impact on primary breakup. If turbulence is strong enough, turbulent eddies can overcome the surface tension and separate from the jet.

For fully developed pipe flow (large L/D ratios), the velocity profile may change at the instant when the jet leaves the nozzle due to the removed wall boundary condition. The viscous forces accelerate the outer region of the jet and may destabilize the jet surface and lead to breakup.

Cavitation induced disintegration also seems to be of big importance. The intensity and spatial structure of cavitation strongly depends on the nozzle geometry. When cavitation bubbles reach the nozzle orifice, they implode due to the high pressure of the ambient gas. It is unclear if this collapse energy increases turbulence or leads to direct disintegration of the jet.

A review of the mechanisms that influence the stability of a jet can be found in McCarthy & Molloy (1974).

2.7.4   The Blob Injection model

The most popular method to initialize the simulation of spray formation is the so-called blob injection method developed by Reitz & Diwakar (1987). The method assumes that atomization and drop breakup are indistinguishable processes within the dense spray near the nozzle exit. Spherical drops (blobs) with the diameter of the nozzle orifice are injected, which are then subject to secondary aerodynamic induced breakup. The number of drops injected per time step and the initial velocity of the drops are calculated from the mass flow rate. The spray cone angle must be defined so the drops can get a randomly chosen radial velocity component.

2.7.5   The Taylor Analogy Breakup (TAB) model

The Taylor Analogy Breakup model was proposed by O'Rourke & Amsden (1987). It is based on an analogy between a forced oscillating spring-mass system and an oscillating drop. The external force F corresponds to the aerodynamic forces that deform the droplet and amplify the oscillation. The surface tension tries to keep the spherical form of the drop and therefore corresponds to the spring force. The liquid viscosity causes friction forces inside the droplet and corresponds to the damping force. The equation of motion of the damped spring-mass system reads

$$m\ddot{x} = F - kx - d\dot{x} \tag{2.137}$$

where x is the displacement of the equator of the droplet from its equilibrium position, m the droplet mass, k the spring constant, and d the damping rate. In accordance with the analogy, the coefficients in (2.137) are

$$\frac{F}{m} = C_F \frac{\rho_g u_{rel}^2}{\rho_l r}, \quad \frac{k}{m} = C_k \frac{\sigma}{\rho_l r^3}, \quad \frac{d}{m} = C_d \frac{\mu_l}{\rho_l r^2} \tag{2.138}$$

Using the dimensionless displacement $y = x/(C_b r)$, the equation of motion reads

$$\ddot{y} = \frac{C_F}{C_b} \frac{\rho_g}{\rho_l} \frac{u_{rel}^2}{r^2} - C_k \frac{\sigma}{\rho_l r^3} y - C_d \frac{\mu_l}{\rho_l r^2} \dot{y} \qquad (2.139)$$

C_F, C_k, C_d and C_b are model constants, ρ_g and ρ_l are the gas and liquid densities, r is the spherical droplet radius and μ_l is the liquid viscosity. Assuming constant u_{rel}, which is appropriate for a small time step during a simulation, the analytical solution of equation (2.139) is

$$y(t) = \frac{C_F}{C_k C_b} We_g + e^{-\frac{t}{t_d}} \left[A \cdot cos(\omega t) + \frac{1}{\omega t_d} B \cdot sin(\omega t) \right] \qquad (2.140)$$

where

$$A = \left(y_0 - \frac{C_F}{C_k C_b} We_g \right), \quad B = \left(\dot{y}_0 t_d + y_0 - \frac{C_F}{C_k C_b} We_g \right) \qquad (2.141)$$

with

$$We_g = \frac{\rho_g u_{rel}^2 r}{\sigma}, \quad \frac{1}{t_d} = \frac{C_d \mu_l}{2 \rho_l r^2}, \quad \omega^2 = C_k \frac{\sigma}{\rho_l r^3} - \frac{1}{t_d^2} \qquad (2.142)$$

In contrast to other definitions, the Weber number We_g is defined with the droplet radius and not the diameter. y_0 and $\dot{y}_0$ are the position and velocity of the drop equator at $t = 0$. When used in combination with the blob injection model, these values are often set to $y_0 = \dot{y}_0 = 0$. The TAB model only accounts for the fundamental oscillation mode corresponding to the lowest order spherical harmonic, which is the most important one for lower Weber numbers, as discussed by O'Rourke & Amsden (1987). It is assumed that breakup occurs only if $x \geq 0.5r$, which results in $C_b = 1/2$ and $y \geq 1$. For a Weber number lower than the critical Weber number $We_{g,crit} \approx 6$ (determined in experiments), no breakup occurs. The remaining model constants are determined as

$$C_b = \frac{1}{2}, \quad C_k = 8, \quad C_d = 5, \quad C_F = \frac{1}{3} \qquad (2.143)$$

Equation (2.140) allows for the computation of the droplet breakup time.

The TAB model is also able to predict the spray angle. New droplets get the velocity of the old drop plus an additional radial velocity component

$$|\vec{v}_n| = C_v C_b r |\dot{y}|, \quad C_v \approx 1.0 \tag{2.144}$$

This radial velocity component is equal to the deformation velocity of the old drop at the time of breakup. The exact direction of $\vec{v}_n$ is sampled randomly.

The TAB model results in a complete disintegration of the old drop into a number of new drops. The number and size of these new drops are determined by an energy balance of the kinetic energy of the oscillation and the surface energy before and after breakup. The radius of the new drops is randomly chosen from a predefined size distribution that results in the predicted Sauter mean radius SMR from the energy balance.

2.7.6 The WAVE model

The WAVE model was proposed by Reitz (1987). The model is based on a stability analysis of a cylindrical liquid jet under the influence of perturbations of its surface using a first order linear theory. The liquid and the surrounding gas are assumed incompressible, and the gas is assumed inviscid. The initial disturbances caused by turbulence grow due to aerodynamic forces coming from the relative velocity of the liquid and the gas (Kelvin-Helmholtz instability). The analysis leads to an equation that relates the disturbance growth rate (the increase of the amplitude per time) to its wavelength. Curve fits of the numerical solution of this equation were generated for the growth rate Ω of the fastest growing surface wave and the corresponding surface wavelength Λ.

$$\Omega = \left(\frac{\rho_l r_0^3}{\sigma}\right)^{-0.5} \frac{0.34 + 0.38 \cdot We_g^{1.5}}{(1 + Oh)(1 + 1.4 \cdot T^{0.6})} \tag{2.145}$$

$$\Lambda = 9.02 \cdot r_0 \frac{(1 + 0.45 \cdot Oh^{0.5})(1 + 0.4 \cdot T^{0.7})}{\left(1 + 0.87 \cdot We_g^{1.67}\right)^{0.6}} \tag{2.146}$$

where

$$Oh = \frac{\sqrt{We_l}}{Re_l}, \quad Ta = Oh\sqrt{We_g}, \quad We_g = \frac{\rho_g r_0 u_{rel}^2}{\sigma} \tag{2.147}$$

$$We_l = \frac{\rho_l r_0 u_{rel}^2}{\sigma}, \quad Re_l = \frac{\rho_l r_0 u_{rel}}{\mu_l} \tag{2.148}$$

Oh is the Ohnesorge number, Ta the Taylor number, We_g is the gas Weber number, We_l the liquid Weber number, Re_l the liquid Reynolds number and r_0 is the radius of the undisturbed jet. Reitz (1987) applied this theory to the breakup modeling of the blobs with radius r_0 initialized at the nozzle orifice. New child drops are formed as the surface waves on the parent drop are sheared off by aerodynamic forces. It is assumed that the new child drops get a radius r_{new} proportional to the wavelength Λ

$$r_{new} = C_1 \cdot \Lambda \tag{2.149}$$

The model constant $C_1 = 0.61$ is taken from the original paper of Reitz (1987). The parent drop does not fully disintegrate but only reduces its radius during this breakup process.

$$\frac{dr}{dt} = -\frac{r - r_{new}}{\tau_{bu}} \tag{2.150}$$

where r is the parent droplet radius and τ_{bu} is the breakup time of the model, defined as

$$\tau_{bu} = \frac{3.726 \cdot C_2 \cdot r}{\Lambda \cdot \Omega} \tag{2.151}$$

The model parameter C_2 corrects the characteristic breakup time and depends on the nozzle flow. This parameter needs to be adjusted to match the simulation results with available measurements. A lower value of C_2 leads to a decrease in penetration length, while a higher value of C_2 increases the breakup length by reducing breakup.

2.8   Numerical solution of the Navier-Stokes equations

As mentioned before, the equations of fluid mechanics are analytically solvable only for certain flow types. Often simplifications of the equations are possible, e.g. assuming incompressible flow, but still the resulting equations are difficult to solve. Models are used

to make a solution of the equations possible (e.g. turbulence models). To obtain an approximate solution, a discretization of the differential equations is necessary. The resulting system of algebraic equations can then be solved numerically. An approximation in space and time is necessary, and the numerical solution holds for discrete locations in space and time only. Different discretization methods exist, but in 3D CFD often the Finite-Volume Method is used because it is by definition conservative. The discretization error is mainly determined by the approximation of the fluxes across the surfaces of the control volume.

The mostly used spatial discretization for derivatives on unstructured grids is the 3-point Central Differencing Scheme (CDS). Assuming constant grid size Δx it is defined as

$$\frac{\partial f}{\partial x} = \frac{f_{j+1} - f_{j-1}}{2\Delta x} + O(\Delta x^2) \tag{2.152}$$

$$\frac{\partial^2 f}{\partial x^2} = \frac{f_{j+1} - 2f_j + f_{j-1}}{\Delta x^2} + O(\Delta x^2) \tag{2.153}$$

where $O(\Delta x^2)$ is the order of the discretization error, which is 2 for the given example. Higher-order schemes are usually only used on structured grids, where the neighbor determination is easier.

Time integration schemes are necessary if transient flow is simulated. The solution for the current time step can only rely on the solutions of the previous time steps. This means that the time discretization corresponds to an extrapolation. If only the results of the previous time step are used, the discretization is called explicit. If the discretization also depends on the results of the new time step, the scheme is called implicit. Often implicit schemes are used because they are stable. The order of accuracy is defined by the number of previous time steps used in the discretization scheme. Because of the high memory consumption, often only 1st or 2nd order schemes are used.

For more information on numerical methods in fluid dynamics refer to, e.g., Ferziger & Perić (2008).

3 Turbulent pipe flow simulation

Large Eddy Simulations of turbulent pipe flow for three different bulk velocities have been performed to generate a boundary condition at the nozzle exit for the subsequent LES spray simulations. For the bulk velocity of 100 m/s, a mesh dependency test was performed with 3 different meshes. The results are compared to DNS data from Fukagata & Kasagi (2002) available for nearly the same Reynolds number.

3.1 Simulation setup

An LES simulation resolves most of the turbulent scales. The size of the largest eddies in a turbulent flow is determined by the geometry of the flow itself. For wall bounded shear driven flows, the length scale of the largest eddies l can be estimated as $l \approx 0.1L$ Eggels (1994), where L denotes a length scale of the flow geometry that corresponds to the pipe diameter D in our case. The velocity scale of these largest eddies is of the order of the mean fluctuating velocity and according to Eggels (1994) it can be estimated as $u \approx (0.05 \cdots 0.067)U$, where U is the bulk velocity of the flow. Since the length and time scales are functions of the radius for the given pipe flow, these are only rough estimates of the turbulent scales. The smallest resolved scales are given by the filter width that depends on the grid size. The used top-hat filter results in a filter width of $l_f^3 \approx V_{cell}$. The ratio l/l_f describes the range of length scales of resolved motions and must satisfy the condition $l/l_f > 1$ because otherwise even the largest scales are removed by the filtering. It is suggested by Eggels (1994) that for an LES the condition $l/l_f > 2$ has to be obeyed and that higher values are necessary for a realistic LES. The near wall region, however, needs a further refined mesh to capture the velocity gradients and the damping effects of the wall. If the near wall region is not refined, the SGS model needs to account for these effects.

The temporal resolution for LES also depends on the filter width l_f. The time step Δt should be proportional to the time scale l_f/u. In general, numerical stability limits the time step. For explicit time discretization schemes, the Courant-Friedrichs-Lewy number CFL limits the time step. For one dimension it reads

$$CFL = \frac{U\Delta t}{\Delta x} = \frac{\alpha_u u \Delta t}{\Delta x} < 1 \tag{3.1}$$

where α_u is the ratio of the relevant advection velocity U to the largest eddy velocity scale u. Δt and Δx denote the time step and the mesh size. It follows that

$$\frac{\Delta t}{l_f/u} = \frac{C}{\alpha_u}\frac{\Delta x}{l_f} = \frac{C}{\alpha_u} \ll 1 \tag{3.2}$$

since in our case $\Delta x = l_f$ and $\alpha_u \gg 1$. This means that for explicit time discretization the stability criterion limits the time step Δt and not the time scale l_f/u.
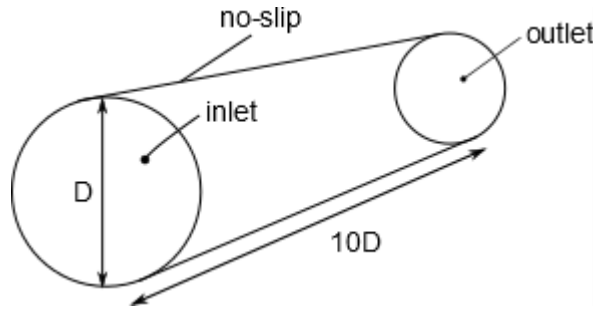
Figure 10: Computational domain

The computational domain for the present pipe flow simulation shown in Figure 10 has a diameter D of 100 μm and length of 1 mm. A periodic inlet/outlet boundary and a wall boundary were applied. The length of the pipe was chosen to be 10 times the diameter to ensure that the largest eddies that can be stretched near the wall will fit in the domain. Eggels (1994) showed for a Reynolds number of 5300 that the two-point correlation coefficient of the streamwise velocity fluctuation is not zero for a separation distance of 2.5 D. This implies that the pipe length should be greater than 5 times the diameter, and that the chosen length of 10 D is sufficient.

The different mesh resolutions that were used for the mesh dependency test are listed in Table 1. A visualization of the three meshes is presented in Figure 11. The mesh M1 was refined near the wall, meshes M2 and M3 not. The mesh dependency tests were performed for a bulk velocity of 100 m/s, which corresponds to a Reynolds number of

5246. The calculation time for all three cases was 0.4 ms. As shown in Figure 13, this is long enough to ensure a fully developed turbulent flow.

	Mesh M1	Mesh M2	Mesh M3
Δx	D/40	D/40	D/20
Δr	D/88	D/42	D/22
Δθ	2π/160	2π/80	2π/40
Number of cells	2176000	512000	68000
Length scale l	D/10	D/10	D/10
$l/$Δx	4	4	2
$l/$Δr	~9	~4	~2
y+ of first cell	~0.5	~3.9	~6.8

Table 1: Mesh properties
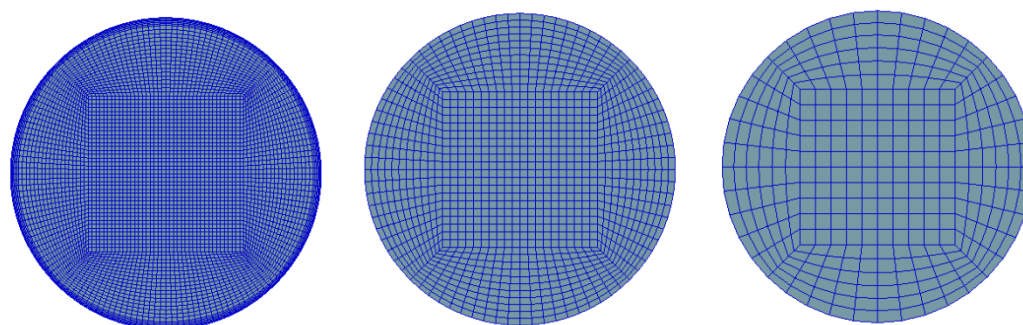
Figure 11: Meshes M1, M2 and M3
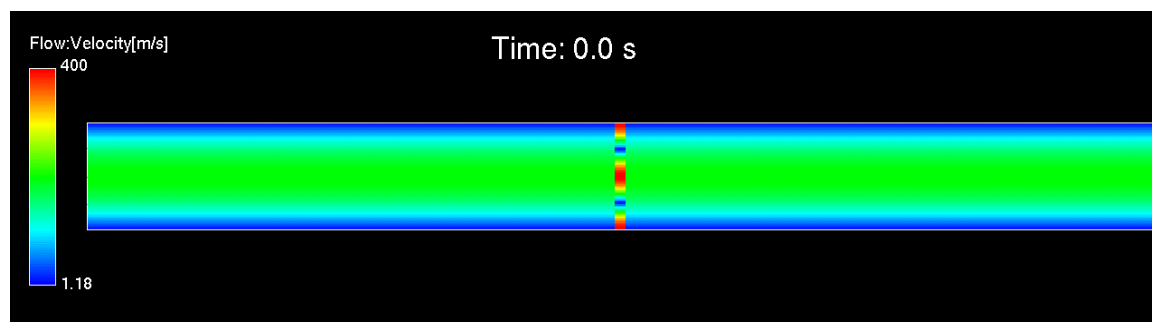
Figure 12: Initial velocity field of case C100

All simulations were initialized with a laminar velocity profile and a disturbance of the velocity field as shown in Figure 12. For some cells in the pipe center, the initial velocity was set to two times the maximum velocity of the laminar velocity field to accelerate the transition to turbulent flow. When the turbulent flow was fully developed, the averaging of the flow quantities was started and the instantaneous flow field was stored to a file for

every time step. These files were later used as boundary conditions for the LES spray simulations. Diesel was used as the fluid, the properties are listed Table 2.

Temperature [K]	Dynamic viscosity [Ns/m²]	Density [kg/m³]
293.15	0.00154	810.521

Table 2: Fluid properties (Diesel)

The simulation cases run to generate the boundary conditions for the spray simulations are listed in Table 3. These simulations were performed using the finest mesh M1 because the results of the mesh dependency test show the best results for this mesh and the subsequent LES spray simulation also has a very fine mesh and therefore the resolution of the stored instantaneous velocity field should approximately match the resolution of the spray mesh.

	Case C050	Case C100	Case C150
Bulk velocity [m/s]	50	100	150
Reynolds number [-]	2623	5246	7870
Calculation time [s]	0.001	0.000445	0.00043
Flow through times [-]	50	44.5	64.5
Time step [s]	2e-8	1e-8	1e-8
Expected centerline velocity [m/s]	63	126	190
CFL number [-]	0.5	0.5	0.76
y+ of first cell	~0.3	~0.5	~0.7

Table 3: Simulation cases

The expected centerline velocity for the fully developed turbulent flow was calculated using the empirical correlation $\overline{U}/u_{max} = 0.791$ for a Reynolds number of 4000 found in Brenn & Meile (2008). The CFL number was calculated using the expected centerline velocity. The timestep was chosen to be small enough to allow even smaller grid sizes in the subsequent spray simulations.

3.2   Simulation results

All LES simulations were performed using the 3D CFD software FIRE v2013.1 from AVL with implicit filtering and the Coherent Structure Model described in chapter 2.5.2 as the SGS

turbulence model. Second-order schemes were used for time and space discretization. Incompressible flow was assumed.

3.2.1   Mesh dependency tests

The results of the mesh dependency tests are compared to DNS data from Fukagata & Kasagi (2002). The averaging of the values was re-started after 100µs when the flow was already fully developed, as shown in Figure 13.
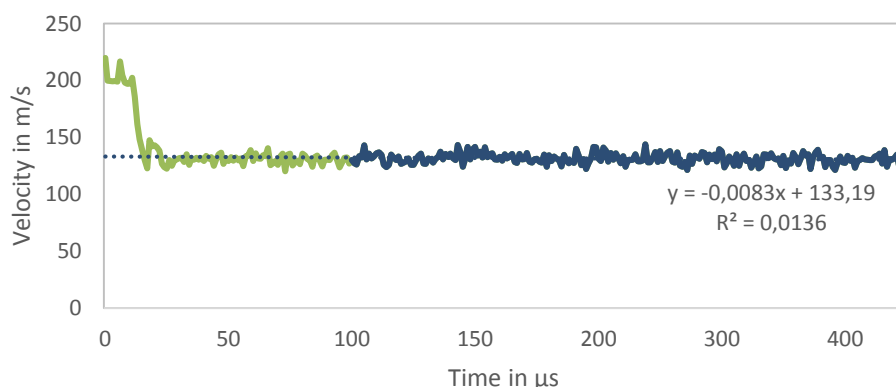
Figure 13: Average velocity on the pipe centerline as a function of time for the mesh M1

The mean non-dimensional velocity profiles for the three meshes are presented in Figure 14 to Figure 16. The results are compared to the DNS data from Fukagata & Kasagi (2002).
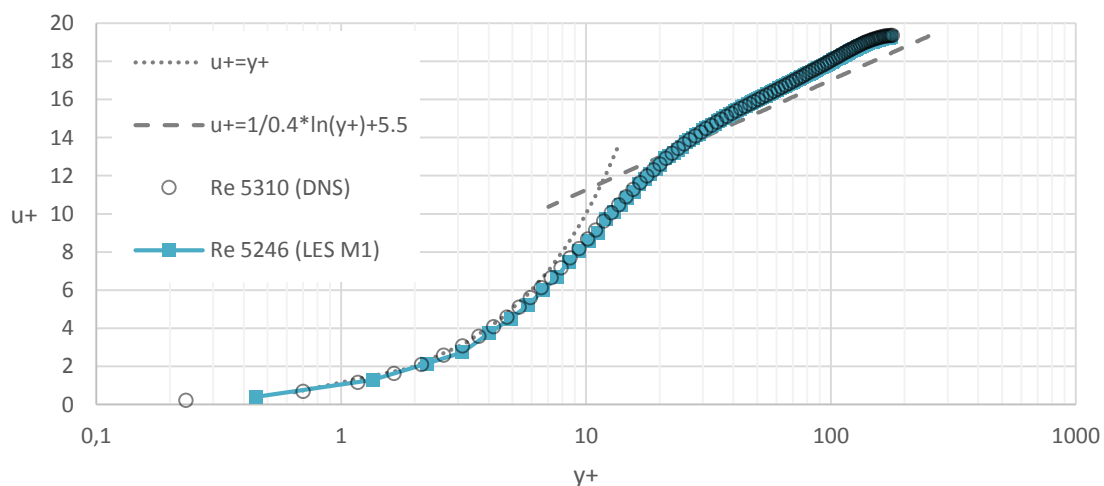
Figure 14: Mean axial velocity normalized by the friction velocity as a function of the dimensionless distance from the wall for mesh M1
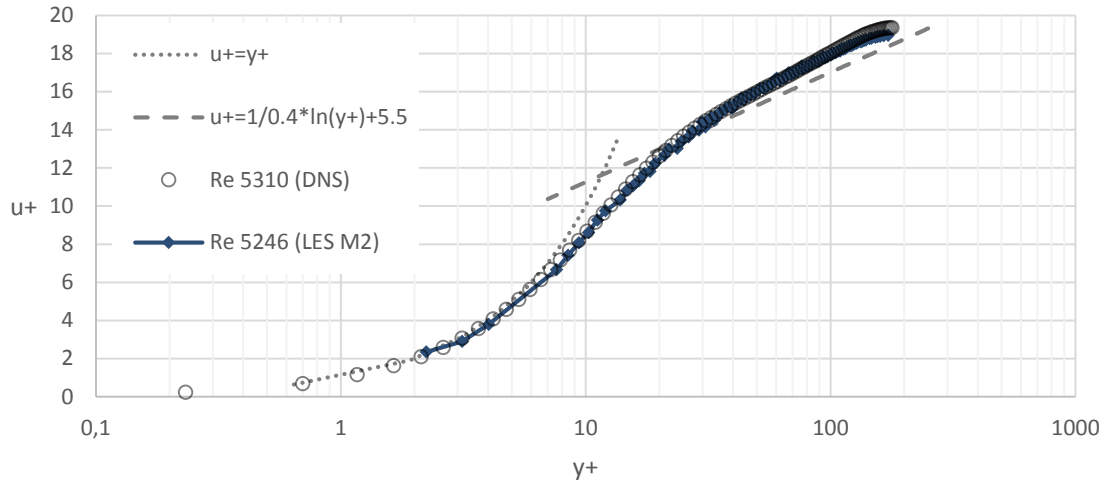
Figure 15: Mean axial velocity normalized by the friction velocity as a function of the dimensionless distance from the wall for mesh M2
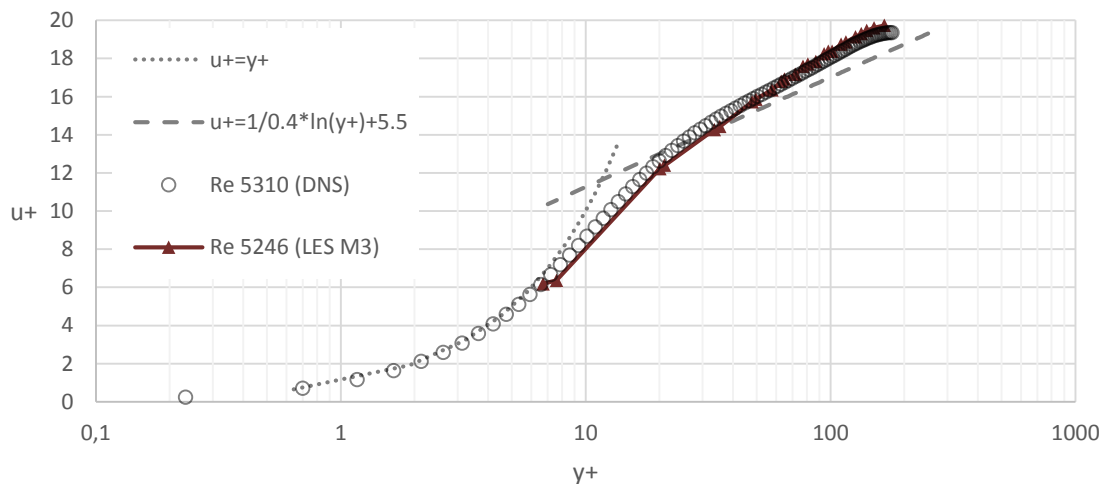
Figure 16: Mean axial velocity normalized by the friction velocity as a function of the dimensionless distance from the wall for mesh M3

The output of FIRE v2013.1 was extended to include the Reynolds stresses in cylindrical coordinates. The average Reynolds stresses and fluctuations in cylindrical coordinates are compared to the DNS data Fukagata & Kasagi (2002) for the three different meshes. The results for the finest mesh M1 are in very good agreement with the DNS data. The results for the mesh M2 are still good, but the mesh M3 seems to be too coarse to capture the Reynolds stresses properly.
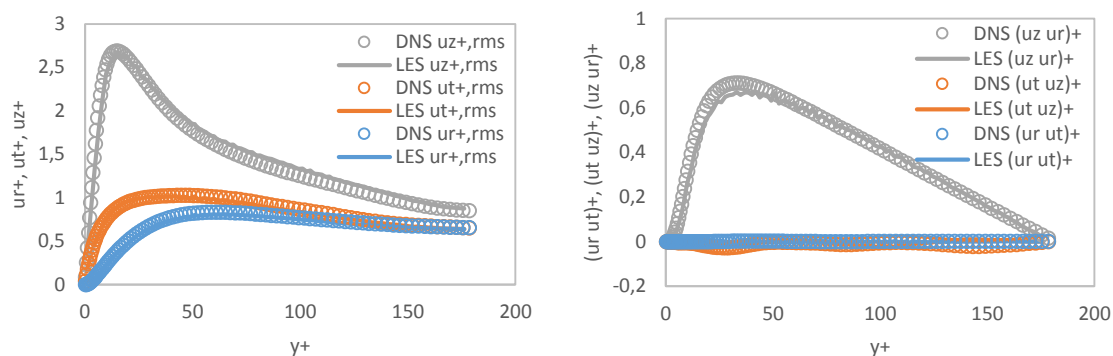
Figure 17: Fluctuations and Reynolds stresses for mesh M1
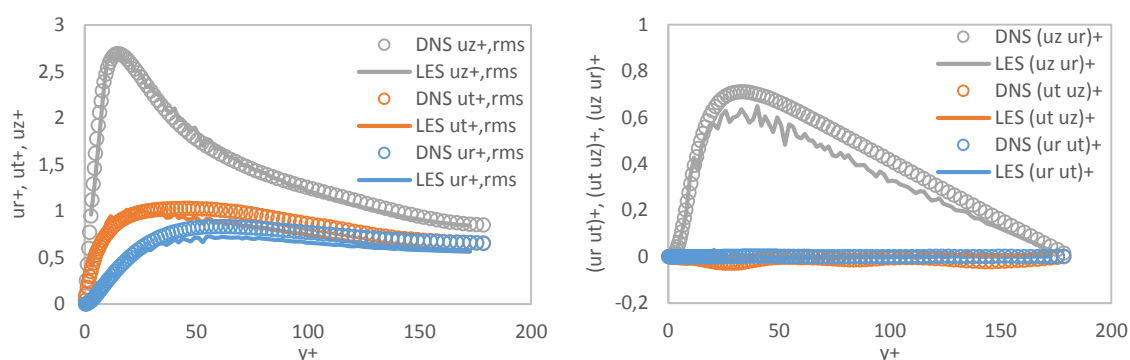
Figure 18: Fluctuations and Reynolds stresses for mesh M2
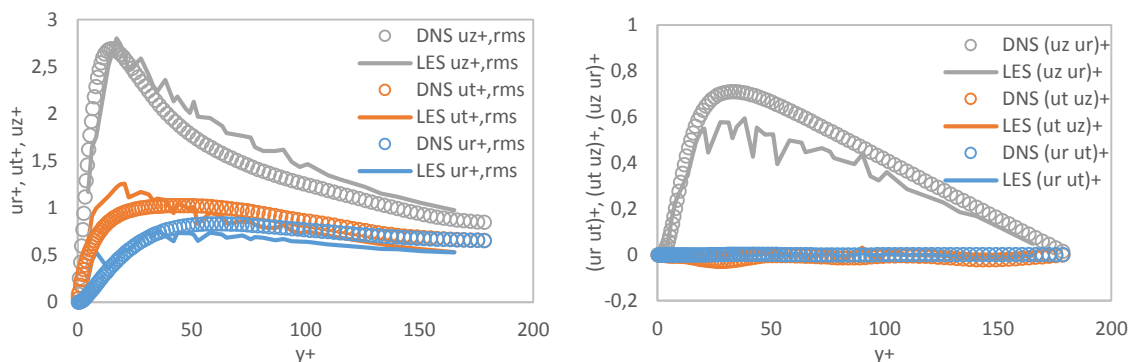
Figure 19: Fluctuations and Reynolds stresses mesh M3

The Reynolds stress tensor τ_{ij} can be expressed in terms of an isotropic τ_{ij}° and an anisotropic tensor τ_{ij}', such that $\tau_{ij} = \tau_{ij}^{\circ} + \tau_{ij}'$. The isotropic part can be written as $\tau_{ij}^{\circ} = (1/3)\tau_{kk}\delta_{ij}$. The anisotropic part then reads $\tau_{ij}' = \tau_{ij} - (1/3)\tau_{kk}\delta_{ij}$. A non-dimensional anisotropy tensor can be defined as

$$b_{ij} = \frac{\tau'_{ij}}{k} = \frac{\tau_{ij}}{k} - \frac{2}{3}\delta_{ij} \qquad (3.3)$$

In the case of isotropic turbulence all terms of the anisotropy tensor b_{ij} vanish. The diagonal elements of b_{ij} are limited to $-1/3 \le b_{ij} \le 2/3$. The anisotropy tensor has a zero trace and the non-zero invariants

$$II = -\frac{1}{2}b_{ij}b_{ji} \quad III = \frac{1}{3}b_{ij}b_{jk}b_{ki} \qquad (3.4)$$

The time mean invariant analysis of Lumley (1978) is a useful tool to characterize the structure of turbulence. The values of these invariants that are realizable in a flow are bounded. This leads to the anisotropy invariant map, or so-called Lumley triangle, presented in Figure 20. The Lumley triangle can also be used to validate measurements, since all realizations of the invariants have to be inside the triangle.
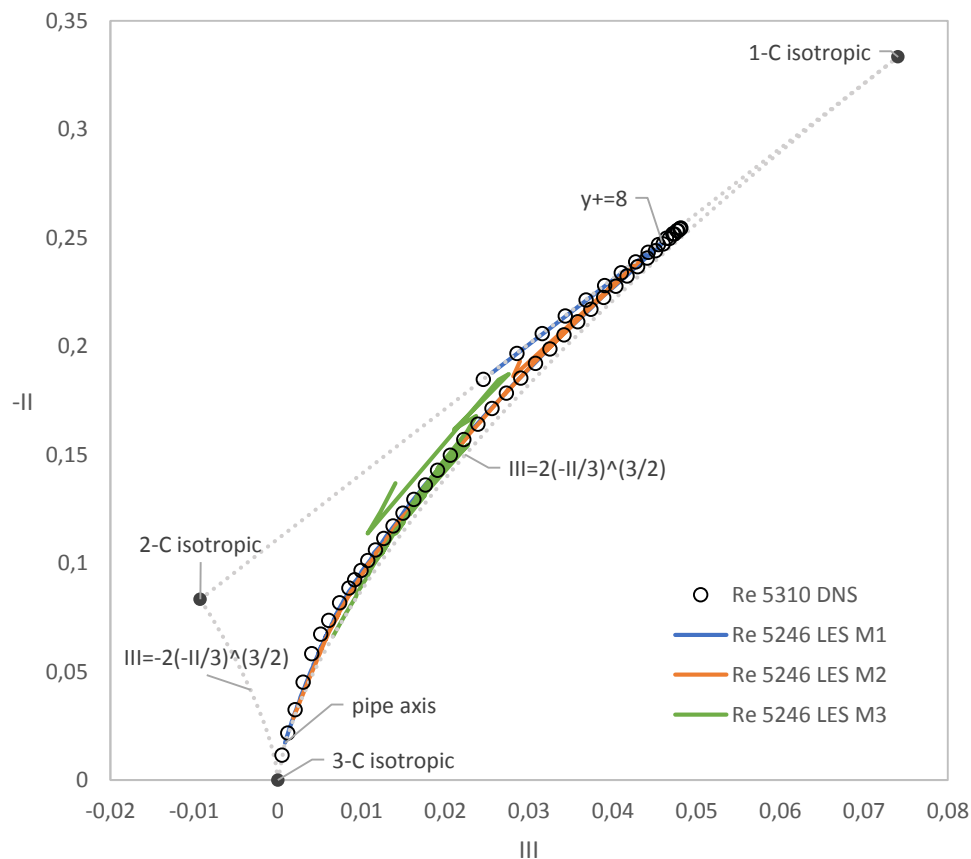
Figure 20: Anisotropy invariant map of the DNS data and the LES results for the three different meshes

The results show that three-component isotropic turbulence only exists near the pipe axis. Near the wall, the turbulence reaches a two-component state due to the damping of the wall-normal component. The results for the mesh M1 show very good agreement with the DNS data. The mesh M2 is not refined near the wall, and the two-component state of turbulence is not reached. The mesh M3 is obviously too coarse to reproduce the DNS results, but all realizations of the invariants are inside the triangle.

The equivalent Smagorinsky constant C_s was calculated from the mean coherent structure model coefficient C_{CSM} and is presented in Figure 21.
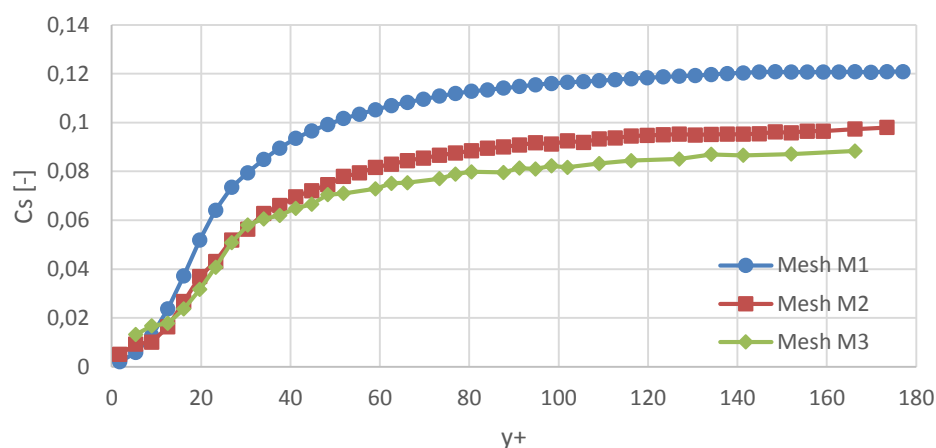
Figure 21: Equivalent Smagorinsky constant C_s as a function of the dimensionless distance from the wall

The results show that the coherent structure model damps its coefficient C_{CSM} near the wall without the need of a special wall function. The value of the coefficient reaches higher values for the finest mesh M1. This is reasonable, since the definition of the eddy viscosity (2.112) includes the filter width Δ that corresponds to the cell size. This leads to the expected higher values of the eddy viscosity for a coarser grid.

The ratio between unresolved and total kinetic energy is also important for LES simulations. It should not be too high, since the idea of LES is to resolve most of the turbulence. The ratios for the three meshes are presented in Figure 22.
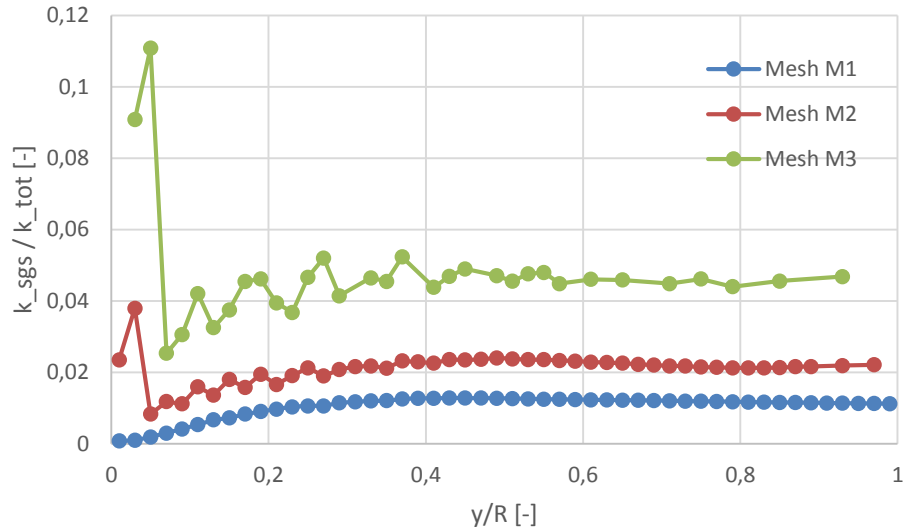
Figure 22: Ratio of unresolved to total kinetic energy as a function of the distance from the wall.

For the meshes M2 and M3, the results show a peak near the wall. The production of turbulent kinetic energy has its maximum in this region, which means that also dissipation is high in this region. For the coarser meshes, more of this dissipation has to be modelled.

3.2.2 Flow generator

The mesh M1 was used to generate the boundary conditions for the subsequent spray simulations. The export of the flow field was started after 200µs for the case C050 and after 100µs for the cases C100 and C150. The mean centerline velocities for the three cases are shown in Figure 23 to Figure 25. The results show, that with increasing Reynolds number, the mean centerline velocity is more stable.
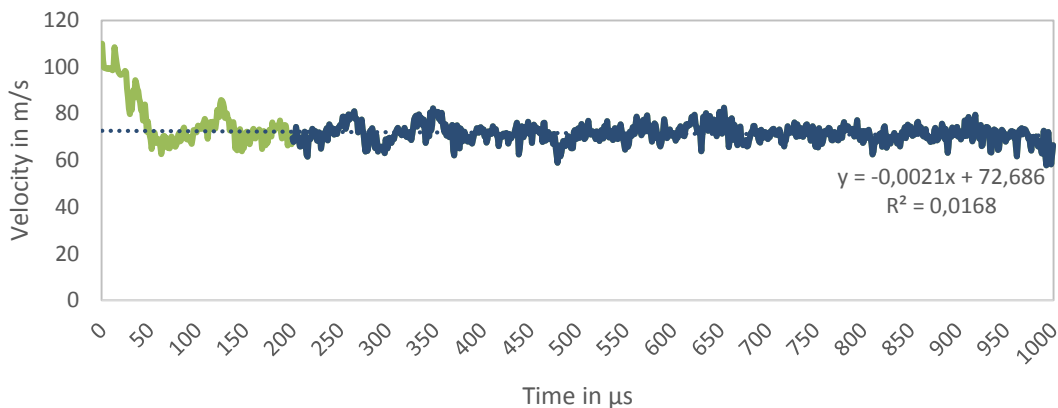
Figure 23: Mean centerline velocity of case C050 as a function of simulated flow time
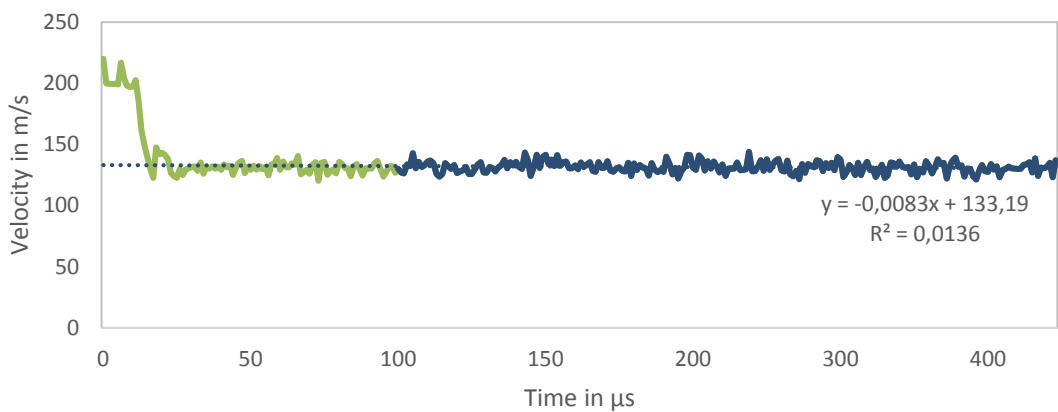
Figure 24: Mean centerline velocity of case C100 as a function of simulated flow time
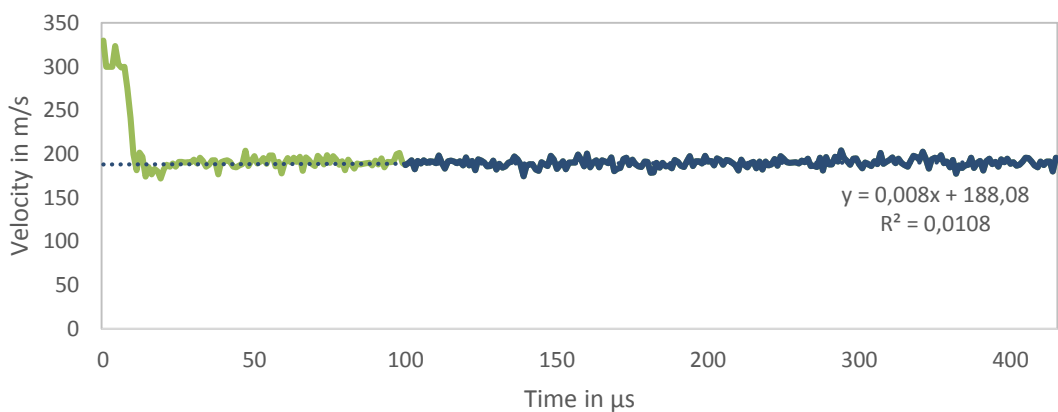
Figure 25: Mean centerline velocity of case C150 as a function of simulated flow time

The downward shift of the velocity profile in the logarithmic region with increasing Reynolds number shown in Figure 26 was also documented by Durst, Kikura, Lekakis, Javanovic, & Ye (1996) for a turbulent channel flow.
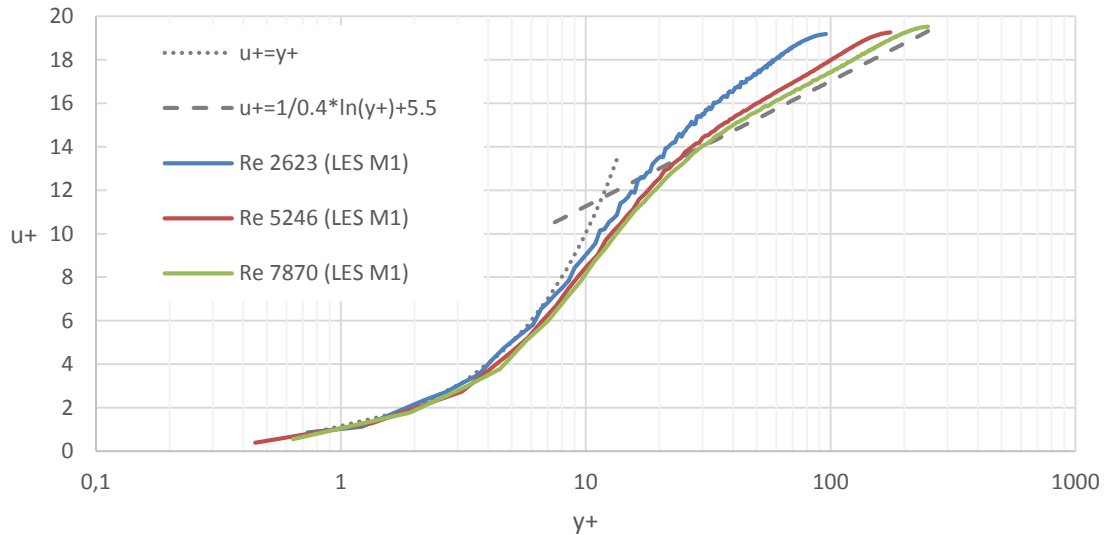
Figure 26: Dimensionless velocity profiles of the three cases

The turbulent velocity fluctuations u' normalized with the friction velocity presented in Figure 27 show a peak at about $y^+ = 12$ and nearly the same curve shape for all three Reynolds numbers. The results are again compared to the DNS data from Fukagata & Kasagi (2002) and show good agreement. The measurements by Durst, Kikura, Lekakis, Javanovic, & Ye (1996) show similar results for the investigated Reynolds number range.
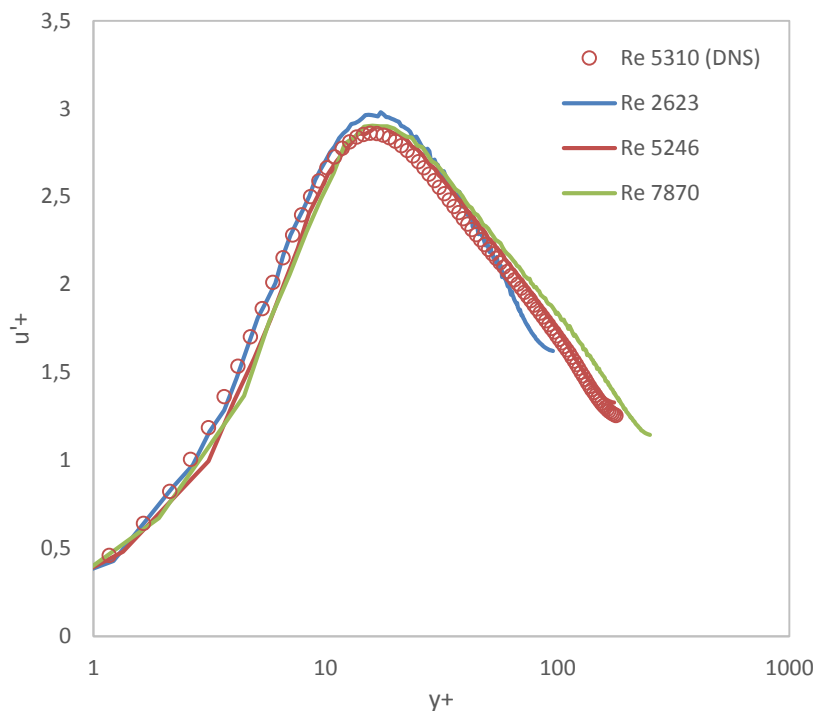
Figure 27: Distribution of turbulent velocity fluctuations u' normalized with the friction velocity

The fully developed turbulent flow for the three different bulk velocities are shown in Figure 28 to Figure 30. It can be seen that the turbulent structures become smaller with increasing Reynolds number.
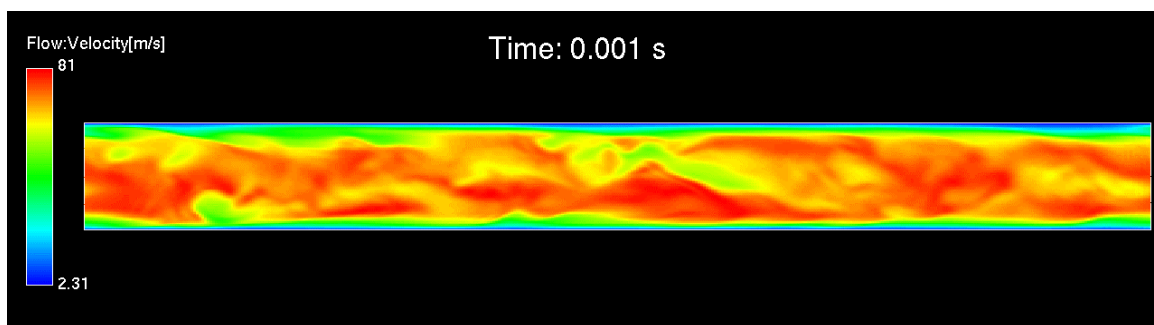
Figure 28: Fully developed turbulent pipe flow for a bulk velocity of 50 m/s (Re = 2623) – spatial distribution of the velocity magnitude
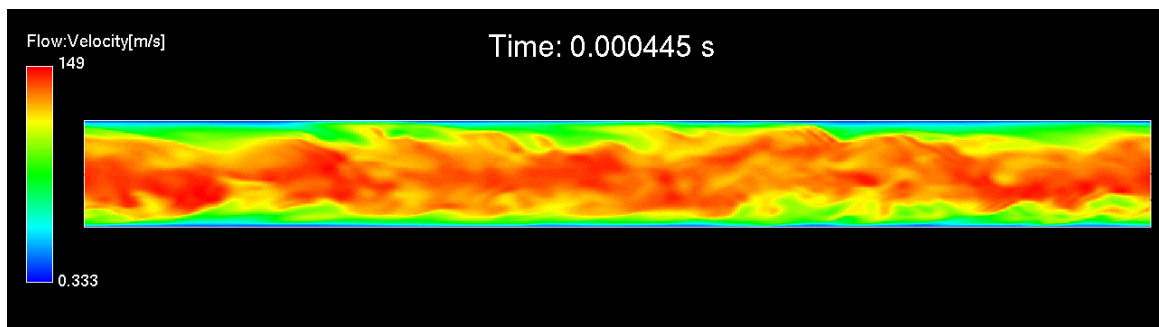
Figure 29: Fully developed turbulent pipe flow for a bulk velocity of 100 m/s (Re = 5246) – spatial distribution of the velocity magnitude
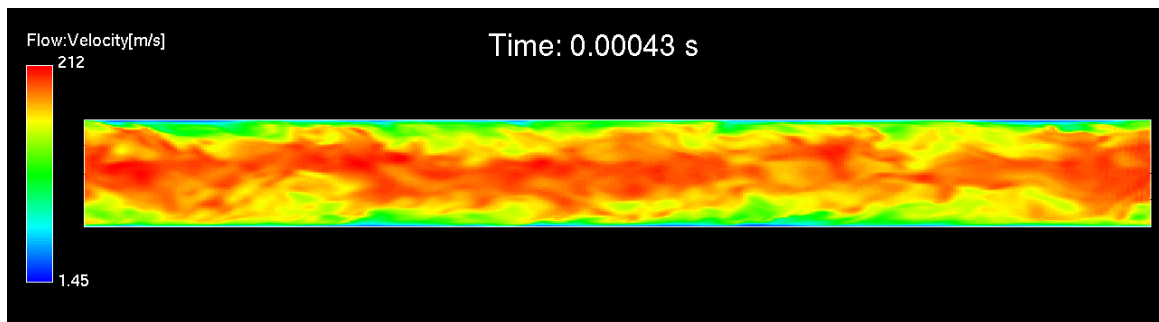
Figure 30: Fully developed turbulent pipe flow for a bulk velocity of 150 m/s (Re = 7870) – spatial distribution of the velocity magnitude

3.3 Conclusions

- The mesh dependency tests showed that the CSM is able to generate excellent results for the finest mesh M1 and good results for the coarser mesh M2. With the coarsest mesh M3, the velocity profile was captured properly, but the Reynolds stresses were not in a good agreement to DNS data. The calculation of the mean equivalent Smagorinsky constant from the mean CSM coefficient showed that the damping effects of the wall are well captured by this model without the need for a special wall damping function. The value for the equivalent Smagorinsky constant on the pipe axis differed from the constant value of 0.1 used in the implementation of the Smagorinsky model in FIRE for the finest and the coarsest mesh. This implies that a fixed value of the coefficient is difficult to define and that a local evaluation is necessary. Since the distance from the wall, which is often hard to determine in complex flows, is not needed for the determination of the

CSM model parameter, and the value range of the parameter is quite narrow, it should also be applicable to complex geometries.

- For the case C050 with a Reynolds number of 2623, which is not far from the critical Reynolds number of approximately 2300 it can be seen that the mean velocity on the centerline is not as stable in time as for higher Reynolds numbers. The variance of the mean velocity on the centerline decreases with increasing Reynolds number.

- LES simulations need a fine mesh to produce results close to DNS results. Only the smallest scales of turbulence can be assumed isotropic, and modelling them with a Boussinesq approach like the Smagorinsky and Coherent Structure Model is appropriate. If the mesh gets too coarse, the anisotropy of turbulence cannot be accounted for by the models.

4 LES/VOF simulation of turbulent liquid jets

LES simulations of turbulent liquid jets with a diameter of 100 μm have been performed to gain information on the development of the liquid core. The bulk velocities of the jet ranged from 50 to 150 m/s and the used liquid was Diesel fuel. The liquid jet was injected into quiescent air at three different densities, relevant to Diesel injection in ICE, ranging from 15 to 34.5 kg/m³. A so-called cold spray, without heat transfer and vaporization, was simulated. The velocities were chosen to represent the velocities during the opening and closing phases of a Diesel injector needle.

In experiments, several disturbances of the liquid jet exist at the same time. In numerical experiments, an ideal flow setting is possible. The flow field of the liquid jet was initialized with the results of the turbulent pipe flow simulation from chapter 3. Effects of cavitation or fuel supply oscillations were not considered though they can have a significant influence on the breakup of a liquid jet, as discussed by Dumouchel (2008). This means that only the influences of turbulence and aerodynamic effects on the primary breakup are investigated.

The requirement for grid resolution for simulating the atomization of a liquid jet is severe. If the grid resolution is not high enough, artificial breakup may occur when the thickness of a liquid structure becomes smaller than the grid spacing. Surface forces induce breakup and must therefore be evaluated correctly. This means that the curvature of the liquid surface needs to be calculated, which is only possible if the grid spacing is much smaller than the radius of the liquid structure. High mesh resolution, especially close to the phase interface as discussed by Herrmann (2011), would be necessary. Since droplets of O(1 μm) are produced during breakup of a liquid Diesel jet, the needed grid resolution often exceeds the feasible limits. Based on the available computational resources, the simulations of this thesis focus on the determination of the liquid core length. Droplet size distributions were not analyzed. The applied interface tracking is a hybrid method combining the Eulerian multi-fluid and the VOF approaches, as discussed by Han & Alajbegovic (2002). The benefit of this method is that it applies VOF where the mesh resolution is fine enough, while it solves the Euler-Eulerian multiphase transport equations (2.121) and (2.123) where the mesh resolution is too coarse. Having this in

mind, the presented simulations show a practical workflow to capture the liquid core and the larger ligaments produced near the nozzle orifice.

4.1 Simulation setup

The computational domain shown in Figure 31 was used for the spray simulations and had a size of 12D x 12D x 46D, where D=100µm is the nozzle diameter. A static pressure boundary condition was applied to all borders of the domain, except for the border at the nozzle orifice. A wall boundary condition was applied there. The large width and height of the domain were necessary to allow for the use of a static pressure boundary condition. Since a very fine mesh resolution is needed in the spray formation area, but not near the boundary, the mesh was refined towards the spray axis in 4 steps, shown in Figure 32. Cubic mesh cells are used, and the refinement was done by dividing a parent cell into 8 new cubic cells.
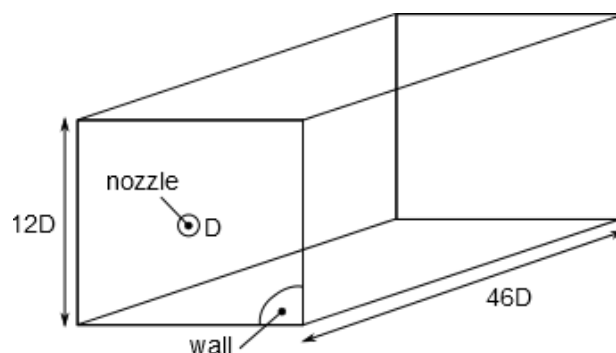
Figure 31: Computational domain size of meshes MS1, MS2 and MS3
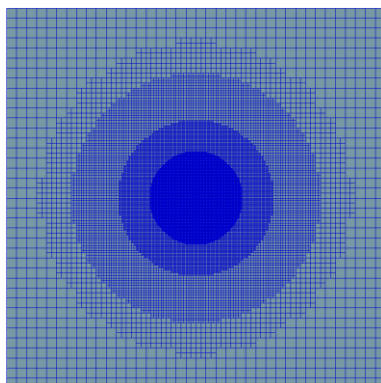
Figure 32: Refinement of meshes MS1, MS2 and MS3 in radial direction

A mesh dependency test was performed using three different mesh sizes near the spray axis. The exact properties of the meshes are listed in Table 4.

	Mesh MS1	Mesh MS2	Mesh MS3
Cell size [μm]	2.5	2	1.6
Total number of cells [millions]	22	42	83

Table 4: Mesh properties

In other numerical experiments, e.g. Ménard, Tanguy, & Berlemont (2007), a slip-wall boundary condition is used for the 4 borders surrounding the spray axis, and the distance from the nozzle is often only 1-2 nozzle diameters. A test with such a small domain shown in Figure 33 was performed, and the results were compared to the results with the larger domain used for all other simulations in this thesis. This small domain also consists of cubic cells with an edge length of 2.5 μm and has no refinement. The small domain will be referred to as mesh MS4.
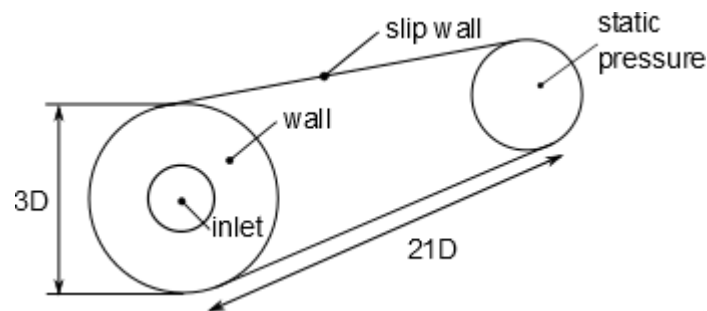
Figure 33: Small computational domain MS4

Nine cases were simulated with different gas densities and mean injection velocities. The inflow boundary conditions for the liquid velocity field were created by a pipe flow simulation as described in chapter 3. The operating conditions and phase properties of the simulation cases will be outlined later in the results chapter. The liquid phase has the same properties as the liquid used in the pipe flow simulations and corresponds to Diesel fuel properties. The gas phase is air and is treated as incompressible, which is reasonable because the Mach number under Diesel injection conditions with high gas temperatures will be low.

4.2 Simulation results

All two-phase LES simulations were performed with the 3D CFD software FIRE v2013.1 from AVL. The VOF model described in chapter 2.6.2 was used to track the surface between the two phases. The Smagorinsky model was used as the SGS turbulence model. Second-order schemes were used for the discretization.

4.2.1 Influence of boundary conditions

It was assumed that the slip wall boundary condition has an influence on the spray formation. Therefore the goal was to replace it by a static pressure boundary condition. This is only reasonable with a greater diameter of the computational domain. Therefore, several test simulations were performed until the final domain size of 12D x 12D x 46D shown in Figure 31 was chosen. The same simulation was also run on a small domain with a diameter of three nozzle diameters as shown in Figure 33. The phase properties for these two simulations where the same as used by Ménard, Tanguy, & Berlemont (2007) and are outlined in Table 5. The meshes MS1 and MS4 were used for comparison with a mean injection velocity of 100 m/s. The inflow boundary condition was generated by an LES pipe flow simulation.

Phase	Viscosity [Ns/m²]	Density [kg/m³]	Surface tension [N/m]
Liquid	1.2E-03	696	0.06
Gas	1.0E-05	25	

Table 5: Phase properties

The liquid volume fraction distributions of the two simulations after a simulation flow time of 30μs are presented in Figure 34 and Figure 35. It can be seen in Figure 34 that near the slip wall a reasonable amount of liquid is present, and that the volume fraction is much more smeared further away from the nozzle orifice than in the case with the larger domain shown in Figure 35. Let $\bar{\varphi}$ denote the mean liquid volume fraction within the nozzle diameter D defined as

$$\bar{\varphi} = \frac{2\pi \cdot 4}{D^2 \pi} \int_{r=0}^{\frac{D}{2}} \varphi(r) r dr \qquad (4.1)$$

Figure 36 shows a considerable difference for the mean liquid volume fraction within the nozzle diameter $\bar{\varphi}$ starting at about 10 nozzle diameters from the nozzle orifice. The main reason for this behavior comes from the fact that air is entrained from the lateral boundaries in the simulation case with mesh MS1. The mesh MS4 does not allow this due to the slip-wall boundary condition.
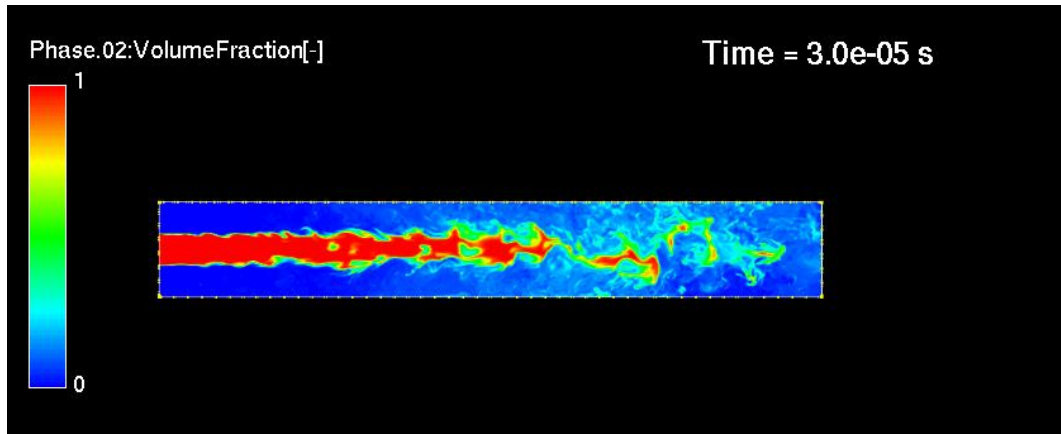
Figure 34: Liquid volume fraction distribution for a mean injection velocity of 100 m/s after 30µs of simulated flow time using mesh MS4
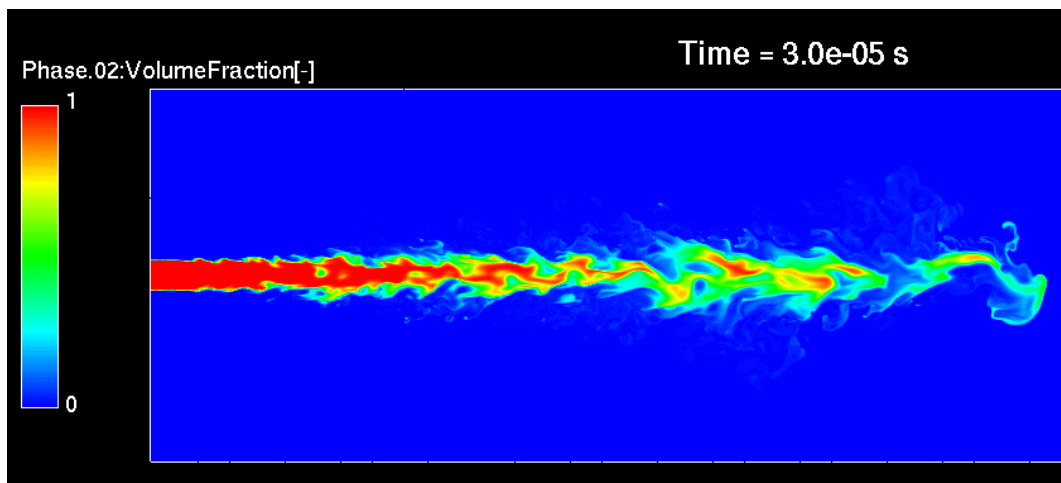
Figure 35: Liquid volume fraction distribution for a mean injection velocity of 100 m/s after 30µs of simulated flow time using mesh MS1
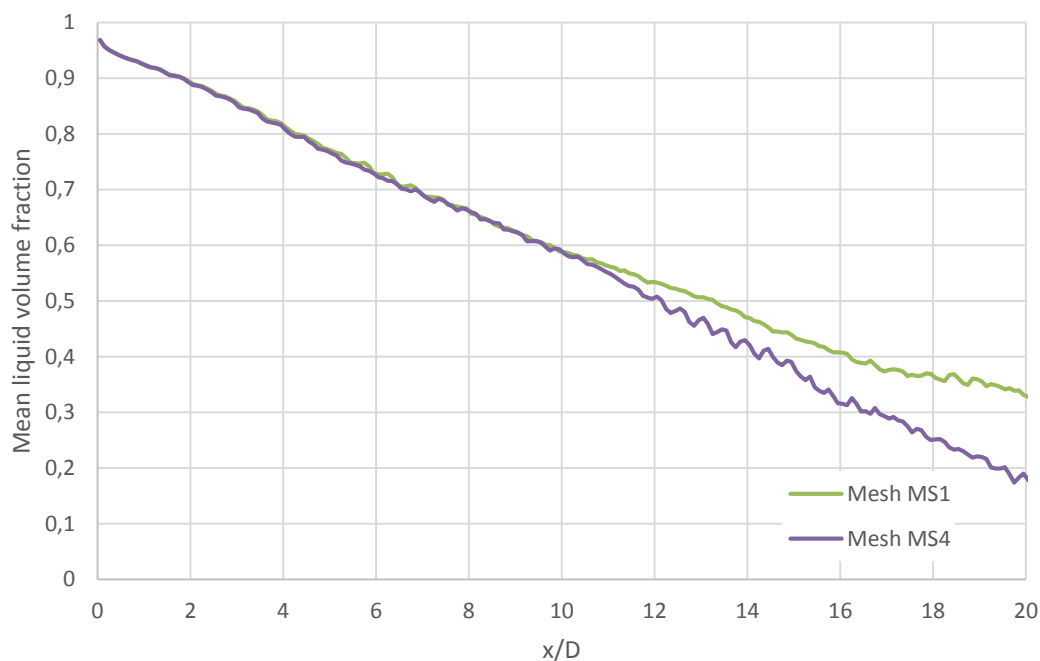
Figure 36: Mean liquid volume fraction within the nozzle diameter $\bar{\varphi}$ as a function of the distance from the nozzle normalized by the nozzle diameter

4.2.2   Mesh dependency tests

A mesh dependency test was performed with the three meshes MS1, MS2 and MS3. The phase properties listed in Table 5 are used for the simulations and the inflow boundary condition is again generated by a fully developed turbulent pipe flow simulation with a bulk velocity of 100 m/s. The mean liquid volume fractions within the nozzle diameter $\bar{\varphi}$ for the three meshes are presented in Figure 37. The curves for the meshes MS2 and MS3 are nearly the same, while the curve for the coarsest mesh MS1 differs slightly, starting at a distance of 15 nozzle diameters from the orifice.

Since the goal of the LES spray simulations is the determination of the liquid core length, we need to define what is the liquid core. Here the liquid core is defined as the region where the mean liquid volume fraction is greater than 0.5. This definition of the liquid core was also used by Heidorn & Steiner (2009). The value of the volume fraction is averaged in the circumferential direction and also over time, where the time averaging is started when the liquid volume fraction is greater than 0 for the first time. The resulting

images of the liquid core for all three meshes are shown in Figure 38 to Figure 40. The calculated liquid core length is nearly identical for the meshes MS2 and MS3, but shorter for the coarsest mesh MS1.
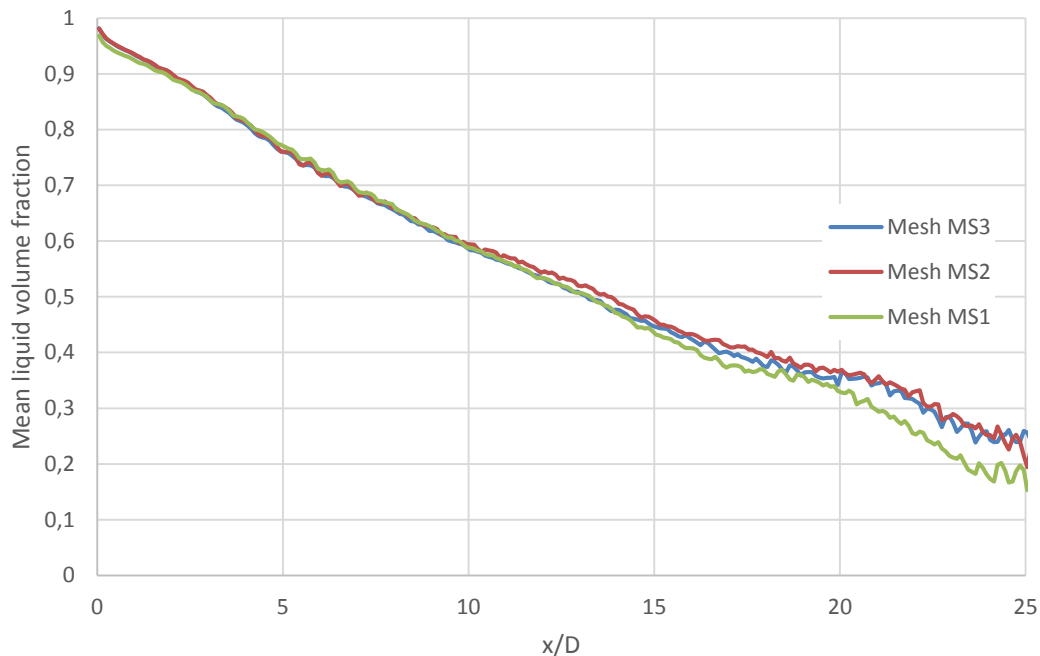
Figure 37: Mean liquid volume fraction within the nozzle diameter $\bar{\varphi}$ as a function of the distance from the nozzle normalized by the nozzle diameter
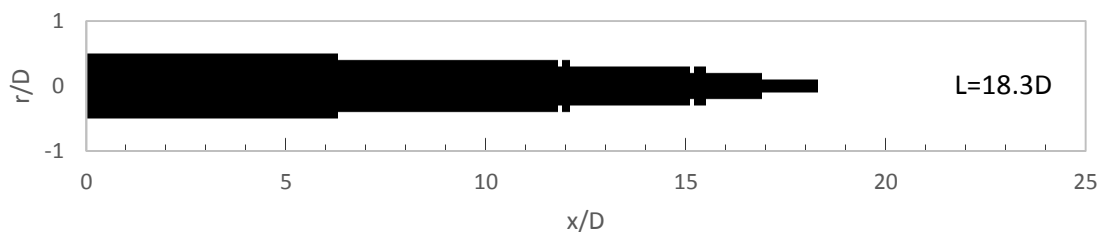
Figure 38: Liquid core visualization for mesh MS1
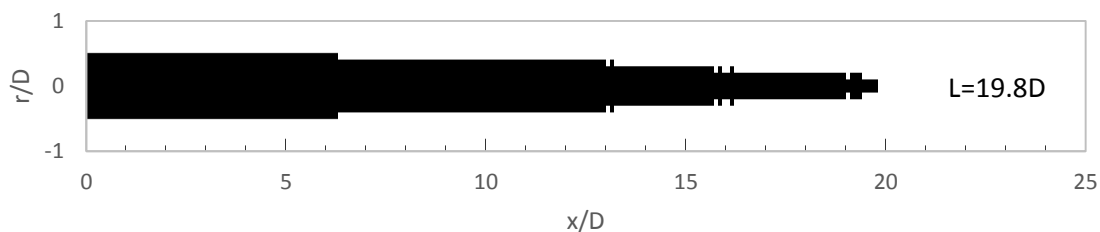
Figure 39: Liquid core visualization for mesh MS2
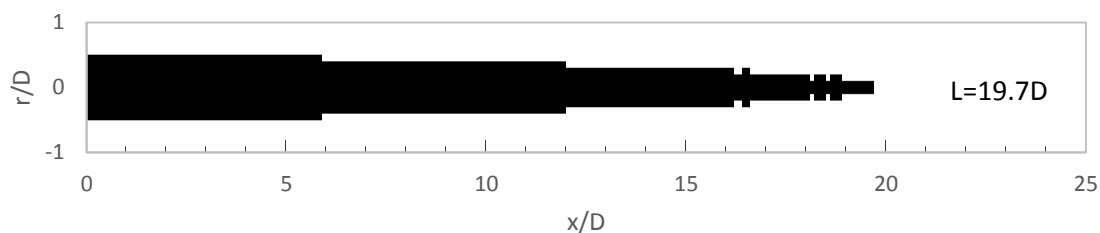
Figure 40: Liquid core visualization for mesh MS3

4.2.3 Liquid core length under different gas pressures and injection velocities

The development of the liquid core length under different ambient gas pressures and injection velocities is investigated. Because the computational costs of these simulations is severe and mesh MS2 showed similar results as the finest mesh MS3, all further simulations were carried out on the mesh MS2. The liquid and gas properties and injection conditions are listed in Table 6 and Table 7, respectively. The results of the fully developed turbulent pipe flow simulations described in chapter 3.2.2 are used as an inflow boundary condition. The diameter of the nozzle orifice is 100µm.

Phase	Viscosity [Ns/m²]	Density [kg/m³]	Surface tension [N/m]
Liquid	1.54E-03	810.521	0.0264
Gas	3.90E-05	15, 25, 34.5	

Table 6: Phase properties

Mean injection velocity [m/s]	Injection Reynolds number [-]	Liquid Weber number [-]	Gas density [kg/m³]	Gas Weber number [-]	Time step [s]
50	2623	7659	15	142	2E-08
50	2623	7659	25	236	2E-08
50	2623	7659	34.5	326	2E-08
100	5246	30634	15	567	1E-08
100	5246	30634	25	945	1E-08
100	5246	30634	34.5	1304	1E-08
150	7870	68928	15	1276	1E-08
150	7870	68928	25	2126	1E-08
150	7870	68928	34.5	2934	1E-08

Table 7: Operating conditions

According to Reitz (1978) the mechanism of jet breakup is defined by its Ohnesorge and Reynolds numbers. Since the liquid properties and the jet diameter are the same for all simulations, the Ohnesorge number is constant at the value $Oh = 0.0334$. By adding the operation points listed in Table 7 to the Ohnesorge nomogram shown in Figure 41 it turns out that two of the three operation points lie in the second wind induced regime and one in the atomization regime.

Since the nomogram does not account for the gas pressure, Hobbie & Eggers (2004) suggested to replace the Ohnesorge number in the nomogram by the following dimensionless number

$$Z = Oh\sqrt{\frac{\mu_l}{\mu_g}We_g} = \sqrt{\frac{\mu_l^3}{\mu_g}\frac{u^2}{\sigma^2}\frac{\rho_g}{\rho_l}} \qquad (4.2)$$

where μ_l and μ_g are the liquid and gas dynamic viscosities, We_g is the gas Weber number, u is the velocity, σ the surface tension and ρ_g and ρ_l are the gas and liquid densities, respectively. Adding the operating points to the new nomogram shows that they should all lie in the atomization regime. The operating points for a gas density of 34.5 kg/m³ are shown in Figure 42. The lines mark the border between the second wind induced and atomization regimes for each injection velocity.
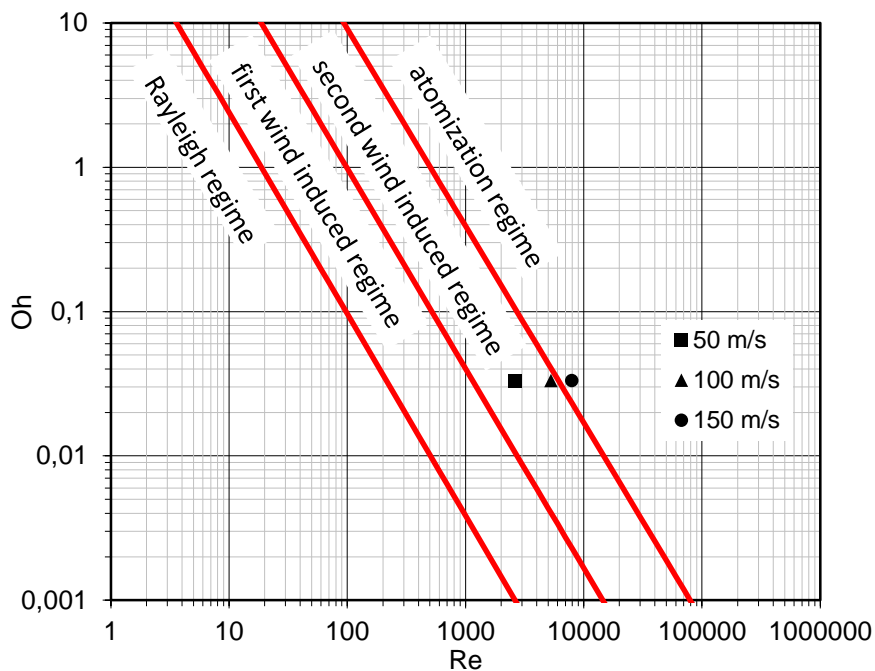
Figure 41: Ohnesorge nomogram containing the three operation points of the simulations
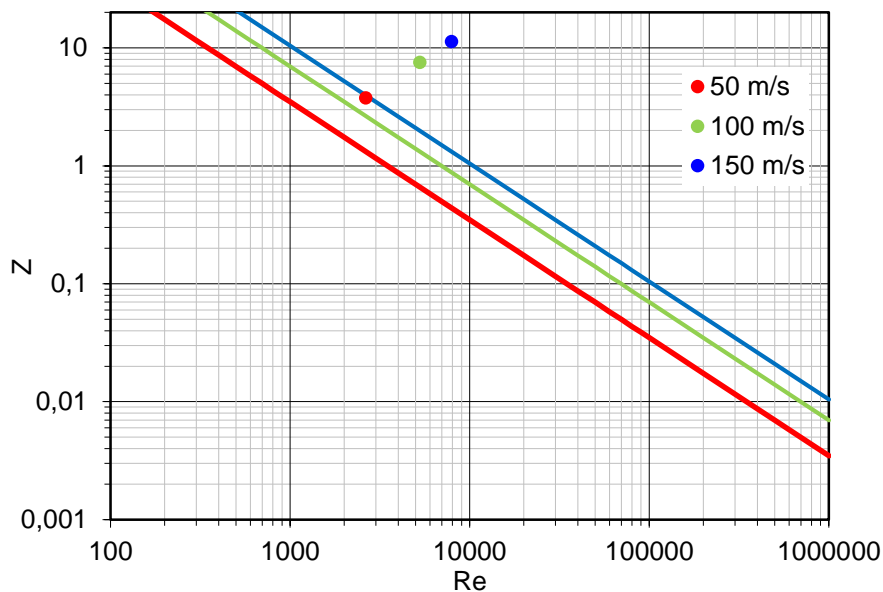
Figure 42: Nomogram according to Hobbie & Eggers (2004) for a gas density of 34.5 kg/m³. The lines mark the border between the second wind induced and atomization regimes for each injection velocity.

The liquid core length was calculated from the simulation results for all 9 operating conditions after the spray tip reached a position of 4.5 mm from the nozzle orifice. The

liquid core is defined as the region where the mean liquid volume fraction is greater than 0.5. The value of the volume fraction is averaged in the circumferential direction and also over time, where the time averaging is started when the liquid volume fraction is greater than 0 for the first time. The resulting liquid core lengths are presented in Figure 43.
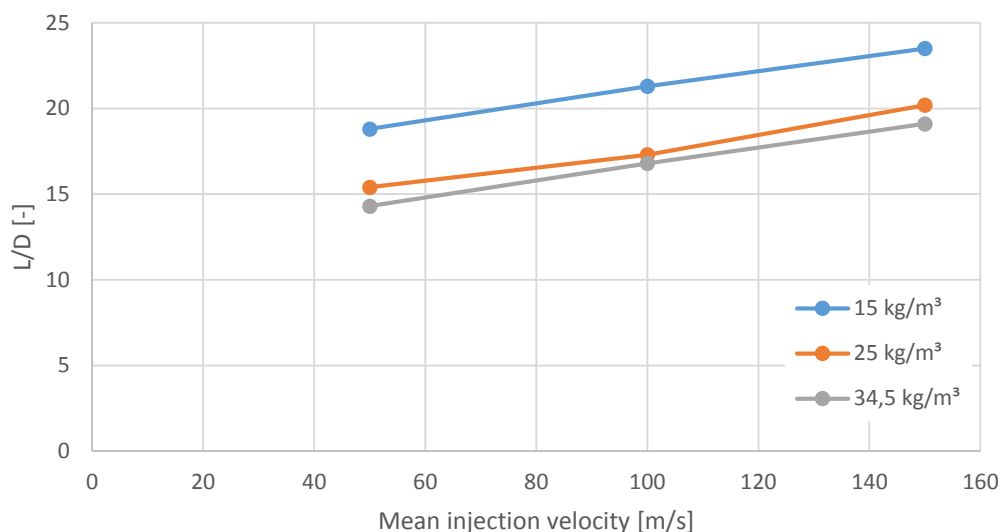
Figure 43: Liquid core length calculated from simulation results normalized by the nozzle diameter as a function of the mean injection velocity. The lines correspond to the different gas densities.

The curves show that, for a given injection velocity, the liquid core length decreases with increasing gas density. The effect of the ambient gas density on the liquid core length is much stronger in the range of 15 to 25 kg/m³ than for the range 25 to 34.5 kg/m³. This effect was also observed by Hiroyasu, Shimizu, & Arai (1982) and Arai, Shimizu, & Hiroyasu (1985), who investigated the influence of ambient pressure on liquid jet breakup length.

There seems to be a nearly linear correlation between the liquid core length and the mean injection velocity in the investigated region that does not depend on the gas density. All operation points definitely lie in the turbulent region of the stability curve shown in Figure 8. The observed increase of the liquid core length with the injection velocity corresponds to the stability curve, and authors like Arai, Shimizu, & Hiroyasu (1985) published measurement results in the same Reynolds number range that also showed this trend.

The iso surfaces representing a liquid volume fraction of 0.1 for all operation conditions at nearly the same spray tip penetration are shown in Figure 44 to Figure 46.

$$\rho_g = 15 \frac{kg}{m^3}$$

$$\rho_g = 25 \frac{kg}{m^3}$$

$$\rho_g = 34.5 \frac{kg}{m^3}$$
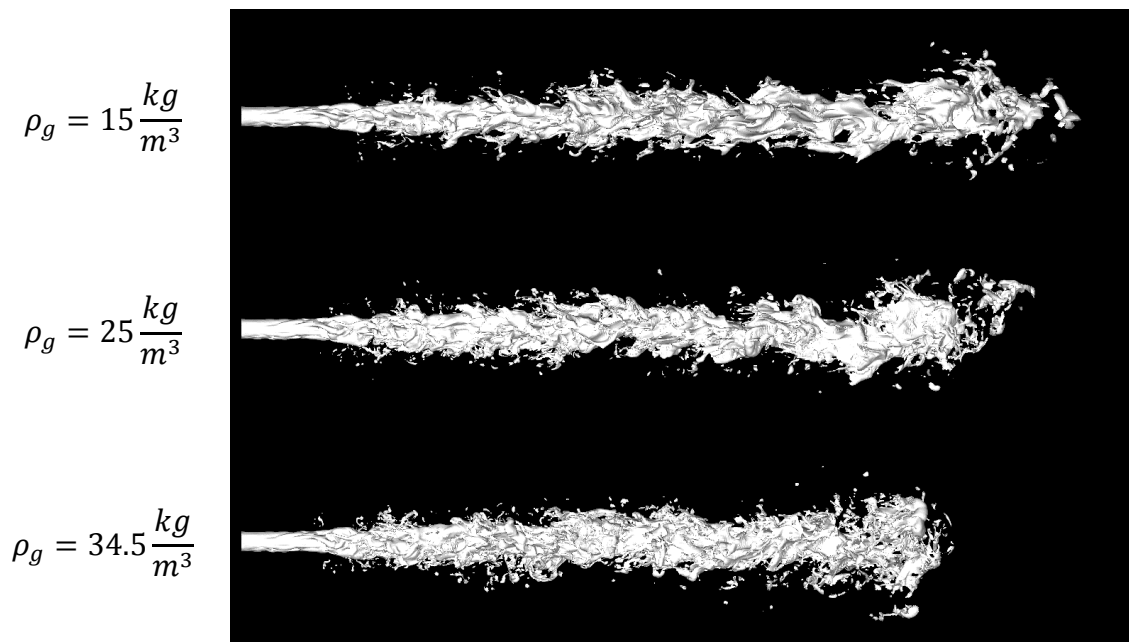
Figure 44: Spray formation for 50 m/s mean injection velocity and different gas densities after 90 µs. The iso surface represents a liquid volume fraction of 0.1

$$\rho_g = 15 \frac{kg}{m^3}$$

$$\rho_g = 25 \frac{kg}{m^3}$$

$$\rho_g = 34.5 \frac{kg}{m^3}$$
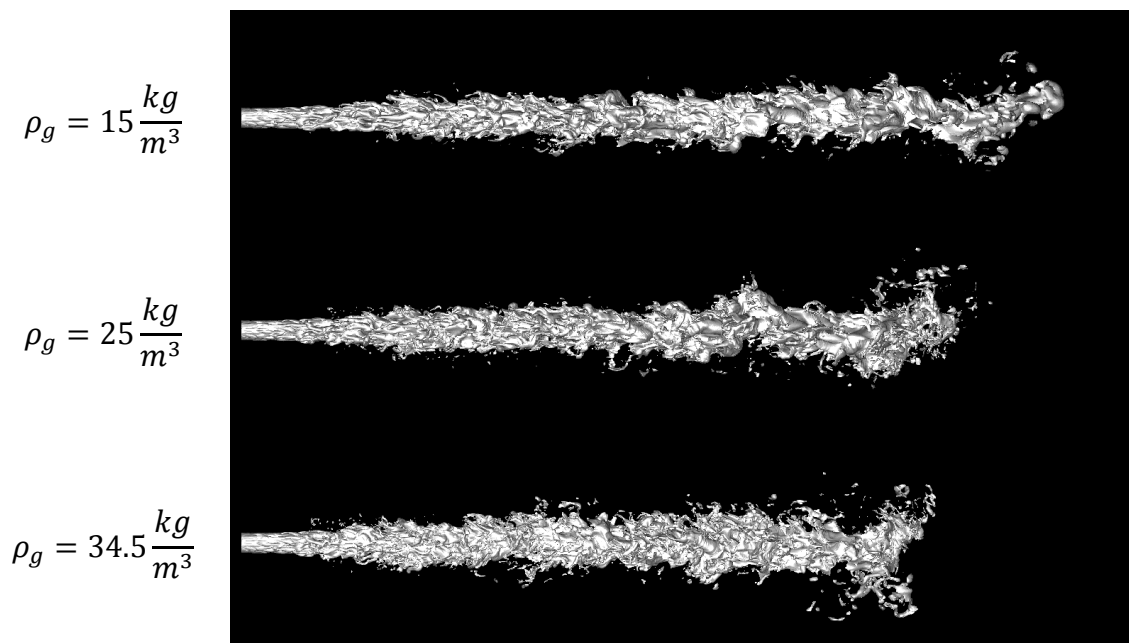
Figure 45: Spray formation for 100 m/s mean injection velocity and different gas densities after 45 µs. The iso surface represents a liquid volume fraction of 0.1

$$\rho_g = 15\,\frac{kg}{m^3}$$

$$\rho_g = 25\,\frac{kg}{m^3}$$

$$\rho_g = 34.5\,\frac{kg}{m^3}$$
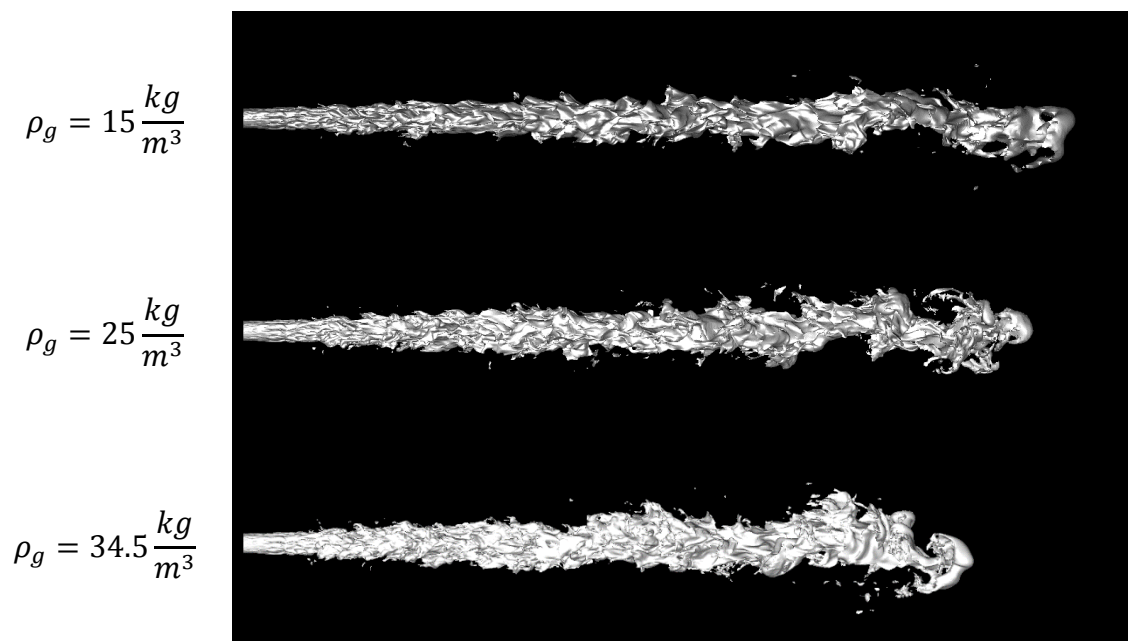
Figure 46: Spray formation for 150 m/s mean injection velocity and different gas densities after 30 µs. The iso surface represents a liquid volume fraction of 0.1
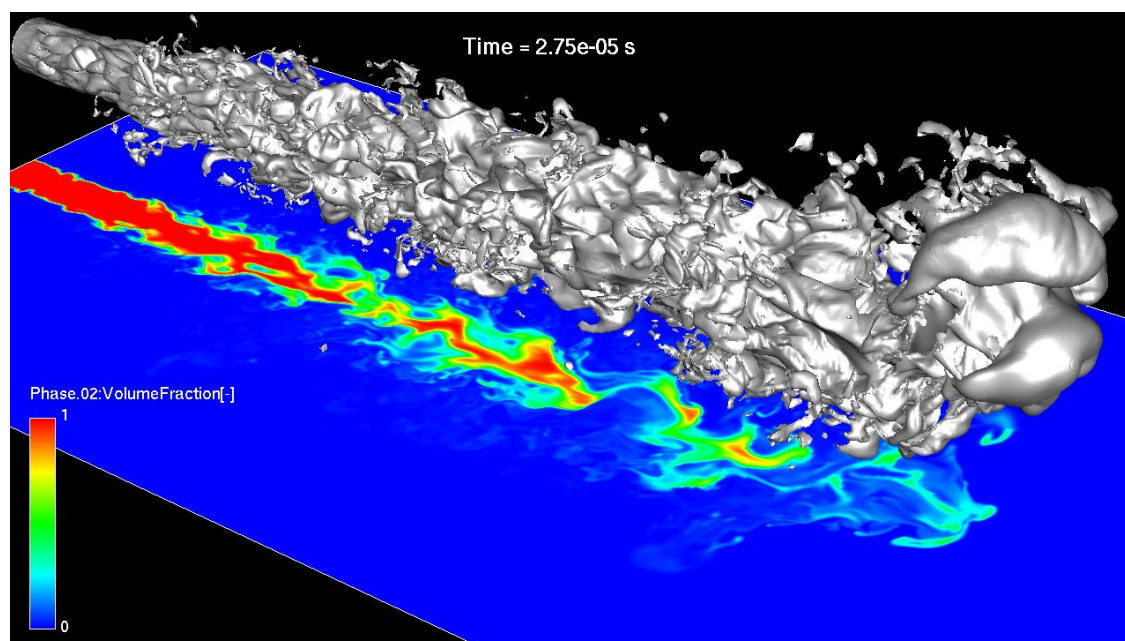
Figure 47: Spray formation for 100 m/s mean injection velocity and a gas density of 34.5 kg/m³. The iso surface represents a liquid volume fraction of 0.1

Looking at the visualization of the simulation results, e.g. Figure 47, one can see how turbulence disrupts the jet surface right downstream from the nozzle orifice. Amplified by the aerodynamic forces, disturbances grow and ligaments detach from the jet surface.

This phenomenon corresponds to the description of the second wind induced breakup regime, and not to the atomization regime. This implies that the borders between the different breakup regimes as defined by Reitz (1978) are probably not valid for the used inflow conditions. The regime borders were defined as a result of measurements where the nozzle flow conditions are not clearly defined and could also be influenced by, e.g., cavitation effects. The further increase of the liquid core length with increasing injection velocity also corresponds to the second wind induced regime. Further simulations with higher injection velocities would be necessary to clarify this point.

4.3 Conclusions

- It was shown that the computational domain size and boundary conditions have an influence on the simulation results for spray formation. It is therefore suggested that the domain diameter normal to the spray axis should be around 12 times the nozzle orifice diameter. Refining the mesh towards the spray axis proved to be a good possibility to reduce cell count and computational effort.

- In the investigated Reynolds number range from 2623 to 7870, the liquid core length increases linearly with increasing injection velocity. This corresponds to measurement results by Arai, Shimizu, & Hiroyasu (1985).

- The liquid core length decreases with increasing ambient gas density. The effect of gas density on the liquid core length is much stronger in the investigated range of 15 to 25 kg/m³ than in the range of 25 to 34.5 kg/m³. Similar results have been published by Arai, Shimizu, & Hiroyasu (1985) and Hiroyasu, Shimizu, & Arai (1982). The increased gas density enhances the Kelvin-Helmholtz instabilities of the jet.

- Regarding the ambient gas density, and following Hobbie & Eggers (2004), all simulations fall in the atomization regime. The visualization of the results shows that the disintegration of the jet does not start at the nozzle orifice, but that initial disturbances of the jet surface coming from turbulence are amplified by aerodynamic forces until ligaments detach. This and the fact that the liquid core becomes longer with increasing injection velocity implies that all performed

simulations are in the second wind induced breakup regime. A possible explanation is the fact that the borders between the regimes were extracted from measurements where the flow conditions inside the nozzle were uncertain. Furthermore, a hard border between two different regimes is hard to define, as there are many influences on the disintegration of a liquid jet, as discussed by Lefebvre (1989). Further simulations with higher injection velocities would be necessary to extend the stability curve and see if the atomization regime is reached at higher Reynolds numbers.

5   A breakup model for transient Diesel fuel sprays

One task of this thesis was to improve the primary breakup model currently used in the 3D CFD software FIRE from AVL. One unique feature of FIRE is the possibility to use a separate injector flow simulation to gain detailed information about the nozzle flow. The flow properties at the nozzle orifice are stored to a so-called nozzle file. This nozzle file can then be used to initialize a subsequent Lagrangian spray simulation. A schematic description of this process is given in Figure 48.
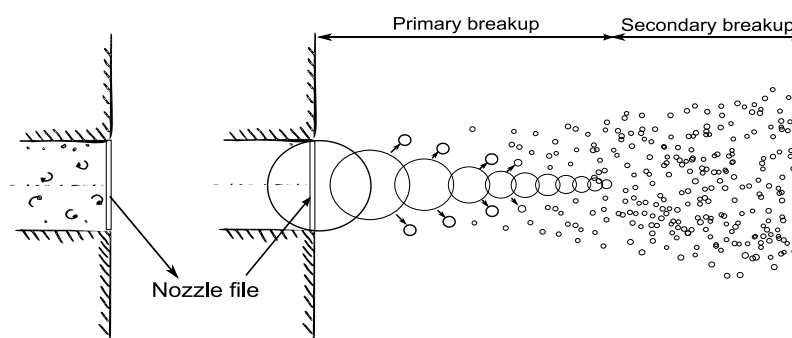
Figure 48: Schematic description of the nozzle file based Lagrangian spray simulation in AVL FIRE

The injector flow simulation is normally performed as a three-phase simulation (liquid, vapor and air). At certain time steps during the simulation, flow properties (velocity, volume fraction, turbulent kinetic energy, dissipation rate, density, temperature) are stored to the nozzle file for each face of the spatially discretized nozzle orifice. Figure 49 shows the flow field at a certain time stored in a nozzle file.

The standard primary breakup model in FIRE v2013.1 FIRE for nozzle file based Lagrangian spray simulations takes advantage of the additional information, like the turbulent kinetic energy, provided through the nozzle file. It is briefly described in chapter 5.1. This breakup model is validated for high Reynolds and Weber numbers when the injector needle is fully open. Modern Diesel engines, however, work with multiple pilot and post injections, where these high injection velocities are not reached. The question is, if the assumptions made for the phase when the injector needle is fully open are valid in the transient phases of injection also. Chapter 5.2 deals with this question and discusses possible problems and

solutions that may arise from the need to simulate a whole engine cycle including multiple injections.
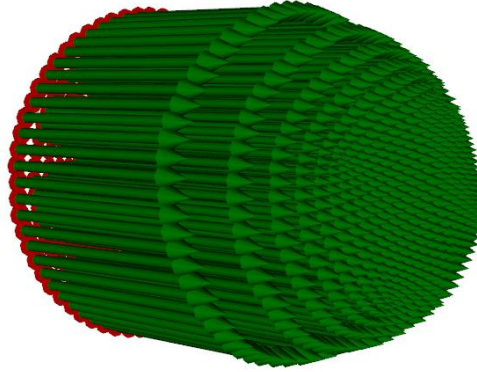
Figure 49: Flow field at the nozzle orifice stored in a nozzle file. The green arrows are symbols for local mean velocities.

5.1   The primary breakup model

The primary breakup model by Tatschl, v.Künsberg-Sarre, Alajbegovic, & Winklhofer (2000) is based upon the competing effects of turbulence, cavitation and aerodynamic breakup processes. The WAVE model is used to determine the aerodynamic breakup rate

$$\left(\frac{dr}{dt}\right)_a = -\frac{r - r_a}{C_2 \tau_a} \quad with \quad r_a = C_1 \Lambda \tag{5.1}$$

where r_a is a characteristic droplet radius depending on the dominant aerodynamic wave length Λ, and τ_a is a characteristic break-up time. The model parameters C_1 and C_2 can be used to adjust the characteristic droplet radius and the break-up time, respectively.

The turbulent break-up rate is calculated from turbulent length and time scales, r_t and τ_t, respectively. This approach is based on the work of Huh & Gosman (1991).

$$r_t = C_\mu^{0.75} \frac{k^{1.5}}{\varepsilon} \qquad \tau_t = C_\mu \frac{k}{\varepsilon} \tag{5.2}$$

$$\left(\frac{dr}{dt}\right)_t = -\frac{r - C_3 r_t}{C_4 \widetilde{\tau}_t} \quad with \quad \widetilde{\tau}_t = \frac{k}{\varepsilon} \tag{5.3}$$

where the constant $C_\mu = 0.09$ and C_4 contains C_μ according to the definition of $\widetilde{\tau}_t$. As for the aerodynamic breakup rate the model constants C_3 and C_4 allow the adjustment of the characteristic droplet radius and the break-up time. Similar to the WAVE model, child droplets are created when breakup occurs. The new droplets get an additional radial velocity v_{ra} or v_{rt} according to aerodynamic or turbulent breakup mechanism, respectively.

$$v_{ra} = C_5 \Lambda \Omega \tag{5.4}$$

$$v_{rt} = C_6 \sqrt{\frac{2}{3} k} \tag{5.5}$$

Therefore the spray angle is determined automatically by the model. Additional equations for the turbulent kinetic energy and its dissipation rate have to be solved to account for the turbulence induced break-up. The impact of collapsing cavitation bubbles on the primary break-up is modeled via an additional source term in the turbulence model. The details of this model are described in Tatschl, v.Künsberg-Sarre, Alajbegovic, & Winklhofer (2000). The turbulence and cavitation induced break-up competes with the aerodynamic one until, at a certain distance downstream from the nozzle exit, the aerodynamic break-up processes become dominant. The transition to the secondary break-up model occurs when one of the following criteria is met:

- The current diameter becomes smaller than the stable turbulent diameter
- The current diameter becomes smaller than 10% of the initial diameter
- The Weber number is lower than 40 and the turbulent breakup rate is smaller than the aerodynamic breakup rate

The blob injection model, described in chapter 2.7.4, is used to initialize the spray simulation. In the current implementation of the primary breakup model, a constant number of blobs is released at every time step of the simulation. The release position of each of those blobs is chosen randomly across the nozzle orifice. The flow properties, stored in the nozzle file for the nearest face to the release position are used to initialize the blob. The initial diameters of all blobs are set equal to the nozzle diameter.

5.2 Improvement of the primary breakup model

Many test simulations with different nozzle flow situations available at AVL have been performed during this thesis. While reviewing the results of these simulations, several problems with the current implementation became obvious and shall be described now.

In the transient phase of the injection, while the injector needle moves, the flow inside the nozzle is not fully developed. This means that the nozzle hole often is not completely filled with liquid, but also contains a reasonable amount of vapor. At start or end of injection, even air may stream back into the nozzle hole. When the injector is fully open, cavitation bubbles may reach the nozzle orifice and reduce the effective nozzle diameter. Figure 50 shows a typical flow field at the nozzle orifice during the beginning of a pilot injection. The red dot in the mass flow diagram marks the time of flow field visualization. The green vectors represent the velocity of the liquid phase while the red faces represent the spatially discretized nozzle orifice. At this time, most of the nozzle orifice is not filled with liquid, but with vapor and air.
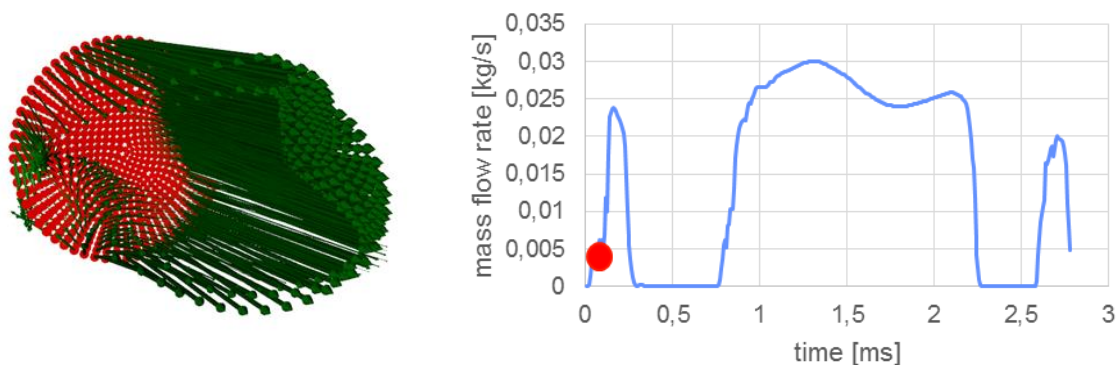
Figure 50: Flow field at the nozzle orifice during a pilot injection (left). Mass flow rate through the injector as a function of time (right).

In the current implementation, blobs are initialized at a random position of the nozzle orifice. It is obvious that this method can only work as intended when the nozzle orifice is fully covered with liquid, as shown in Figure 49. Otherwise blobs may be initialized with the velocity of the vapor or gas phase.

The current model sets the initial blob diameter to the nozzle diameter. This assumption is again only valid if the nozzle hole is totally filled with liquid. If a reasonable amount of the nozzle cross-section is filled with vapor and air, the blob diameter should be reduced.

Since the model was mostly used for the simulation of one main injection at a time, a fixed number of blobs are initialized every time step. Since the application of the model shall be extended to multiple injections, this does not make sense in times when there is no mass flow. The creation of massless blobs in the phase between two injections should be avoided.

Especially at the end of injection it was regarded by reviewing the results of the test simulations that blobs are initialized which neither break up nor evaporate. This unphysical behavior is assumed to have two reasons. When the end of injection is reached, the initial velocity of these blobs is rather low, and the WAVE model is probably not the best model to describe the breakup for lower Weber numbers. The initial blob diameter is set to the nozzle diameter even though in this phase of injection the nozzle hole is not fully filled with liquid. This unphysical large diameter prevents fast evaporation of these blobs.

The following improvements to the primary breakup model are suggested after the evaluation of the current problems:

- Do not initialize any blobs if the current mass flow rate is below a certain threshold value.
- Only release blobs from a face where the liquid volume fraction is higher than a given value.
- Calculate an initial diameter for each blob based on the fraction of the nozzle orifice filled with liquid at the time of initialization.
- Switch between the breakup models, TAB or WAVE, based on the Weber number of each blob. For lower Weber numbers than a given threshold value, the blobs are handled by the TAB model, otherwise by the WAVE model. Figure 51 illustrates the dependence of different droplet breakup modes on the Weber number. One has to be aware that these results were generated using shock waves and that this might not fully correspond to the flow situation during a fuel injection. Otherwise

it is common to use this classification also for non shock wave induced breakup. The obtained results seem to justify this procedure. The TAB model should therefore be better suited to model the breakup at lower Weber numbers and is often used for the simulation of gasoline injection.

- To account for the transient nature of injection, Sazhin, Martynov, Kristyadi, Crua, & Heikal (2008) proposed a modified WAVE model. They suggested to model the liquid core as a rigid body. This means that blobs constituting the liquid core do not experience any drag and move as a rigid jet at a velocity equal to the current injection velocity. This method was introduced, because they observed an under-predicted penetration at the early stages of injection. The model is implemented in FIRE v2013.1 in the following way: All blobs subject to primary breakup experience no drag as long as they are part of the liquid core. If the injection velocity at the nozzle increases due to injection acceleration, this velocity is immediately translated to all blobs constituting the liquid core. The liquid core is defined by its length which has to be provided as a parameter. The simulation results from chapter 4.2.3 can be used to estimate the value of this parameter.

All of these suggested improvements have been implemented in AVL FIRE v2013.1 and are validated in chapter 5.3.
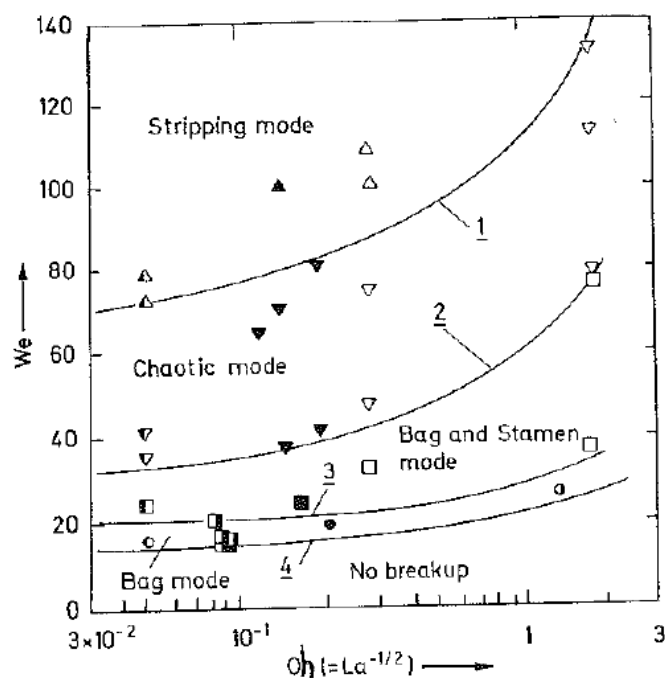
Figure 51: Domains of the droplet breakup mode from Hirahara & Kawahashi (1992)

5.3   Application and validation

The improvements to the primary breakup model described in chapter 5.2 have been implemented in the 3D CFD software FIRE v2013.1 from AVL. The simulations used to analyze the current problems of the primary breakup model were performed again after the changes to the source code.

The effects of the modifications can be seen in Figure 52 and Figure 53, where the Lagrangian spray simulation result, at the time marked in Figure 50 is presented. The nozzle diameter was 250µm in this case. Looking at the color coded droplet diameter in Figure 53 it can be seen that the blobs are initialized with a diameter of about 167µm. This is the effective diameter calculated from the nozzle orifice area that is really filled with liquid. The spray shape also looks as expected, which indicates that all blobs are released at faces where the liquid volume fraction was higher than the defined threshold value of 0.9.
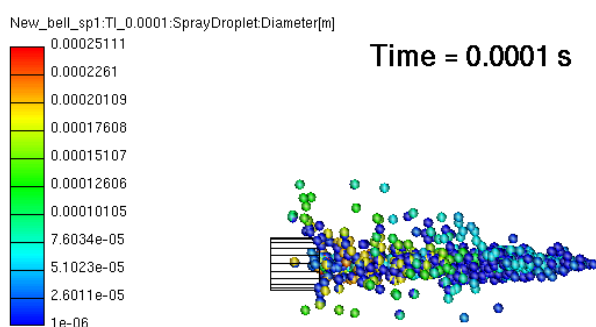
Figure 52: Lagrangian spray result during pilot injection with color coded droplet diameter using the original breakup model.
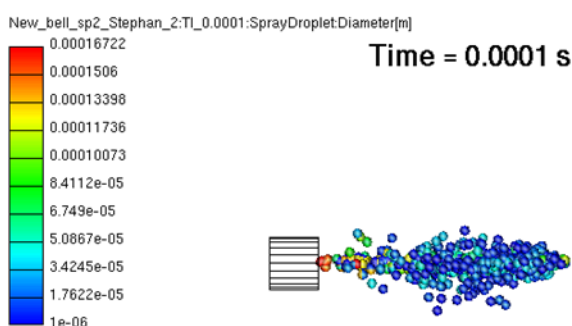
Figure 53: Lagrangian spray result during pilot injection with color coded droplet diameter using the modified breakup model.

The result after the end of the pilot injection is presented in Figure 54. As there is currently no mass flow through the injector, no new blobs are initialized. For all visible parcels, the TAB model is used, since their Weber number during initialization was lower than the threshold value of 50. Compared to the original case, the reduced initial diameter of the blobs and the use of the TAB model led to faster evaporation of the spray. Further tests should be performed to evaluate if these modifications can improve combustion simulation, which strongly depends on the accurate simulation of evaporation.
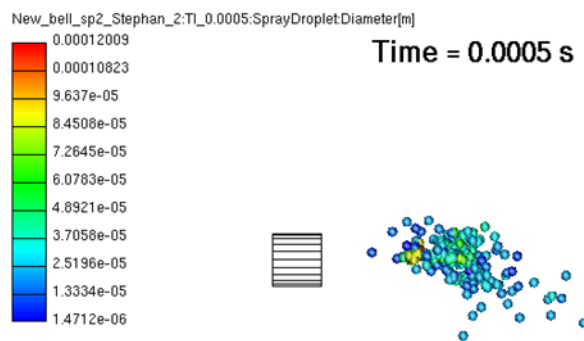
Figure 54: Lagrangian spray result right after end of injection with color coded droplet diameter.

To prove that the modified primary breakup model is able to generate valid results, they are compared to measurements available at AVL. These measurements were performed at the Toyota Central Research and Development Laboratories during a cooperation between AVL List and Toyota and have also been used by Nagaoka, Ueda, Masuda, von Berg, & Tatschl (2008). The experiments were done on an optically accessible high pressure cold constant volume vessel. Images of the spray were captured with a single shot laser pulse light source and a high resolution CCD camera. The measured spray tip penetration was averaged for all nozzle holes. Several mini sac (MS) nozzles were investigated at Toyota and some of them are chosen for the validation of the modified breakup model. All nozzles were tested at room temperature and high pressure ambient gas, as listed in Table 9. The geometrical properties and injection conditions of the nozzles are outlined in Table 8. The number of nozzle holes n was modified according to the nozzle diameter D in order to keep the same range of total mass flow rate. The roundness R at the nozzle hole inlet was chosen to get good agreement between the measured and simulated discharge coefficient C_d. For all nozzles an angle of 105° between the injector

axis and the nozzle hole axis was used. The needle lift curve was approximated from the lift sensor output and is shown in Figure 55. The used timings are listed in Table 8. The simulated and measured injection rates for the nozzle N1 are compared in Figure 56.

Nozzle	n	D [mm]	L [mm]	R/D	C_d	T1 [ms]	T2 [ms]	T3 [ms]
N1	5	0.14	0.8	0.1	0.81	1.0	1.24	2.0
N2	5	0.14	0.6	0.1	0.82	1.04	1.32	2.0
N3	5	0.14	1.0	0.1	0.80	1.04	1.32	2.04
N4	9	0.10	0.8	0.2	0.80	1.0	1.24	2.0

Table 8: Nozzle specifications and conditions

Injected liquid	Diesel fuel
Dynamic viscosity of injected liquid	0.00338 Pa s
Surface tension of injected liquid	0.027 N/m
Density of injected liquid	810 kg/m³
Injection pressure	87.5 MPa
Ambient gas	CO_2
Ambient gas pressure	2.1 MPa
Ambient gas temperature	293 K

Table 9: Operation conditions
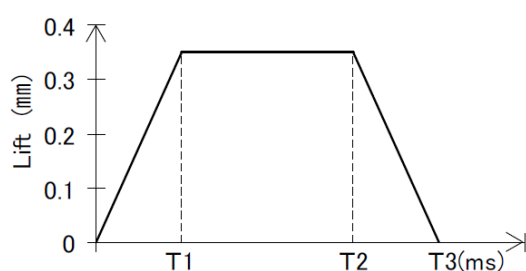
Figure 55: Approximated needle lift curve used for calculations
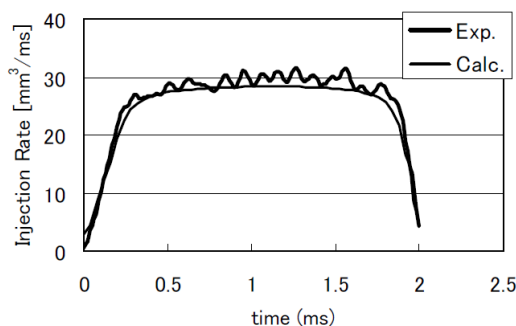
Figure 56: Comparison of injection volume flow rate for nozzle N1

The injector flow simulations were performed at Toyota, and the resulting nozzle files containing the flow properties at the nozzle orifice are used together with penetration measurements to validate the modified primary breakup model.

The computational domain for the Euler-Lagrangian spray simulation is shown in Figure 57. The maximum spray tip penetration that was experimentally measured was about 65mm and the spray diameter at this time was about 18mm. The diameter of the cylindrical computational domain was 5cm (2.8 times the maximum measured spray diameter) and the length was 10cm (1.5 times the maximum measured spray tip penetration). The hexahedral mesh cells had an edge length of 1mm, resulting in a total number of $2.1 \cdot 10^5$ cells. A wall boundary condition was used at the top surface of the domain that contained the nozzle orifice, and static pressure was applied to all other boundaries. The operating conditions are outlined in Table 9. The modified primary breakup model was used together with the WAVE model as the secondary breakup model. The model parameters were the same for all performed simulations. Spray shape and spray tip penetration results are compared to the measurements from Figure 58 to Figure 62. All results are in good agreement with the measurements.
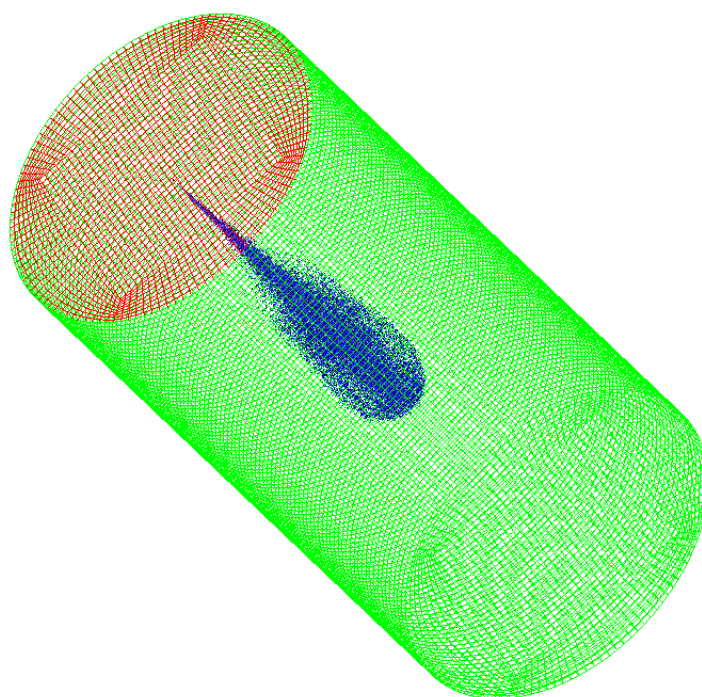
Figure 57: Computational domain with spray
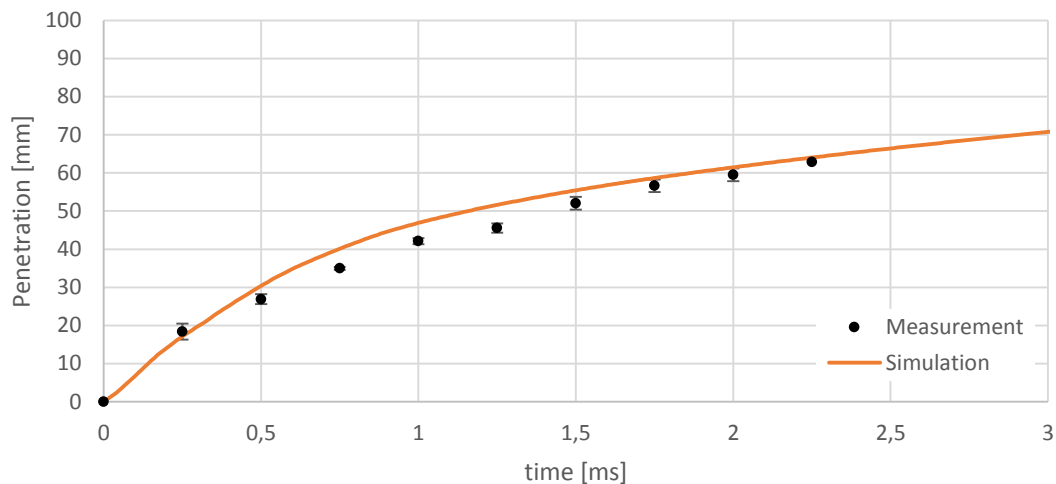
Figure 58: Comparison of spray tip penetration for nozzle N1
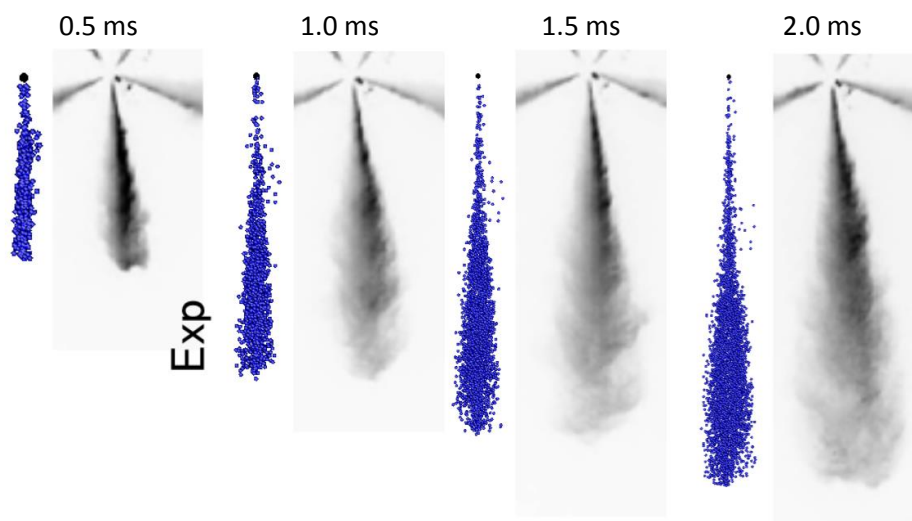
Figure 59: Comparison of spray shape at certain time instants after start of injection for nozzle N1. The spray shape images from the experiments are taken from Nagaoka, Ueda, Masuda, von Berg, & Tatschl (2008).
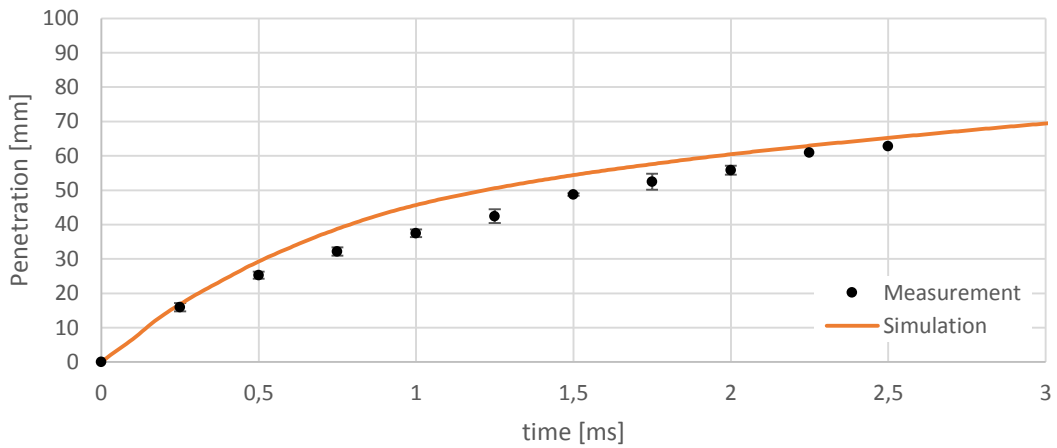
Figure 60: Comparison of spray tip penetration for nozzle N2
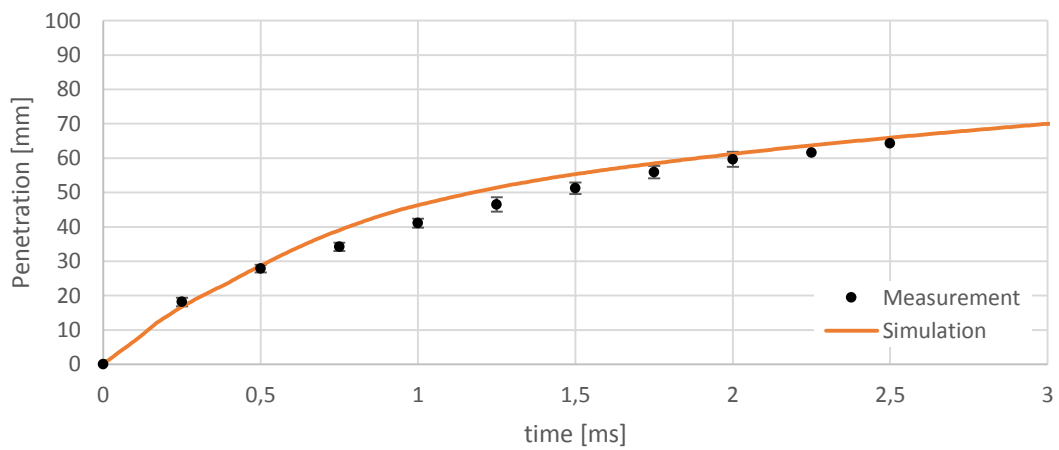
Figure 61: Comparison of spray tip penetration for nozzle N3
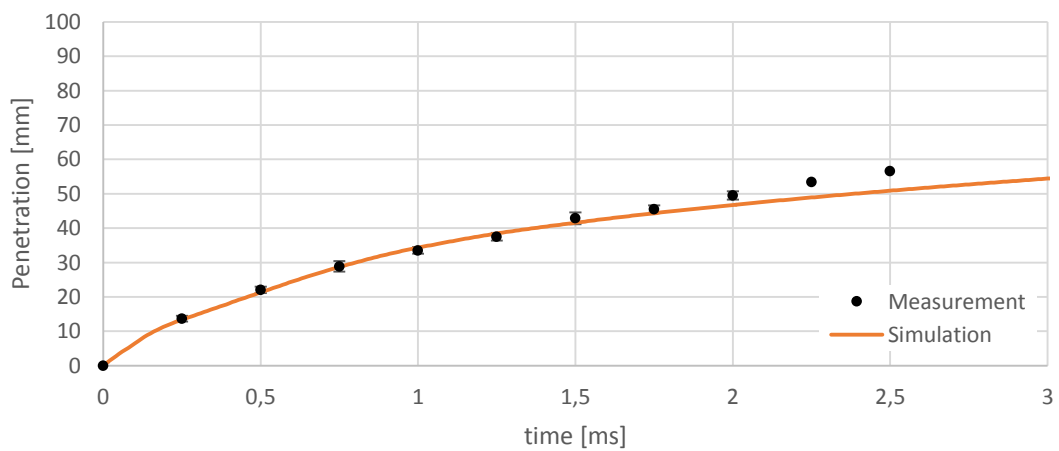
Figure 62: Comparison of spray tip penetration for nozzle N4

5.4 Conclusions

- The modified primary breakup model was applied to several fuel injection test cases. The review of the results showed that the modifications improved the spray shape in the transient phase of injection, e.g. Figure 52 and Figure 53. The automatic calculation of the initial blob diameter, based on the area of the orifice filled with liquid, results in a more physical representation of the actual flow field, e.g. Figure 53.

- The validation results proved that the modified primary breakup model is able to reproduce the measured penetration curve and the spray shape, as shown in Figure 58 to Figure 62. The new parameter for the liquid core length can be used to adjust the form of the penetration curve in the early stages of injection. This should especially help in cases where the penetration in the early stages of injection is underestimated, as mentioned by Sazhin, Martynov, Kristyadi, Crua, & Heikal (2008).

- Mesh dependency is one major problem of CFD spray simulation. Especially the penetration results are sensitive to the mesh size, as described by Baumgarten (2006). The resolution of the mesh that would be needed to properly resolve the gas phase flow quantities violates the requirement of a void fraction close to one of the Lagrangian liquid phase description. Therefore the gas flow can never be resolved accurately near the nozzle, and the parameters of the breakup models have to be adjusted when a different mesh size is used to get similar results. The model parameters are often adjusted so that the simulated cylinder pressure for one engine cycle matches the measured one. If additional information like penetration or droplet size distribution measurements are available, they are used to adjust the models. It is obvious that advanced breakup models are needed that are more based on physics. The amount of parameters that have to be adjusted can then be reduced. Using the flow properties at the nozzle orifice, from a separate nozzle flow simulation, to initialize the Lagrangian spray simulation is a first step in this direction. Large Eddy Simulations of a liquid jet, as described in

chapter 4, could help to better understand the mechanisms of primary breakup and further improve the models.

6 Conclusions and Outlook

The aim of this thesis was to validate and improve the primary breakup model used for the Lagrangian spray calculation in AVL FIRE. The primary breakup model uses the flow properties at the nozzle orifice of a separate 3D multiphase injector flow simulation as an initial condition. At the start of this thesis this method was mostly used for the simulation of one main injection at a time. The suggested model improvements make it possible to get reasonable results also for multiple injections. Of special interest was the transient phase of injection, because the current models are mainly validated for the phase when the injector needle is fully open. To further improve the primary breakup models, detailed information about the region near the nozzle orifice was necessary. This region is visually hard to capture due to the dense spray. Therefore it was investigated if Large Eddy Simulations of the disintegration of a liquid jet can produce reasonable results that can be used to further improve the breakup models. Since LES needs a transient inflow boundary condition, a fully developed turbulent pipe flow was simulated to generate the necessary data. These simulations were used to validate the Coherent Structure Model from Kobayashi (2005) on different mesh sizes against DNS data.

6.1 Conclusions

During the work on this thesis, several conclusions could be drawn. These are summarized now for each topic.

- The results of a Large Eddy Simulation of a fully developed turbulent pipe flow, using the Coherent Structure Model as an SGS turbulence model, showed very good agreement with DNS data. This turbulence model determines the eddy viscosity locally and automatically dampens it near a wall, based on flow properties only. It should therefore also be applicable to complex geometries. The results further showed that a fine mesh is needed in an LES to generate valid results. Only the small turbulent structures can be assumed isotropic, and if the mesh is too coarse, the SGS turbulence models cannot account for the fact that turbulence is highly anisotropic.

- The results of several LES/VOF simulations of a turbulent liquid jet were used to determine the liquid core length under different inflow and ambient conditions. The resulting stability curve shows that the liquid core length increases with the jet velocity, and that it decreases with increasing ambient gas density in the investigated range. It was shown that the simulation of the disintegration of a liquid jet is possible, but comes at extremely high computational costs. If the drop sizes near the nozzle orifice are also of interest, the mesh size must be further reduced to be smaller than the smallest drops. Due to limited memory and computer power, this was currently not feasible.

- The modifications to the primary breakup model for the Lagrangian spray improved the simulation results in the transient phase of injection when the injector needle moves. The validation with measurements showed good agreement for the penetration curve and the spray shape. Mesh dependency and the need to adjust the breakup model parameters are the drawbacks of the Lagrangian spray simulation in general.

6.2 Outlook

The LES/VOF simulations of the breakup of a liquid jet should be extended to higher injection velocities. This would allow to further extend the stability curve of a turbulent liquid jet, as shown in Figure 43, and to understand if and when the transition between the second wind induced and the atomization regimes happens. The next step would be to use highly resolved nozzle flow simulations as an inflow boundary condition of the LES/VOF simulations. This could help to further improve the primary breakup models, since the same inflow boundary condition could be used for the Lagrangian spray simulation. A further refinement of the computational mesh and improvements to the interface tracking algorithm would be necessary to also gain information about the droplet size distribution near the nozzle orifice. This is currently not possible due to the high memory and CPU power requirements, but in the near future numerical experiments could help to better understand the mechanisms of primary breakup.

7   Acknowledgements

8 References

Arai, M., Shimizu, M., & Hiroyasu, H. (1985). Breakup Length and Spray Angle of High Speed Jet. *Proceedings of the 3rd International Conference on Liquid Atomization and Spray Systems*, pp. 1B/4/1-10.

Balewski, B. S. (2009). *Experimental investigation of the influence of nozzle-flow properties on the primary spray breakup. Ph.D. Thesis.* TU Darmstadt.

Baumgarten, C. (2006). *Mixture Formation in Internal Combustion Engines.* Heidelberg: Springer Verlag.

Brackbill, J. U., Kothe, D. B., & Zemach, C. (1992). A continuum method for modeling surface tension. *Journal of Computational Physics, 100*(2), pp. 335-354.

Brenn, G., & Meile, W. (2008). *Strömungslehre und Wärmeübertragung I.* Graz: Institut für Strömungslehre und Wärmeübertragung.

Dumouchel, C. (2008). On the experimental investigation on primary atomization of liquid streams. *Experiments in Fluids, 45*(3), pp. 371-422.

Durst, F., Kikura, H., Lekakis, I., Javanovic, J., & Ye, Q. (1996). Wall shear stress determination from near-wall mean velocity data in turbulent pipe and channel flows. *Experiments in Fluids, 20*(6), pp. 417-428.

Eggels, J. G. (1994). *Direct and Large Eddy Simulation of Turbulent Flow in a Cylindrical Pipe Geometry, Ph.D. Thesis.* Delft University Press.

Ferziger, J., & Perić, M. (2008). *Numerische Strömungsmechanik.* Berlin Heidelberg: Springer-Verlag.

Fukagata, K., & Kasagi, N. (2002). *DNS Database of Turbulence and Heat Transfer.* Retrieved from http://thtlab.jp/DNS/PI12__PG.WL3

Gersten, K. (2004). Fully Developed Turbulent Pipe Flow. In *Mechanics of Flow Metering* (pp. 1-22). Berlin: Springer-Verlag.

Gersten, K., & Herwig, H. (1992). *Strömungsmechanik.* Braunschweig: Vieweg.

Han, J., & Alajbegovic, A. (2002). A Simulation of multiphase flows in complex geometry using a hybrid method combining the multi-fluid and the volume of fluid (VOF) approaches. *Proceedings of ASME FEDSM'02-31153*, pp. 887-892.

Heidorn, D., & Steiner, H. (2009). Subgrid-scale interface model for atomizing high-speed liquid jets. *Turbulence, Heat and Mass Transfer 6.* Begell House Inc.

Herrmann, M. (2011). On Simulating Primary Atomization using the Refined Level Set Grid Method. *Atomization and Sprays, 21*(4), pp. 283-301.

Hirahara, H., & Kawahashi, M. (1992). Experimental investigation of viscous effects upon a breakup of droplets in high-speed air flow. *Experiments in Fluids, 13*(6), pp. 423-428.

Hiroyasu, H., Shimizu, M., & Arai, M. (1982). The breakup of high speed jet in a high pressure gaseous atmosphere. *Proceedings of the 4th International Conference on Liquid Atomization and Spray Systems-ICLASS*(Vol. 82), pp. 69-74.

Hobbie, M., & Eggers, R. (2004). Jet disintegration and drop formation in pressurized gases. In *Final Presentation of the DFG Research Program: Atomization and Spray Processes.* Shaker.

Huh, K. Y., & Gosman, A. D. (1991). Phenomenological model of diesel spary atomization. *Atomization and Spray Technology, Vol. 3*, pp. 309-337.

Jones, W., & Launder, B. (1972). The Prediction of Laminarization with a Two-Equation Model of Turbulence. *International journal of Heat and Mass Transfer, Vol. 15*, pp. 301-314.

Kobayashi, H. (2005). The subgrid-scale models based on coherent structures for rotating homogeneous turbulence and turbulent channel flow. *Physics of Fluids, Vol. 17*.

Kobayashi, H., & Wu, X. (2006). Application of a local subgrid model based on coherent structures to complex geometries. *Center for turbulent research Stanford University and NASA. Annual research brief*, pp. 69-77.

Lefebvre, A. H. (1989). *Atomization and sprays.* New York: Hemisphere Publishing Corporation.

Lumley, J. L. (1978). Computational modeling of turbulent flows. *Adv. Appl. Mech.*(18), pp. 123-176.

McCarthy, M. J., & Molloy, N. A. (1974). Review of Stability of Liquid Jets and the Influence of Nozzle Design. *The Chemical Engineering Journal, 7*, pp. 1-20.

Ménard, T., Tanguy, S., & Berlemont, A. (2007). Coupling level set/VOF/ghost fluid methods: Validation and application to 3D simulation of the primary break-up of a liquid jet. *Inernational Journal of Multiphase Flow, 33*, pp. 510-524.

Nagaoka, M., Ueda, R., Masuda, R., von Berg, E., & Tatschl, R. (2008). Modeling of Diesel Spray Atomization Linked with Internal Nozzle Flow. *THIESEL 2008 Conference on Thermo- and Fluid-Dynamic Processes in Diesel Engines, Valencia*.

Ohnesorge, W. (1931). Die Bildung von Tropfen an Düsen und die Auflösung flüssiger Strahlen. *Zeitschrift für angewandte Mathematik und Mechanik, 16*(6), pp. 355-358.

O'Rourke, P. J., & Amsden, A. A. (1987). The TAB Method for Numerical Calculation of Spray Droplet Breakup. *SAE paper 872089*.

Patel, V., Rodi, W., & Scheurer, G. (1985). Turbulence models for near-wall and low Reynolds number flows: A review. *AIAA Journal, Vol. 23*, pp. 1308-1319.

Pope, S. B. (2000). *Turbulent Flows.* Cambridge: Cambridge University Press.

Prandtl, L. (1945). Über ein neues Formelsystem für die ausgebildete Turbulenz. *Nachrichten der Akademie der Wissenschaften zu Göttingen, Mathematisch-physikalische Klasse*, pp. 6-19.

Prosperetti, A., & Tryggvason, G. (2009). *Computational Methods for Multiphase Flow.* Cambridge: Cambridge University Press.

Ramshaw, J. D., & Trapp, J. A. (1976). A numerical technique for low-spedd homogeneous two-phase flow with sharp interfaces. *Journal of Computational Physics, 21*(4), pp. 438-453.

Reitz, R. D. (1978). *Atomization and other Breakup Regimes of a Liquid Jet. Ph.D. Thesis.* Princeton University.

Reitz, R. D. (1987). Modeling Atomization Processes in High-Pressure Vaporizing Sprays. *Atomization and Spray Technology, 3*, pp. 309-337.

Reitz, R. D., & Bracco, F. V. (1986). Mechanisms of Breakup of Round Liquid Jets. *Encyclopedia of Fluid Mechanics, 3*, pp. 233-249.

Reitz, R. D., & Diwakar, R. (1987). *Structure of High-Pressure Fuel Sprays.* SAE Technical Paper 870598.

Sazhin, S. S., Martynov, S. B., Kristyadi, T., Crua, C., & Heikal, M. R. (2008). Diesel fuel spray penetration, heating, evaporation and ignition: modelling vs. experimentation. *Int. J. Engineering Systems Modelling and Simulation, Vol. 1*(No. 1), pp. 1-19.

Schlichting, H., & Gersten, K. (2006). *Grenzschicht-Theorie.* Berlin: Springer-Verlag.

Smagorinsky, J. (1963). General circulation experiments with the primitive equations, 1. The basic experiment. *Monthly Wheater Review, Vol. 91*, pp. 99-164.

Steiner, H. (2010). *Höhere Strömungslehre und Wärmeübertragung.* Graz: Institut für Strömungslehre und Wärmeübertragung.

Stokes, G. (1851). On the Effect of the Internal Friction of Fluids on the Motion of Pendulums. *Transactions of the Cambridge Philosophical Society*(Vol. 9), p. 8.

Tatschl, R., v.Künsberg-Sarre, C., Alajbegovic, C., & Winklhofer, E. (2000). Diesel Spray Modeling Including Multidimensional Cavitation Nozzle Flow Effects. *Proc. of ILASS-Europe Conference, Sept. 11-13.* Darmstadt.

Van Driest, E. (1956). On turbulent flow near a wall. *Journal of Aeronautical Sciences*(Vol. 23), pp. 1007-1011.